DISSERTATION

TROPICAL RAINFALL REGIMES AND THEIR EVOLUTION ON HOURLY TO DAILY TIMESCALES

Submitted by

Gregory Scott Elsaesser

Department of Atmospheric Science

In partial fulfillment of the requirements

For the Degree of Doctor of Philosophy

Colorado State University

Fort Collins, Colorado

Fall 2011

Doctoral Committee:

Advisor: Christian D. Kummerow

Eric D. Maloney
Mitchell W. Moncrieff
David A. Randall
Steven C. Reising

ABSTRACT

TROPICAL RAINFALL REGIMES AND THEIR EVOLUTION ON HOURLY TO DAILY TIMESCALES

Data from multiple satellite and in situ sources are used to investigate the dominant raining cloud populations in the tropics, with the purpose of documenting how diverse the raining cloud populations are at any given time over a scale similar in size to the grid-box (~100 – 200 km) of a present-day global climate model (GCM). For all locations in the tropics, three similar rainfall clusters (defined according to their ensemble of clouds) are found. Differences in mean-state rainfall (e.g. East versus West Pacific Ocean) are largely the result of similar rainfall clusters occurring at ocean basin-dependent relative frequencies of occurrence.

Area-average rainfall rates are substantially different for each cluster. While each rainfall cluster is observed in all tropical basins, differing relative frequencies of occurrence imply that rainfall lifecycles (i.e. the time duration for transition from light to deep rainfall) vary as a function of basin. Among the processes influencing this transition, both mesoscale cold pools (inferred from QuikSCAT surface wind field retrievals) and convective inhibition (CIN, derived from radiosonde-observations) emerge as important parameters driving the transition from light rainfall to deep

convection at the spatial scale of 100 – 200 km. Associated with significant increases in rainfall are substantial decreases (40%) in convective available potential energy (CAPE).

The temporal evolution of rainfall clusters is derived for different lifecycle stages of a composite Madden-Julian Oscillation (MJO) event. It is found that the rainfall cluster consisting of shallow (<3 km) and congestus raining clouds exhibits little temporal variation for all stages of the composite event, while non-raining scenes and deeper clouds are modulated as a function of time for all stages. Instead of a "transition" from shallow to deep convection, the results suggest an "addition" of deep convection at the expense of non-raining scenes. Unique to the initiation stage, deep organized convective systems are rare until 1 – 5 days before the development of a convective anomaly that finally begins propagating eastward. The lack of deep convection during the initiation stage relative to other stages is associated with both decreased values of columnar water vapor (TPW) and increased stability in the lower-troposphere. Both are hypothesized to preclude the development of deeper convection, thus allowing for the slow (10-30 day) increase in TPW by evaporation to continue, in contrast to later stages of the MJO when moisture convergence serves as the largest contributor to moistening.

The analyses described above are applied to output from a novel multiscale-modeling framework (MMF) coupled with a slab ocean model. The extent to which the MMF yields results similar to the observational depictions outlined above is discussed in great detail.

ACKNOWLEDGEMENTS

I would like to express gratitude to my advisor, Prof. Chris Kummerow, for his "one size doesn't fit all" approach to advising. Throughout the process, Chris was willing to consistently let me pursue my own interests quite independently, but at the same time, was always happily available for any discussion, feedback or guidance. In my case, it was exactly what I desired. I am thankful for the financial support to perform this research, provided by the Center for Multiscale Modeling of Atmospheric Processes (CMMAP). Collaboration with both Jim Benedict and Mark Branson on the multiscale modeling framework output needed to perform the analysis described within is acknowledged. Additionally, I would like to thank my committee members, Drs. Eric Maloney, Mitch Moncrieff, Dave Randall and Steve Reising for occasional discussions on aspects of this work, and for taking time out of their schedules to serve on my committee. Lastly, I would like to thank my wife, Erin. Erin's continual support and willingness to "pick up the slack", particularly in regard to caring for our two young children during the past six months, were instrumental in allowing me to finish this endeavor with more than two cents of sanity and enthusiasm left.

TABLE OF CONTENTS

LIST OF ACRONYMS

CAPE	Convective Available Potential Energy
CIN	Convective Inhibition
CMORPH	Climate Prediction Center Morphing Technique (for rainfall observations)
CPKE	Cold Pool Kinetic Energy
CRM	Cloud-Resolving Model
GCM	Global Climate Model or equivalently, General Circulation Model
MERRA	Modern-Era Retrospective Analysis for Research and Applications
MCONV	Moisture Convergence
MCS	Mesoscale Convective System
MJO	Madden – Julian Oscillation
MMF	Multiscale Modeling Framework
ORG	Organized Deep Convection Cluster
PTH	Precipitation Top Height
RAOB	Radiosonde Observation
RFO	Relative Frequency Of Occurrence
RMS	Root-Mean Square

SHAL	Shallow Convection Cluster
SST	Sea Surface Temperature
TKE	Turbulent Kinetic Energy
TPW	Total Precipitable Water
TPWTRANS	Vertically-Integrated Moisture Convergence
TRMM	Tropical Rainfall Measuring Mission
TRMM PR	TRMM Precipitation Radar
UNORG	Unorganized Deep Convection Cluster

CHAPTER 1

INTRODUCTION

1.1 Motivation

Global average precipitation is constrained by the energy budget of the troposphere. On a regional scale, however, variations and trends in precipitation are tied directly to tendencies in the local atmospheric circulations and water vapor concentration. Therefore, while global mean precipitation may be tending in one direction given perturbations to the components of the energy budget (due to both anthropogenic and natural causes), regional precipitation may be systematically decreasing or increasing in time (Allen and Ingram, 2002; Sun et al. 2007). Thus, as Earth's climate warms, given the obvious connection between water and human society, any trend in regional water (largely provided by rainfall) over time has indisputable effects on society. To this end, it becomes increasingly important to understand the potentially changing, regionally dependent rainfall states.

This is recognized in both the observational and modeling community of the atmospheric sciences field. From the observational perspective, the need for increased understanding has motivated the formulation of the upcoming Global Precipitation Measurement (GPM) Mission (Hou et al. 2008). Recognizing that regional rainfall is a composite of rapidly evolving precipitation systems, the ultimate goal of GPM is to

measure rainfall over all regional domains at a three-hour resolution. With this comes the need to synthesize additional environmental observations in a manner that increases understanding of what ultimately influences rainfall on these soon-to-be globally observed hourly timescales.

From the modeling perspective, in order to accurately simulate regional changes in rainfall, the model must first have the ability to simulate the diverse number of raining clouds observed over any region, and properly represent their impact on the larger-scale thermodynamics and general circulation. Deficiencies in the representation of rainfall and clouds in current global climate models (GCMs) have motivated the development of a new state-of-the-art modeling framework that involves embedding a cloud-resolving model (CRM) into each large scale grid-box of a GCM (a configuration often referred to as a multi-scale modeling framework, or MMF; Grabowski and Smolarkiewicz (1999) and Grabowski (2001)). In designing an MMF, a stated intention is to better represent the complex interactions between clouds and the environment, and to improve the characteristics of rainfall as a function of the large-scale atmosphere (using currently-available observational products as a metric). In the period of time leading up to the widespread use of global CRMs in climate simulations, the MMF is arguably one of the more promising modeling approaches for conducting longer-term weather and climate simulations (Randall et al. 2003; Arakawa 2004; Arakawa et al. 2011).

In the meantime, before the launch of GPM and maturation of the MMF approach, designing rainfall studies that incorporate both GPM objectives (i.e. study of rainfall regimes at a higher temporal resolution) and MMF goals (i.e. investigating parameters – potentially represented well in a mature MMF – that influence rainfall on short timescales)

would be a worthwhile pursuit. The overarching goal of this dissertation is to perform such a study. Through the use of a combined multi-sensor observational framework and current-generation MMF configuration (two-dimensional CRM embedded in a GCM), tropical rainfall tendencies and ensemble cloud populations evolving on diverse timescales ranging from 3-6 hours to intraseasonal periods are studied. By virtue of presenting MMF results next to observations in a side-by-side depiction, an evaluation of the model representation against current observations is implicit. However, beyond a simple evaluation approach, a goal of this work is to determine to what extent currently available observational platforms and modeling configurations can provide a coherent, consistent picture of rainfall, cloud ensembles and processes influencing rainfall tendencies on short time scales. In essence, then, a collaborative approach involving both is pursued, the specific components of which are discussed below.

1.2 Outline of Dissertation

In addition to this introduction (Chapter 1) and final conclusions chapter (Chapter 6), this dissertation consists of four content chapters (Chapters 2 – 5), written in a manner that allows for each chapter to be read as a stand-alone paper with its own introduction and conclusions; nonetheless, each chapter does build on the preceding one, as evidenced by the consistent references to prior chapters.

Regarding these content chapters, Chapter 2 in present form was published in the *Journal of Climate* in May 2010. In this chapter, substantially different tropical rainfall regimes (West Pacific versus East Pacific, for example) are investigated with the purpose of determining to what extent significantly different mean states are reproduced by favored

ensembles of raining clouds (i.e. "building blocks") recurring at region-dependent relative frequencies of occurrence. A similar question was asked concerning cloud regimes recently (e.g. Jakob and Tselioudis 2003; Zhang et al. 2007), and results in those studies provided motivation to ask the same question concerning tropical rainfall regimes. Data from the Tropical Rainfall Measuring Mission (TRMM) Precipitation Radar (PR) serve as the foundation for defining the state of rainfall. A particular focus of this study is on distributions of raining cloud types and heating, and not simply area-averaged rainfall. In this manner, prevalent rainfall states are characterized according to their constituent raining cloud populations.

The findings of Chapter 2 suggest that to a large extent, different mean rainfall regimes can be reproduced by a limited number of rainfall clusters (one consisting of predominantly shallow raining clouds, and the others comprising progressively deeper clouds) occurring at location-dependent relative frequencies of occurrence. Furthermore, these results also suggest that regions with different temporal-mean rainfall regimes transition through similar shallow and deep precipitation states, but do so at varying rates leading to significantly different rainfall lifecycles. Therefore, the material in Chapter 3 focuses on investigating the mechanisms that influence the transition from shallow rainfall to deeper, more organized rainfall, with the purpose of gaining insight (from a purely observational perspective) on what may cause the transition from one rainfall cluster to another over varying time scales. Recent modeling studies have highlighted the importance of sub-GCM scale fluctuations (i.e. unresolved in current GCMs) in atmospheric fields (e.g. Fletcher and Bretherton 2010) in determining the transition from non-raining clouds to rainfall. Along this same vein, but focusing on the transition from light to deeper rainfall, a

new observational parameter related to cold pool activity (based on wind vector retrievals from the QuikSCAT scatterometer) is developed and its relation to rainfall evolution is investigated in this chapter.

Considered together, Chapters 2 and 3 analyze regional rainfall regimes, their constituent cloud populations and the transition from light to deeper rainfall (on both hourly and daily timescales) from a multi-sensor observational perspective. This is directly related to the GPM aim of documenting regional rainfall evolution on hourly timescales. An equivalent analysis of rainfall regimes and rainfall lifecycles from the perspective of a state-of-the-art climate model (an MMF) is performed in Chapter 4. Select observational results from Chapters 2 and 3 are reproduced in this chapter in a side-by-side comparison to the MMF results. As is the case for the observational analysis, rainfall regimes are largely interpreted according to cloud populations. Drawing on the strengths of both the observational sources used and the MMF utilized, a concerted effort is made to develop a consistent conceptual picture of 1) what the dominant raining cloud populations are in the tropics, and 2) what background parameters aid in distinguishing one population from another, and more generally, what factors influence the transition from a shallower raining state to a deeper one.

In Chapter 5, the rainfall clusters derived in Chapters 2 and 4 are investigated within the context of the Madden – Julian Oscillation (MJO, Madden and Julian 1971, 1972), a phenomenon known to influence regional rainfall on intraseasonal timescales. A particular focus of this chapter is on the evolution of both the observed and modeled rainfall clusters during the initiation period of the MJO in the West Indian Ocean, a currently less understood stage in the lifecycle of the MJO (Kim et al. 2009). While

Chapters 2 – 4 focus on rainfall states and rainfall transition over hourly to daily timescales, the analysis in this chapter – within the MJO context – involves documenting the evolution of rainfall and cloud populations on 30 – 90 day timescales.

The key findings in the content chapters (Chapters 2 – 5) are summarized in Chapter 6, and suggestions for future work are interspersed throughout.

CHAPTER 2

OBSERVED SIMILARITY OF PRECIPITATION REGIMES OVER THE TROPICAL OCEANS

2.1 Introduction

A variety of precipitating clouds, categorized by their vertical extent and rainfall characteristics, have been observed over the tropical oceans (e.g., Warren et al. 1985; Masunaga and Kummerow 2006). Even though the distribution of precipitating clouds is continuous in nature, a number of studies have consistently shown that dominant ones emerge from the spectrum: three convective types consisting of shallow cumuli, congestus cumuli and deep precipitating cumulonimbi (Johnson et al. 1999) and a non-convective stratiform type considered to be, in large, a by-product of deep convective activity in the tropics (Houze 1997). Given a particular basin, the longer-term temporal mean state of precipitating convection can be thought of as comprising the average prevalence of each convective and attendant stratiform precipitating cloud type. Over the past few decades, satellite and in situ studies have sought to document both the mean characteristics of precipitating convection across the tropics, as well as the differences that exist from one basin to another. Consistently, a number of observational studies have shown that the statistical average heating rate, rainfall rate, cloud fraction, cloud type and spatial extent of

rainfall systems is not homogeneous across the tropical oceans (e.g., Houze and Betts 1981; Berg et al. 2002; Masunaga and Kummerow 2006; Zuidema and Mapes 2008).

Despite the documented dissimilarities in the mean precipitation states, there remains uncertainty regarding the extent to which a particular precipitation regime (containing a particular distribution of precipitating clouds) occurring in one geographic basin resembles the same regime type occurring in another basin. Specifically, it remains unclear whether or not the proportions of each cloud type (shallow precipitating cumulus, congestus and deep convective) are approximately constant given the presence of a particular precipitation regime, to what extent precipitation regimes are mixed in terms of cloud types, and how similar particular precipitating cloud types are from one basin and one precipitation regime to another.

There is continued motivation, then, to determine whether or not precipitation regimes can be described from an instantaneous perspective with universal descriptors versus describing precipitation from a longer temporal-mean perspective. This study explores the nature of precipitation regimes through consideration of the ensemble of precipitating clouds (beyond the most prevalent cloud type) belonging to a precipitation regime, with further investigation into how consistent each regime's spectral cloud ensemble is as a function of tropical ocean basin. Precipitation regimes are objectively identified and characterized using a common clustering framework applied separately and independently to adjacent geographic basins spanning the entire tropics, with the intention of diagnosing the extent to which regimes are similar. It is assumed a priori that regimes contain a mixture of precipitating cloud types and therefore, individual precipitating clouds are not isolated so as to avoid compositing similar precipitating clouds from different

regimes. The role of each cloud type within the precipitation regimes, in terms of their contribution to regime diabatic heating, is also investigated using new satellite-based products.

Results are presented that support a stronger idea of precipitation regime self-similarity by considering a regime comprising an ensemble of precipitating clouds as a whole, rather than considering precipitating clouds independently of the precipitation regime in which they are developing. These precipitation regimes in their entirety may better serve as repeatable, recurring "building blocks" of the mean-state of tropical precipitation instead of considering individual precipitating clouds as the "building blocks" themselves.

2.2 Data Sources

The primary data products used are derived from instruments onboard the TRMM satellite. The period of study consists of 48 months from Jan 2004 – Dec 2007. Both TRMM PR attenuation-corrected radar reflectivity (Z_E) profiles (surface to 20 km) and surface rainfall rates at the PR native spatial resolution (approximately 5 km) are used and are provided in the standard TRMM PR 2A25 product (hereafter, the 2A25 product; Iguchi et al. 2000). For each PR pixel classified as convective, the precipitation top height (PTH) corresponding to the observed precipitating cloud is computed. The PTH is the altitude of the highest radar echo above Earth's surface with a reflectivity of at least 17 dBZ (further details in Short and Nakamura 2000). A new dataset is created, with a 1º horizontal resolution centered on nadir PR pixels for all TRMM orbits, where each sample now comprises all PTHs associated with the spectrum of precipitating convective clouds present

in the 1º grid. The decision is made to consider the distribution of PTHs within a 1º grid for three primary reasons: 1) the root-mean-square (RMS) error variances in the ancillary diabatic heating products decrease as the spatial averaging-widths increase; 2) the desire to capture the statistical distribution of cloud PTHs present at some instantaneous time in a larger-scale regime requires the consideration of larger box-widths; 3) the nature of the PR scan geometry leads to an under-sampling of shallow cloud PTHs for pixels significantly off-nadir, and therefore, a coarser-than-1º resolution leads to PTH distributions that are biased with respect to the number of shallow precipitating clouds present. The average rainfall rate for each type of precipitating convective cloud, the average stratiform rainfall rate, diabatic heating and the number of non-convective and non-raining pixels are also stored for each 1º sample.

The apparent heat source (Q_1, Yanai et al. 1973) is the diabatic heating associated with unresolved cloud processes occurring in a rainfall regime. Q_1 can be written as

$$Q_1 = \frac{\partial}{\partial t}\bar{s} + \nabla \cdot (\overline{s\mathbf{V}}) + \frac{\partial}{\partial p}\bar{s}\,\bar{\omega} = \overline{Q_R} + \overline{\mathrm{LH}} - \frac{\partial}{\partial p}\overline{s'\omega'} \qquad (2.1)$$

where the total change in the dry static energy ($s = c_pT + gz$), horizontally averaged over a specified domain size (as indicated by the overbar), is given by the sum of three horizontally averaged diabatic heating components: the radiative heating rate (Q_R), the latent heating rate due to phase changes of water (LH) and the heating due to vertical eddy heat flux ($\overline{s'\omega'}$) convergence (the primes indicate departure from a horizontal mean). A term incorporating the effects of horizontal eddy heat fluxes is assumed to be small, and has not been derived. The Spectral Latent Heating algorithm product (SLH product; Shige

et al. 2004, 2007) is used for quantification of the latter two components of the right hand side of Eq. (2.1). These components combined are mathematically equivalent to $Q_1 - Q_R$ (hereafter, occasionally referred to as $Q_{1\text{-}R}$). Heating profiles are available for each TRMM PR pixel at the PR native resolution. The SLH algorithm takes into account the vertical extent of the convection and is therefore able to differentiate shallower heating structures from deeper heating structures corresponding to various vertically extended precipitating clouds. It is important to note that the SLH algorithm estimates heating due to precipitation processes only, as discussed in Shige et al. (2007). $Q_{1\text{-}R}$ is averaged to the same 1º grids described above, and the heating profile represents the composite effect of the various precipitating clouds present in a rainfall regime. Horizontal averaging also has the effect of reducing the RMS error variance associated with the heating estimates (Shige et al. 2007).

The Hydrologic Cycle and Earth Radiation Budget (HERB) algorithm produces radiative heating profiles (Q_R) at 0.25º horizontal resolution and 1 km vertical resolution (L'Ecuyer and Stephens 2003; L'Ecuyer and Stephens 2007; L'Ecuyer and McGarragh 2009). The algorithm utilizes cloud and precipitation information in conjunction with atmospheric water vapor, temperature profiles and surface variables derived using sensors onboard the TRMM satellite, and incorporates a radiative transfer model that simulates vertical profiles of longwave (LW) and shortwave (SW) radiative fluxes. Heating rates are then derived using radiative flux divergences, and these estimates are averaged to 1º [these represent the first term on the right-hand side of Eq. 1]. The vertical profiles of Q_R are smoothed using a 3 km boxcar-averaging window since the nominal 1 km vertical resolution of the product is likely more coarse due to the sole use of passive remote sensing

techniques for determining cloud boundaries in the algorithm (L'Ecuyer and McGarragh 2010).

2.3 Precipitation Regime Identification and Self-Similarity

Figure 2.1 shows the temporal mean state of precipitation and associated Q_1 for five adjacent geographic regions spanning the tropics for the time period under study. These five regions extend meridionally from 15º S to 15º N over the tropical oceans and are labeled according to the ocean basin they predominantly encompass (see Fig. 2.4; Indian (INDI), west Pacific (WPAC), central Pacific (CPAC), east Pacific (EPAC) and Atlantic (ATLA)). Zonally, INDI extends from 30-100º E, WPAC from 100-170º E, CPAC from 170-220º E, EPAC from 220-290º E, and ATLA from 290-360º E longitude. It is from this background mean precipitation state that prevalent precipitation clusters or "regimes" are extracted.

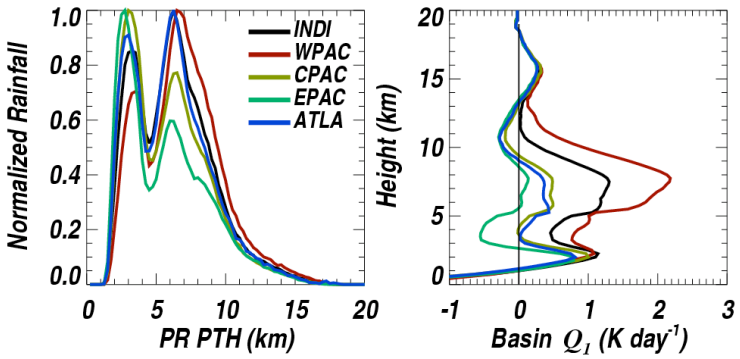

Figure 2.1. The distribution of rainfall as a function of convective cloud PTH for basins spanning the tropical oceans (left panel). Distributions are normalized to account for differences in total rainfall in each basin (see text for further description). The right panel illustrates the average Q_1 profile for each basin.

The left panel of Fig. 2.1 shows the normalized rainfall histograms as a function of cloud PTH. Histograms have been normalized as in Berg et al. (2002, their Fig. 8) such

that the maximum rainfall value is equal to 1 and area under the rainfall curve is the same for each basin. In the average sense, since the total accumulated rainfall is quite different for each basin, normalizing in this manner allows for easier comparison of rainfall histograms and allows one to determine which cloud types play the largest role in rainfall accumulation for each basin. Upon inspection of Fig. 2.1, it becomes clear that rainfall distributions for various tropical basins are not simply scaled by a constant, nor are they unimodal. There is a distinct shift in the types of precipitating clouds that produce most of the rainfall as one traverses geographic basins in the tropics. Because the majority of rain falls from deeper clouds in the Indian and west Pacific basins (left panel of Fig. 2.1), one would expect that Q_1, on average, is larger in magnitude at higher altitudes compared to the other basins, a result seen in the right panel of Fig. 2.1. Like the rainfall histograms, Q_1 profiles are not unimodal either, with peak heating near 2 km and 6-8 km. These results are consistent with the studies summarized in Section 1 noting differences in rainfall and heating across the tropics, as well as the differences in the numbers of various precipitating cloud types across the tropical oceans.

The focus now turns toward determining if dominant precipitation clusters can be extracted from the mean state. Precipitation clusters are identified through use of a simple K-means clustering algorithm (Anderberg 1973). A number of recent studies (Jakob and Tselioudis 2003; Boccippio et al. 2004; Jakob et al. 2005; Rossow et al. 2005; Zhang et al. 2007; Caine et al. 2009) used this same technique to identify cloud and precipitation regimes, and the results show the usefulness of the technique. A cluster is assumed to always contain a spectrum of precipitation clouds. In order to capture the ensemble, the K-means algorithm is applied to five variables in each 1º grid box: the number of clouds with

PTHs less than 5 km, the number of clouds with PTHs from 5-9 km, the number of clouds with PTHs greater than 9 km, the convective rainfall rate averaged over all pixels identified as convective, and the ratio of the average convective rainfall rate to the average rainfall rate (defined as the average over all raining pixels).

The first three variables are normalized by the number of convective precipitation pixels in the grid box. All five variables are standardized, and the K-means algorithm is then applied to all 1º-grid samples for each ocean basin (independently) across the tropics. The algorithm seeks to find the centers of natural clusters present in a dataset. One begins by specifying both the number of clusters and initial data centers (termed centroids, and they are chosen at random). The technique involves assigning each 1º-grid (a data point) membership to a particular cluster based on a minimum Euclidean distance measure. The distance is defined as the sum of the squared differences between each centroid variable and the same variable corresponding to the data point. After evaluating the entire dataset, centroids are re-computed by computing the new mean of each variable for all data points belonging to a particular cluster. The algorithm proceeds in an iterative manner, and when the centroid of the current iteration is the same as that of the previous iteration (decided based on the sum of the squared differences in the centroid variables from one iteration to the next), the specified convergence criterion is met and a solution is found.

2.3.1 Regime Cloud Top Distributions and Rainfall

Three precipitation clusters emerge in each basin; together, they explain approximately 60% of the variation in the five clustering variables across the tropical oceans, a magnitude that is consistent for each geographic basin. The percent of explained variance increases much less rapidly upon the consideration of additional clusters; therefore, the a priori choice of three clusters is considered reasonable. Over 100 iterations of the clustering algorithm were executed for each ocean basin, using a random assignment for first-guess centroids each time. The precipitation clusters were found to be largely invariant to the initial centroid assignment, providing a heuristic measure of the robustness of the results.

Figure 2.2 shows the relative frequency of occurrence (RFO) distributions for clouds of given PTHs for the three clusters. While a cluster is classified according to the predominant, most vertically extended precipitating cloud, each cluster consistently contains a spectrum of precipitating clouds. The shallow (SHAL) precipitation cluster in the top panel of Fig. 2.2 is largely unimodal, and contains precipitating clouds with PTHs peaking in the 2-4 km altitude range, with

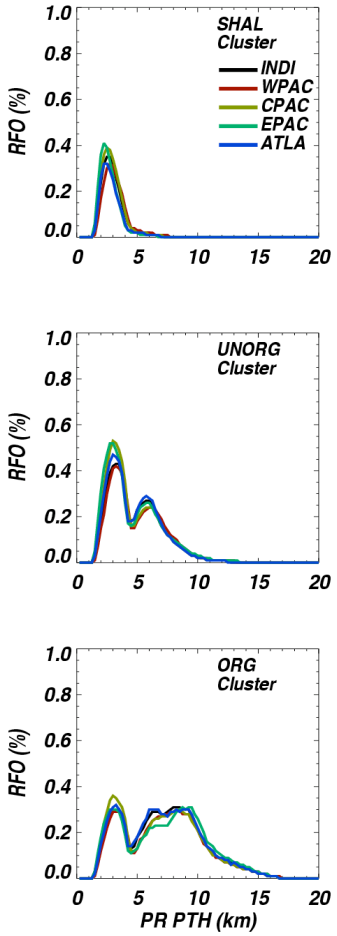

Figure 2.2. The distributions of PTH for the precipitating cloud ensembles that characterize the SHAL, UNORG and ORG precipitation clusters for all tropical ocean basins. The RFO is computed by dividing the number of clouds with a given PTH by the number of pixels within each grid box.

very few clouds having PTHs extending beyond 5 km. The cluster in the middle panel of Fig. 2.2 is consistently bimodal in all basins, with a peak in cloud PTHs near 3 km, and a prevalence of precipitating clouds with PTHs extending from 5.5 to 10 km. This is classified as an unorganized deep convection (UNORG) cluster, and is so chosen based on the presence of deeper convective towers, but with a less significant stratiform component of heating (discussed later) and less rainfall coverage over the 1° grid box. The final precipitation cluster (classified as ORG) consists of a shallow cloud PTH peak near 3 km, a broad second PTH peak extending in height up to 16 km, implying the existence of numerous congestus and progressively deeper precipitating clouds, and a significant component of atmospheric heating dominated by stratiform precipitation (also discussed later), all of which implies that the precipitation regime is representative of organized convection. It should be noted that the distributions of precipitating clouds in Fig. 2.2 are fairly insensitive to the current choice of PTH bin limits used for the first three clustering variables described in the previous section. For each cluster, the convective rain fractions can be determined by summing all RFO values for each convective cloud type (identified based on the cloud's PTH) shown in Fig. 2.2. These fractions are show in Table 2.1.

Table 2.1. Rainfall and heating characteristics of precipitation clusters.

	SHAL	UNORG	ORG
Convective Rain Fraction (%)	2.7	7.1	9.9
Rain Fraction (%)	4.5	17.8	43.8
Ave Surface Rainfall (mm day^{-1})	2.1	14.2	53.9
% of Surface Rainfall classified as Stratiform	30	40	50
$\langle Q_1 - Q_R \rangle$ (K day^{-1})	0.4	3.1	12.7
$\langle Q_R \rangle$ (K day^{-1})	-1.2	-0.8	-0.3

While it has been discussed that the number of precipitating clouds stratified by cloud PTH varies across the tropics, the distributions of precipitating clouds are approximately constant within each cluster, independent of the basin under study (Fig. 2.2). Additionally, the UNORG and ORG clusters are similar in distribution and multimodal for all basins, with one mode consisting of prevalent warm-rain clouds topping out below the mean freezing level in the tropics, in close proximity to deeper precipitating clouds. The average rainfall fractions (defined as the total number of raining pixels divided by the total number of pixels in a grid box) are shown in Table 2.1. The variations of both the convective and total rainfall fractions with respect to the cluster-average magnitudes are on the order of 5%, further implying that the ratio of stratiform to convective rain fraction is approximately the same for each cluster as a function of ocean basin as well.

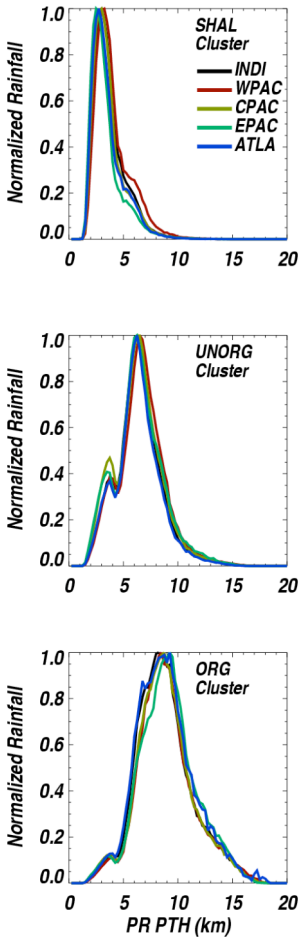

Figure 2.3. As in the left panel of Fig. 2.1, except that the rainfall distributions are now stratified by precipitation cluster observed in each geographic basin.

The distribution of convective rainfall parsed by PTH for each cluster and each geographic basin is shown in Fig. 2.3. The data analysis illustrated here is exactly the same as that illustrated in the left panel of Fig. 2.1, except the focus is shifted to comparing precipitation clusters separately for each geographic basin, and not the geographic basin in

its entirety (irrespective of precipitation cluster present). Whereas the rainfall distributions are quite different in the mean sense (Fig. 2.1), the distributions track each other quite closely within each cluster, and the dominant peaks for convective rainfall production are quite similar for each basin given the presence of a particular cluster. These peaks are around 2-4 km for the SHAL cluster, 6-8 km for the UNORG cluster, and 8-10 km for the ORG cluster. The shallower precipitating clouds (associated with PTHs extending from 3-4 km) that contribute to the bimodality in the PTH distribution in the UNORG and ORG clusters also contribute to the bimodal rainfall histograms as well, although the peaks are less pronounced.

In the time-mean sense, the average surface rainfall rate for 1º grids in each geographic basin varies, on average, by approximately 30% with respect to the tropical average surface rainfall rate (this average includes all 1º grids, so non-raining grids are included as well). If non-raining grids are neglected, the average difference decreases to approximately 16%, so a significant percentage of the average variation arises from notable differences in the number of non-raining scenes that exist in each basin. When stratifying by cluster, however, the rainfall rate differences are typically under 5% for all basins with respect to the cluster mean. The cluster-average surface rainfall rates are provided in Table 2.1.

For all grid boxes covering the tropical oceans, the various cluster contributions to total accumulated rainfall are shown in the top three panels of Fig. 2.4. The SHAL cluster contributes 20 - 25% of the total rainfall in both the INDI and WPAC regions, and as one approaches the dateline and continues eastward, the SHAL cluster progressively contributes more towards the net accumulated rainfall. In the EPAC basin, the SHAL

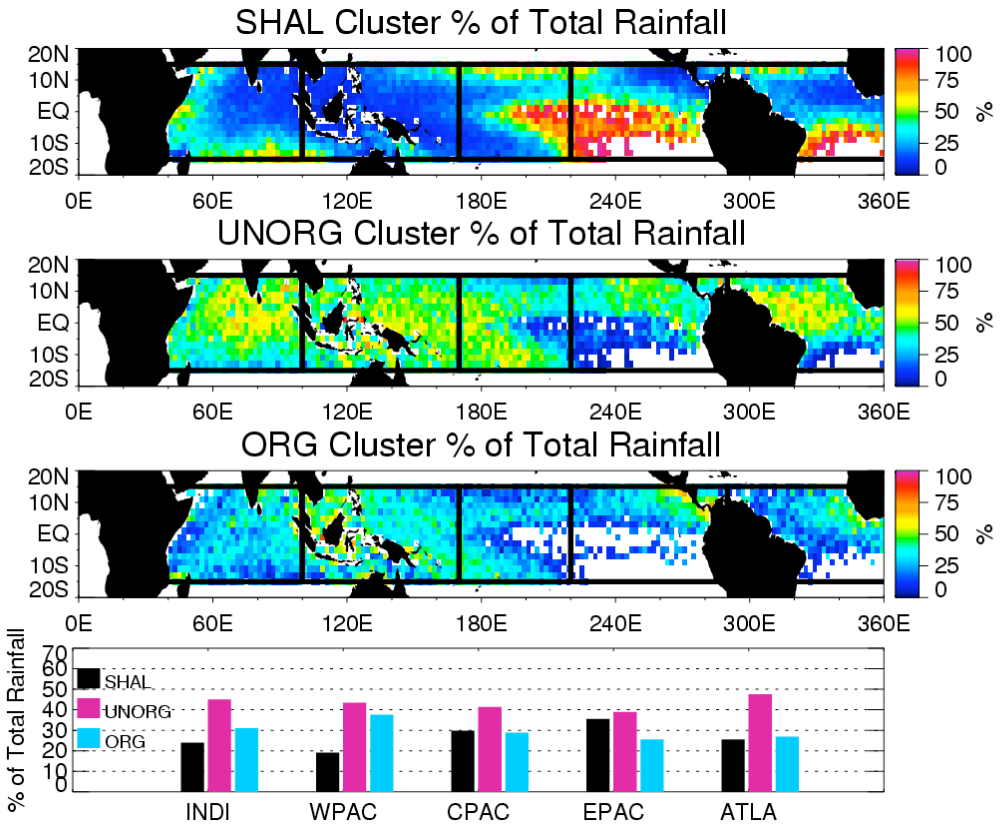

Figure 2.4. The percent contribution to the total accumulated rainfall by each precipitation cluster as a function of ocean location (top three panels). Considering the five large geographic basins in their entirety, the percent contribution to the total rainfall by each cluster is shown in the bottom panel.

cluster contributes almost as much rainfall as the UNORG cluster, and more than the ORG cluster. UNORG and ORG clusters are observed everywhere throughout the tropics, including outside of the inter-tropical convergence zone (ITCZ) regions, and not surprisingly, contribute significantly to the total rainfall in each geographic basin.

2.3.2 Regime Diabatic Heating

The $Q_{1\text{-}R}$ profiles for the three clusters are shown in Fig. 2.5. Qualitatively, the profiles are quite similar for each basin, and as the intensity of convection increases,

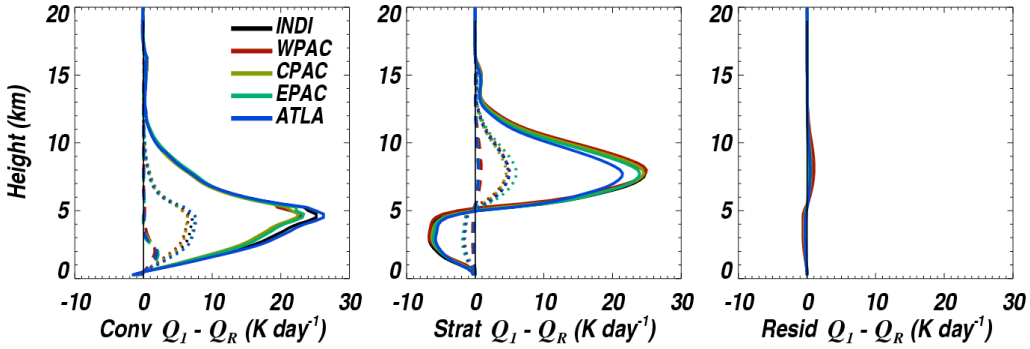

Figure 2.5. The left (center) panel presents the composite convective (stratiform) Q_1 – Q_R profiles for each of the precipitation clusters and each geographic basin. The right panel illustrates the residual Q_1 – Q_R profiles that remain unclassified for each basin. The SHAL (UNORG, ORG) clusters are denoted by the dashed (dotted, solid) lines in the two left panels.

corresponding to a transition from SHAL to UNORG to ORG clusters, the peak and magnitude of $Q_{1\text{-}R}$ increases. The convective (stratiform) $Q_{1\text{-}R}$ is the mean of the convective (stratiform) $Q_{1\text{-}R}$ profiles corresponding to each convective (stratiform) precipitating cloud present in the cluster. As the strength of the convection increases, corresponding to stronger and deeper convective clouds, the anvil production of rainfall increases, and so does the stratiform signature of $Q_{1\text{-}R}$. The stratiform signature is an order of magnitude smaller in the SHAL cluster compared to the ORG cluster. The well-developed stratiform heating profile associated with the ORG cluster along with the increased average surface rainfall rate and dominance by stratiform precipitation (Table 2.1) is an important reason this cluster is considered to be one comprising organized deep convection.

Due to the fact that stratiform rainfall production in the tropics is considered primarily to be the result of convective activity (when considering a large enough spatial scale), a sole-stratiform rainfall cluster is not observed in this study. Therefore, the issue

could arise where stratiform rainfall is significant outside of our identified clusters, far removed from convective towers. The right panel of Fig. 2.5 shows that the $Q_{1\text{-}R}$ profiles associated with the residual stratiform rainfall for each geographic basin is quite small. The column-average (defined from the ocean surface to approximately 18 km) $Q_{1\text{-}R}$ magnitudes for the residual (or unclassified) locations are approximately 0.03 K day^{-1}. This is more than an order-of-magnitude smaller than the average SHAL cluster column-average stratiform and convective $Q_{1\text{-}R}$ combined. Considering that these samples make up less than 10% of the number of raining samples, the contribution to total rainfall and $Q_{1\text{-}R}$ is minimal.

The total $Q_{1\text{-}R}$ for each cluster and each basin is shown in Fig. 2.6, and is mathematically equivalent to the addition of the convective and stratiform components in each precipitation cluster. The column-average total $Q_{1\text{-}R}$ magnitudes for the clusters are provided in Table 2.1. Regarding the profile characteristics, the SHAL cluster $Q_{1\text{-}R}$ peaks near 2 km (Fig. 2.6, center panel), and the total $Q_{1\text{-}R}$ profiles in the UNORG and ORG clusters peak much higher in the atmosphere (6 – 8 km for the ORG cluster). These

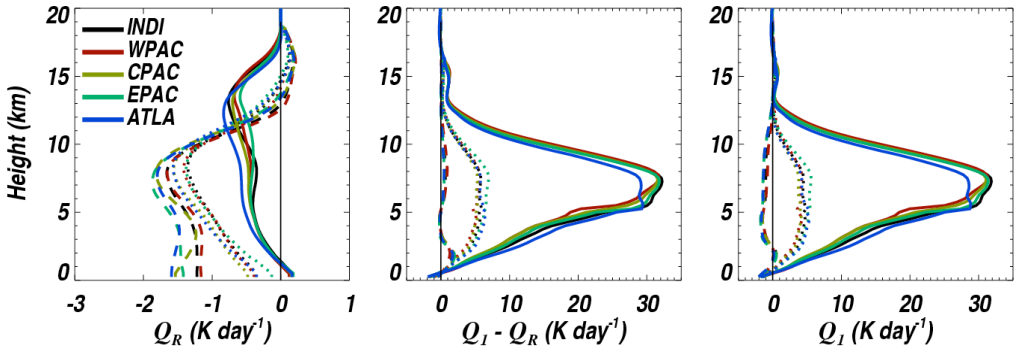

Figure 2.6. The Q_R ($Q_1 - Q_R$, Q_1) profiles for each of the precipitation clusters and basins are shown in the left (center, right) panel. The clusters are indicated according to line style as in Fig. 2.5.

peaks are both consistent in magnitude and altitude across all tropical ocean basins.

The radiative heating (Q_R) profiles for all clusters and basins are shown in the left panel of Fig. 2.6. Since the HERB Q_R algorithm uses additional, independent satellite observations for the cloud-field characteristics and geometry, investigating the Q_R profiles for each cluster and for all basins can provide additional insight into the similarity of precipitation clusters. As the precipitation cluster becomes deeper, the cooling below about 11 km decreases in magnitude, likely from the effect of increasing cloud cover at all altitudes leading to a decrease in the radiative flux divergences. Near the surface, as the intensity of the cluster increases (SHAL to ORG), Q_R rapidly approaches 0 K day^{-1}, presumably because of an increasing peak in total cloud cover in the lowest levels of the atmosphere (typical of more convectively-active regimes) and the associated increasing downward directed LW flux. The opposite trend occurs above 11 km, where radiative cooling increases as the cluster becomes deeper, likely due to the increasing cloud and anvil coverage in the 10-15 km range and the associated LW cooling to space that occurs in the vicinity of higher cloud tops. Increased cooling in the ORG cluster aloft could also be due to increased upper-tropospheric water vapor associated with detraining deep convection leading to increased LW emission. The column-average Q_R magnitudes are shown in Table 2.1. These Q_R magnitudes are quite different from each other, suggesting significant differences in the cloud fields from one cluster to another. However, the average differences of these magnitudes with respect to the cluster-stratified Q_R magnitudes are on the order of 5% for all basins. This implies that given the presence of a particular precipitation cluster, the cloud fields across the tropical geographic basins are fairly similar.

Given the Q_R and $Q_{1\text{-}R}$ components of diabatic heating, the apparent heat source Q_1 can now be quantified for each cluster and basin (Fig. 2.6). $Q_{1\text{-}R}$ is much larger in magnitude than Q_R in heavily precipitating clusters (due to the effects of latent heating), and therefore Q_R serves to only slightly shift (negative direction) the $Q_{1\text{-}R}$ profiles for the UNORG and ORG clusters, while Q_R has a larger impact in the weakly convecting SHAL clusters since $Q_{1\text{-}R}$ is comparable in magnitude. In these commonly observed SHAL clusters, Q_1 shows cooling throughout the troposphere above 2-3 km, and warming below due to the action of precipitating shallow cumulus clouds.

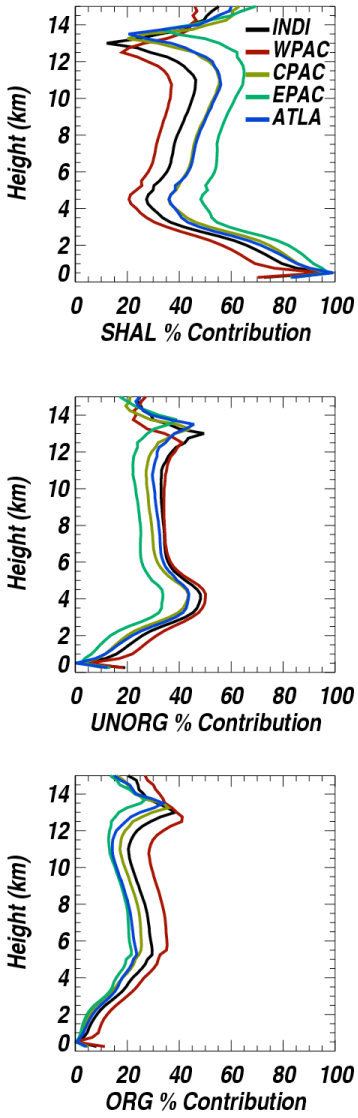

Figure 2.7. The percent contribution to the average Q_1 by each precipitation cluster (as a function of altitude) for each ocean basin.

Provided with the relative frequency of occurrence of each cluster as a function of geographic basin, one can now assess the contribution each cluster makes toward the statistical basin-averaged Q_1 profiles (bottom panel of Fig. 2.1). The 2 km peak in Q_1, evident in all basins, is largely the result of the unimodal SHAL clusters present in most tropical oceanic locations. Specifically, 80% of the magnitude of this peak can be attributed to the SHAL clusters (top panel of Fig. 2.7), a

consistent result seen from one basin to the next. The next peak in Q_1, centered near 8 km, is contributed to heavily and almost equally by all clusters. The warming by convection in the UNORG and ORG clusters contributes positively to this peak, while radiative cooling in the SHAL clusters contribute negatively and decrease the magnitude of this peak. Since deeper clusters are less prevalent in the eastern Pacific and Atlantic Oceans, the Q_1 magnitude at this altitude is closer to 0 K day^{-1} (Fig. 2.1) since radiative cooling from the SHAL clusters overwhelms the heating by the less prevalent deeper convective clusters.

2.3.3 Cloud Type Contributions to Cluster Q_1 Profiles

While a precipitation cluster is characterized according to the most prominent, vertically extended cloud type, other precipitating cloud types consistently coexist in the deeper clusters. There are three prominent peaks in convective cloud PTHs that are clearly seen in the bottom two panels of Fig. 2.2: the first peak extends from 0 – 5 km, the second from 5 – 9 km, and the third (mostly a ORG feature) encompasses the deeper convective clouds with precipitation tops extending from 9 – 20 km. These three broad peaks are likely the result of often-observed precipitating convective clouds and can loosely be classified as precipitating shallow, congestus and deep clouds, consistent with the definition provided by Johnson et al. (1999) and others. Since clusters have been shown to consist of well-defined cloud ensembles, independent of the basin under study, then it is worthwhile to proceed with an investigation of the role each cloud type plays in terms of net heating observed in a cluster.

In the top left panel of Fig. 2.8, the average UNORG cluster Q_1 profile is reconstructed by sequentially adding in progressively shallower precipitating convective

clouds and associated $Q_{1\text{-}R}$ profiles to the combined average stratiform $Q_{1\text{-}R}$ and Q_R profiles representative of the cluster. In the top right panel of Fig. 2.8, the relative importance (in terms of % contribution) of particular cloud types (stratiform, shallow, congestus and deep convective) to the UNORG Q_1 profile is shown. The uppermost part of the Q_1 profile in the UNORG cluster (above 7 km) is mostly reproduced by the stratiform component of $Q_{1\text{-}R}$ (see 90% contribution by Strat + Q_R profile in top right panel of Fig. 2.8). The lower half of Q_1 (lower than 7 km) is nearly reproduced upon the addition of the congestus cloud $Q_{1\text{-}R}$ (40-80% of peak is the result of heating by these clouds). Adding in the shallow convective cloud $Q_{1\text{-}R}$ allows for a broadening of the lower portion of the profile (1 – 2 K day^{-1}) as indicated by comparing the dashed to solid line in the top left panel of Fig. 2.8. Heating by shallow convection is responsible for 20% of the Q_1 magnitude near the surface (solid line in top right panel), with significant cooling resulting from evaporation of precipitation and radiative cooling as indicated by the Strat + Q_R profile. Shallow, congestus and stratiform cloud types all contribute in significant, but varying degrees (as a function of height) to the net UNORG cluster Q_1, and do so in a consistent manner for each ocean basin.

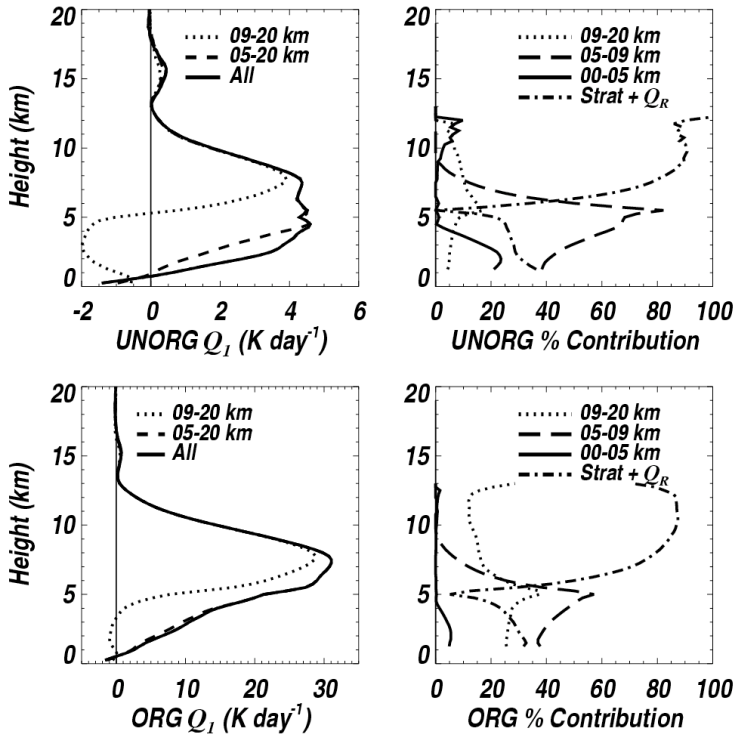

Figure 2.8. The top left panel illustrates the reconstruction of the average UNORG Q_1 profile, computed by successively adding the average convective $Q_1 - Q_R$ profiles (associated with 3 specified subsets of convective cloud ensembles) to the combined stratiform $Q_1 - Q_R$ and average Q_R profile characterizing the cluster. The 3 convective ensembles consist of clouds with PTHs ranging from 9-20 km (dotted), 5-20 km (dashed) and 1-20 km (solid). The top right panel illustrates the contribution by cloud type ensemble (stratiform, and the three convective ensembles) to the average Q_1 profile characterizing the UNORG cluster. The bottom two panels are constructed as in the top two panels, but for the ORG cluster.

Considering now the ORG cluster, and proceeding as before, successively shallower $Q_{1\text{-}R}$ profiles are added to the ORG cluster combined stratiform $Q_{1\text{-}R}$ and Q_R profiles towards reconstruction of the cluster average Q_1. It is evident that the positive lower portion of Q_1 emerges after the congestus $Q_{1\text{-}R}$ is taken into consideration (the congestus clouds contribute 40-60% towards the net heating, slightly larger than the contribution by deeper (9-20 km PTHs) clouds). The role of the shallower convective clouds (consisting of PTHs from 0 – 5 km) is not as significant in the ORG cluster as in the

UNORG one (seen by comparing dashed to solid line in bottom left panel), contributing only slightly to the magnitude of the Q_1 profile from 1 – 4 km. The upper-most portion of ORG Q_1 (above 7 km) is largely reproduced upon consideration of the deep convective precipitating cloud (PTHs from 9-20 km) and stratiform component of heating.

2.4 Dissimilarity in Precipitating Cloud Types

An attempt has been made to show that precipitation clusters are similar in appearance, with nearly indistinguishable cloud ensembles, rainfall distributions and heating profiles. It is worth discussing whether or not the idea of self-similarity can be extended to specific precipitating cloud types. For instance, does a precipitating congestus cloud observed in one precipitation cluster look similar to that in another cluster in terms of surface rainfall rate and vertical profile of radar reflectivity? While deep convective clouds produce a significant amount of rainfall and latent heating, shallow and congestus cloud types (defined as earlier according to their PTH distributions), due to their significant RFO over the tropical oceans, contribute roughly 38% and 47% of the observed total convective rainfall, respectively. Because these clouds are particularly important in terms of rainfall in the tropics, the idea of cloud type similarity is discussed through consideration of particular precipitating clouds within the broad shallow and congestus classifications.

Consider two particular precipitating cloud types within these categories that have PTHs of 3 and 6 km. The cloud with a 3 km PTH can be considered a shallow, warm-raining cloud, while the 6 km precipitating cloud most likely extends beyond the tropical freezing level and may contain ice near the cloud top. Stratified by precipitation cluster, the average surface rainfall rate for a cloud with a 3 km PTH (at TRMM PR instantaneous resolution) is 2.1, 1.5, and 1.4 mm hr^{-1} for SHAL, UNORG and ORG clusters, respectively. As the cluster becomes deeper, the strength of the 3 km precipitating clouds decrease in terms of surface rainfall rate, which is somewhat surprising, but nonetheless consistent for all basins. Figure 2.9 depicts the $Q_{1\text{-}R}$ and radar reflectivity profiles for the 3 km clouds in

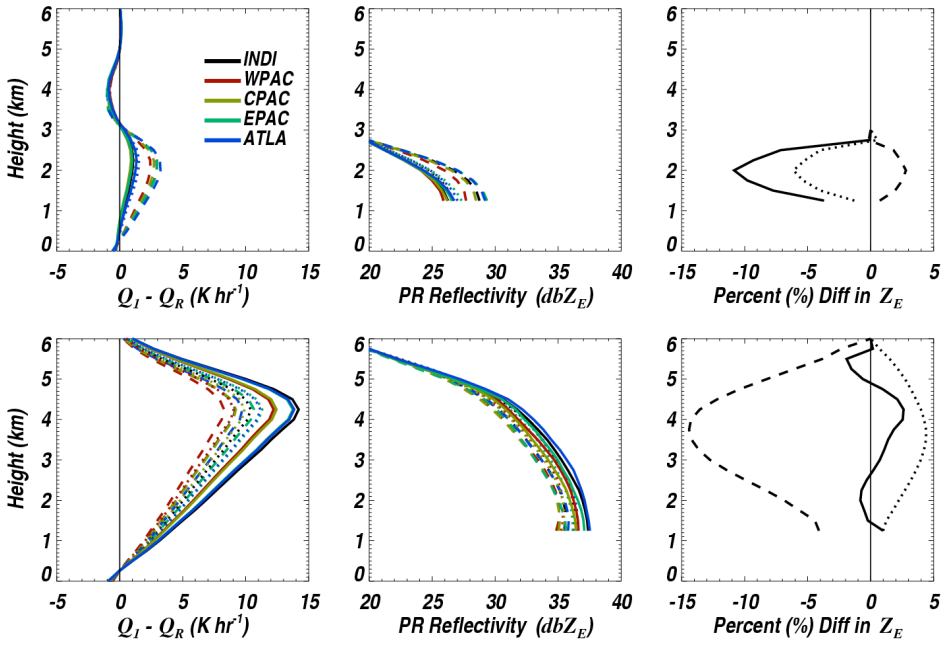

Figure 2.9. The top left panel illustrates the average convective $Q_1 - Q_R$ profiles for convective clouds having PTHs of 3 km for each precipitation cluster (dashed denote SHAL, dotted denote UNORG and solid denote ORG clusters). The top middle panel is constructed as in the top left panel, but for the PR Z_E profiles. The top right panel illustrates, for each precipitation cluster (line-style denotes the cluster), the percent difference in Z_E as a function of height given a convective cloud with a 3 km PTH and the same surface rainfall rate (averaged over all basins). The bottom two panels are constructed as in the top two panels, but for the precipitating clouds having PTHs of 6 km.

the top three panels. One would expect that the $Q_{1\text{-}R}$ from these 3 km cloud types should decrease, consistent with the surface rainfall rate trends, which is indeed what is observed. It must be noted that $Q_{1\text{-}R}$ can be considered a larger-scale variable dependent on the precipitating cloud system as a whole, so further interpretation of the $Q_{1\text{-}R}$ profiles would be more speculative. The top middle panel of Fig. 2.9 shows the corresponding 2A25 product radar reflectivity profiles for the 3 km precipitating clouds. Consistent with the rainfall rates, as the precipitation regime grows deeper, the radar reflectivity profiles weaken for these cloud types. The $Q_{1\text{-}R}$ and radar reflectivity profiles for the clouds with 6 km PTHs are shown in the bottom three panels of Fig. 2.9. For a precipitating cloud with a 6 km PTH, the average surface rainfall rate is 7.5, 8.2, and 10.7 mm hr^{-1} for SHAL, UNORG and ORG clusters, respectively. Unlike the trend for clouds with 3 km PTHs, the rainfall rate, $Q_{1\text{-}R}$ and radar reflectivity values increase as the clusters transition from SHAL to ORG (bottom left and bottom center panel of Fig. 2.9). This is also qualitatively consistent from one geographic basin to the next.

If one becomes more stringent in the definition of a precipitating cloud type such that it is now defined by both a particular vertical thickness and surface rainfall rate, then further investigation into the differences in the profiles of radar reflectivity as a function of height for the three clusters can be made. The results are averaged over all basins, and the average percent difference in radar reflectivity relative to the mean radar reflectivity profile is shown for precipitating clouds defined according to PTH and surface rainfall rate. The results can be seen in the far right two panels of Fig. 2.9. Robust differences emerge, and for the 3 km clouds, given the same surface rainfall rate, there is 14% difference in radar reflectivity at 2 km between precipitating clouds developing in the SHAL cluster versus the

ORG cluster. For the 6 km clouds, given the same surface rainfall rates once again, there is an 18% difference in radar reflectivity at 3.5 km between precipitating clouds developing in the SHAL cluster compared to those developing in the UNORG cluster.

It is evident that the differences between these average surface rainfall rates, $Q_{1\text{-}R}$ and radar reflectivity are large and highly dependent on the precipitation regime in which the cloud is developing. However, the rainfall rates are similar with respect to the tropical average surface rainfall rate for these clouds when one stratifies by precipitation cluster (less than a 7% difference from the cluster average). These results provide motivation for the study of precipitating clouds within the context of the precipitation regime in which they are developing, as opposed to considering precipitating clouds with the same vertical extent and/or rainfall characteristics as self-similar entities, independent of the precipitation regime.

2.5 Conclusions

A wealth of knowledge exists on the nature of tropical precipitation, both in the temporal-mean sense and also with respect to the prevalence of precipitating clouds as one traverses the various ocean basins in the tropics. In this study, an analysis geared towards extracting precipitation regimes from the mean tropical state is performed, but is done so independently for adjacent ocean regions with the purpose of determining how similar various precipitation regimes are across the tropics. The framework has the advantage of not requiring, for example, the specification of how many deep precipitating clouds must exist in a regime for it to be declared "deep" or what percentage of stratiform/convective cloud types must exist in a given area for a particular type of regime to be defined. Three

similar precipitation clusters emerge such that a particular cluster occurring in one basin is nearly indistinguishable from the same cluster identified in another basin. Clusters are quantitatively similar in terms of the ensembles of cloud types, the distributions of rainfall, and the distributions of heating resulting from the spectrum of precipitating clouds present. Precipitating shallow and congestus clouds are in close proximity to each other, as well as in close proximity to deep convective clouds in deeper precipitation clusters. Because a cluster contains a distribution of cloud entities that are not self-similar (despite having the same vertical extent and rainfall), studies that focus on a particular cloud type and its associated ambient thermodynamic characteristics may inadvertently mix regimes by, for example, extracting shallow clouds from a deeper convection regime and shallow clouds from a weakly-convecting regime and compositing the profiles and their corresponding environmental characteristics together.

Within the deeper precipitation clusters, the distributions of PTHs are consistently bimodal. It is shown that particular ensembles of cloud types play significant roles in the composite structure of the heating profiles. These results are robust, and consistent from one tropical ocean basin to the next. Additionally, these results indicate that it may be necessary to consider the entire spectrum of precipitating clouds present in a particular regime in order to capture the heating profile (largely driven by the latent heating term), beyond a rainfall scaling of a generalized latent heating function that depends largely on the amount of stratiform and convective rainfall present.

It is an important result that similar precipitation clusters emerge, particularly since equatorial atmospheric wave activity frequency and large-scale dynamics vary as a function of tropical oceanic basin. Considering that convectively coupled equatorial waves are more

prevalent in some basins than others and that the Madden-Julian Oscillation (MJO) primarily influences the Indian and west Pacific Ocean basins, the result of cluster similarity in terms of the distributions of PTH, rainfall and heating is a significant one, implying that precipitation clusters do not change regardless of the type of equatorial disturbance, and instead, are simply modulated in terms of frequency of occurrence by the disturbance.

Continued interpretation of these clusters, as well as their placement within the "Extended Building Block" hypothesis recently proposed by Mapes et al. (2006) that describes a self-similar progression of precipitating convection from shallow to deeper structures despite being modulated by different large-scale tropical waves, requires the incorporation of additional data sets describing the thermodynamic and dynamical states of the atmosphere. Furthermore, reconciling the remaining cluster differences that exist from one basin to another may require consideration of the idea that some precipitation regimes may be either terminal (i.e. they have reached their peak intensity) or transient (i.e. intensifying and growing towards a deep convective state), as discussed in Luo et al. (2009). It is possible that the same distribution of precipitating clouds could exist in either case, but there is good reason to expect that the heating and rainfall may be different between the two cases, which could provide some insight into why precipitating clouds have similar characteristics with respect to the cluster in which they are developing, but not with respect to the same cloud-types developing in another cluster.

CHAPTER 3

AN OBSERVATIONAL DEPICTION OF THE TRANSITION FROM LIGHT TO HEAVY RAINFALL OVER SHORT TIMESCALES

3.1 Introduction

Over the last decade, considerable progress has been made in quantifying the spectrum of precipitation systems that exist in the tropics and subtropics, particularly over the oceans. This is in large part due to the diverse collection of low-Earth orbit satellites that employ payloads designed for observing upwelling radiation from clouds and water vapor at a resolution sufficiently high for inferring the distribution of raining clouds over any desired tropical or subtropical oceanic region. Observations have shown that roughly 2/3rds of the global rainfall falls equator-ward of 40°, and of this rainfall, 3/4ths of the volumetric accumulation is attributed to mesoscale convective systems (MCSs) that comprise only 10-20% of all raining systems (Mohr et al. 1999), while the frequently-occurring "warm-rain systems" containing ensembles of clouds with tops terminating below the freezing level account for the remaining accumulation (Liu and Zipser 2009). The contribution to the temporal mean rainfall by both shallower collections of raining clouds and deeper, more organized systems is location dependent, and is a function of the mean atmospheric background state.

Despite the fact that the mean precipitation states vary across the tropical oceans, a few recent studies have found that various statistical distributions of raining clouds at an approximate 1-2° spatial scale exhibit notable similarity (e.g. Liu and Zipser (2009), Chapter 2 of this dissertation) to the extent that when they occur, they are almost indistinguishable from one tropical ocean basin to another. With respect to shallower raining regimes, Liu and Zipser (2009) found no substantial regional differences in the spatial extents and rainfall intensities of warm-rain precipitation systems in the tropics. In Chapter 2, precipitation regimes were investigated independently at a 1° spatial scale for adjacent tropical ocean basins through use of a KMEANS clustering technique. It was shown that collections of raining clouds at the 100 km spatial scale resemble each other in a statistical sense in terms of raining cloud populations, precipitation top height distributions, ensemble vertical heating profiles and distributions of surface rainfall. This was found regardless of whether the regime as a whole could be classified as shallow or deep.

Studies such as these imply that significantly different mean rainfall states (such as the west Pacific basin versus the east Pacific basin) are composites of similar precipitation regimes recurring at varying, basin-dependent relative frequencies of occurrence (RFOs). An alternative interpretation is that regions with different temporal-mean atmospheric states transition through similar shallow and deep precipitation regimes, but do so at varying rates leading to significantly different rainfall lifecycles. These rainfall lifecycles would likely reflect a diurnal timescale signature along with multi-day variations in rainfall due to propagating convectively coupled waves. Continued progress in understanding these cycles and the evolution from one regime to another is clearly related to the more general problem of resolving what processes dictate the transition from shallow to deep

convection over varying timescales. This line of inquiry has enjoyed much investigation recently, mostly from a modeling (e.g. Derbyshire et al. 2004; Khairoutdinov and Randall 2006; Kuang and Bretherton 2006; Wu et al. 2009) or field campaign perspective (e.g. Kingsmill 1995; Pereira and Rutledge 2006; Lima and Wilson 2008). While large-scale (i.e. current spatial scales of present-day general circulation model (GCM) grid boxes) parameters related to buoyancy, water vapor and shear are clearly important in regulating shallow and deep precipitation states and their transitions, unresolved fluctuations in atmospheric water vapor, buoyancy and wind velocity and the role this may play in convection evolution on the scale of a GCM grid-box is now receiving significant attention. Analyses of inhomogeneity existing in large-eddy simulation and cloud resolving model (CRM) fields relative to the convection state have proven useful in this regard.

In regards to a GCM representation of convection, there are a number of missing processes (unresolved in current coarse-grid, parameterized GCMs) in these models that have been identified as important for capturing the evolution of convection. These include cold pools and the role they play in deep convective cloud development through thermodynamic effects (Tompkins 2001) or forced lifting of surface parcels above their inhibition barrier (e.g. Mapes 2000; Lima and Wilson 2008; Khairoutdinov et al. 2009; Hohenegger and Bretherton 2011), environmental shear and its interaction with convection regimes (Moncrieff and Liu 2006), water vapor variations at small scales and the effect they may have on subsequent cloud development and organization (Mapes 2000; Chaboureau et al. 2004; Fletcher and Bretherton 2010; Mapes and Neale 2011), and processes allowing for shallow clouds to become buoyant relative to the mean environment promoting the rapid development of deep cloud (Wu et al. 2009).

Of the processes mentioned, consider for the moment that some studies (Tompkins 2001; Ross et al. 2004; Moeng et al. 2009) have shown that cold pool activity can significantly impact horizontal wind velocity at a 10-30 km scale. In light of these spatial scales, the opportunity exists to exploit higher-resolution satellite products in pursuit of a signal related to cold pool activity and evolving larger-scale state of convection. Fortunately, the QuikSCAT satellite orbital and viewing characteristics are such that wind velocity can be retrieved at a scale of ~25km, roughly equivalent to the scales discussed above. Therefore, a key element of this study is the focus on variability in surface wind fields estimated by the QuikSCAT satellite over the tropical oceans.

A new observational parameter related to cold pool activity is developed in this paper that captures the variability in surface wind fields hypothesized to be largely associated with cold pools. The overarching goals of this study include determining to what extent existing space-borne platforms can detect cold pools and furthermore, shed light on existing ideas related to cold pools and their influence on the transition from shallow to deep convection. It should be noted that while most prior modeling studies have discussed transition in the sense of progression from shallow (i.e. non-precipitating) clouds to rainfall, transition defined here specifically focuses on progression from shallow rainfall (i.e. warm-rain dominated; cloud tops well below freezing level) to heavier rainfall associated with organized aggregates of deep convective clouds.

In this analysis, temporal composites of rainfall, cold pool activity, convective available potential energy (CAPE), convective inhibition (CIN) and relative humidity, centered on local rainfall maxima, are constructed. In documenting the evolution from shallow to deeper rainfall, high temporal resolution is desired through the sole use of

observational platforms. This is accomplished through use of multi-sensor satellite products and radiosonde data, merged in such a manner that 3-6 hour resolution can be achieved.

3.2 Observational Datasets

All data and derived parameters used in this study span the time frame extending from 2004 to 2007. The CPC MORPHing (CMORPH) product (Joyce et al. 2004) serves as the basis for rainfall observations. This technique relies on rainfall estimates derived exclusively from a number of orbiting passive microwave sensors. These estimates are propagated in time/space through use of geostationary infrared (IR) data such that global estimates of rainfall rates are produced at an approximate spatial and temporal resolution of 10 km and 30 minutes, respectively.

Twice-daily surface wind velocity information, available over all oceanic regions, is derived from the SeaWinds scatterometer on the QuikSCAT satellite. Details on scatterometry, applications and instrument specifications can be found in Freilich et al. (1994), Liu (2002) and Chelton and Freilich (2005). Through the use of a geophysical model relating wind stress, ocean emissivity and backscattered radiation at multiple azimuth angles, surface wind velocity can be retrieved. As mentioned, retrievals are available at the 25 km spatial scale and are calibrated to a 10-m reference height. The wind vector retrievals serve as the basis for defining cold pool activity.

Rain probability from the scatterometer is determined using the Multidimensional Histogram (MUDH) rain flag algorithm (Huddleston and Stiles 2000). Because wind vector retrievals may be degraded when rainfall is present, rainfall probabilities provided

by this algorithm are used to remove pixels potentially contaminated by rainfall. Given that there is no stated rainfall rate or rainfall probability beyond which the wind retrieval becomes invalid (Liu 2002), a rainfall probability of ≥ 50% is used as the threshold for filtering pixels potentially contaminated by rainfall. As there often is some finite probability of rainfall over the tropical oceans, this choice strikes a balance between discarding a substantial percentage of useful retrievals by either over-flagging (> 0% threshold) or under-flagging pixels likely contaminated by rainfall. Additionally, if the MUDH rain flag is not usable for any cell, the retrieval is immediately discarded.

Buoyancy and relative humidity characterizing the environment are derived from radiosonde observed (RAOB) water vapor and temperature profiles. These profiles are available from the Integrated Global Radiosonde Archive (IGRA; Durre et al. 2006), and

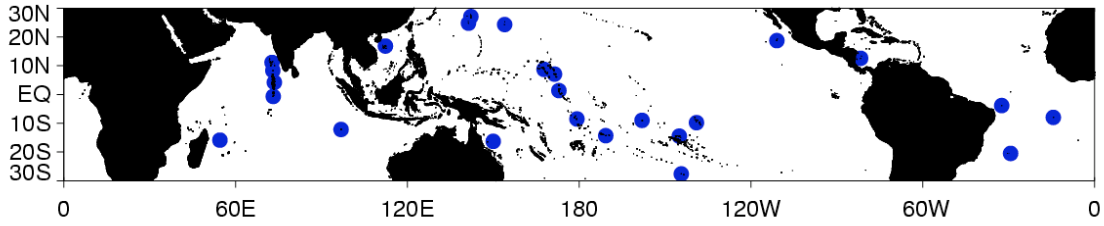

Figure 3.1. Solid circles indicate locations of radiosonde stations.

are produced by the National Climatic Data Center (NCDC). For any given reporting time, a RAOB is used if 1) there is a valid surface report for pressure, temperature and dew point depression and 2) data are available for at least 8 standard pressure levels (1000, 925, 850, 700, 500, 400, 300, 250 hPa). There are 25 RAOB stations used in this study (geographic locations are shown in Fig. 3.1). Since analyses here involve spatial co-location of multiple

datasets, some of which are available for ocean only (e.g. QuikSCAT), only stations located on remote islands are considered.

3.3 Analysis Method

Rainfall data are averaged to 2° and geographically centered on the RAOB launch sites. Given that this spatial scale is representative of the current size of grid-boxes in conventional GCMs or host GCMs in multi-scale modeling frameworks (MMFs), it is a pertinent scale for studying the time evolution of precipitation for convective parameterization purposes.

Cold pool activity is characterized by computing root mean square horizontal velocity fluctuations over the 2° spatial scale. The parameter is referred to as cold pool kinetic energy (CPKE) and is defined as

$$\mathrm{CPKE} = \frac{1}{2}\left(\overline{u'^2} + \overline{v'^2}\right), \tag{3.1}$$

where the primes denote departures from the spatially averaged 2x2° zonal (u) and meridional (v) wind components, and the over-bar indicates an average over the entire grid box. This mathematical formulation is the same as that for turbulent kinetic energy (TKE). However, the horizontal scale of turbulent eddies is typically considered to be approximately related to the depth of the planetary boundary layer [O(1km)]. The horizontal scales being investigated here are on the order of 10-30 km, and therefore, a new interpretation is warranted. Since frontal activity is typically non-existent over the deep tropical oceans, boundaries over open-ocean that would influence the variance in

surface wind are likely related to cold pool outflow from nearby regions of convection. This interpretation is also based on the observation that CPKE tends toward zero as rainfall does, as will be shown in later sections.

In order to visualize the variations of CPKE alongside surface rainfall rates, a snapshot of QuikSCAT surface wind, CPKE and CMORPH rainfall is shown in Fig. 3.2.

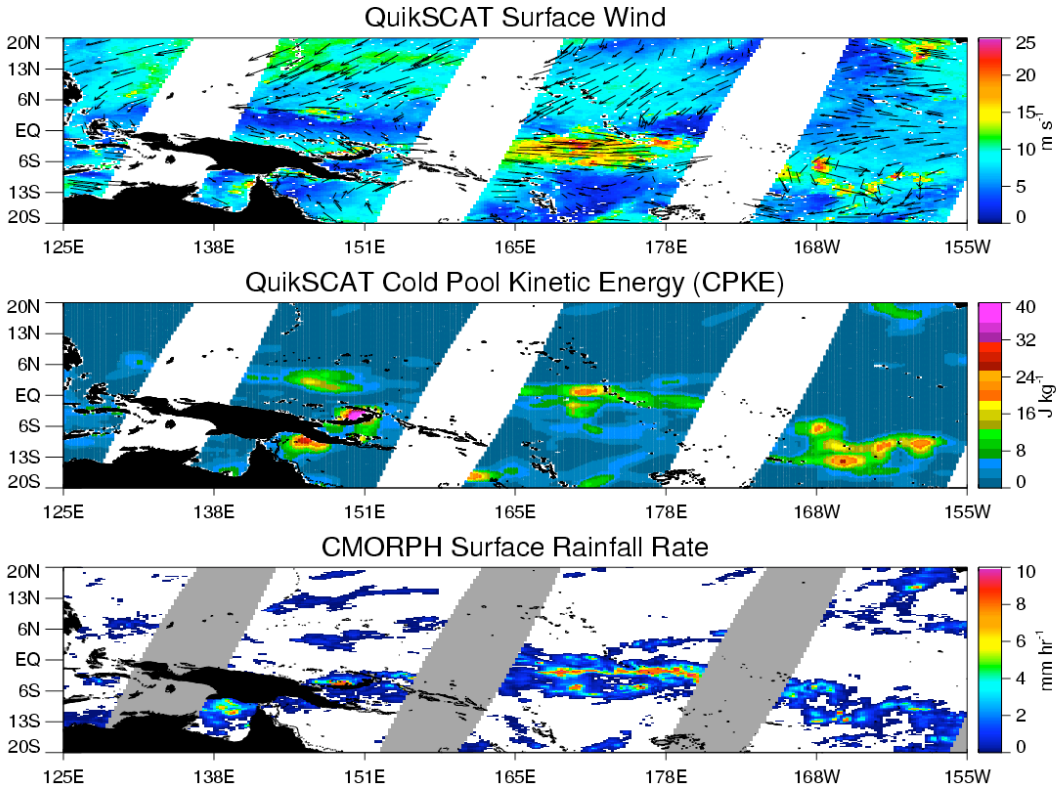

Figure 3.2. Sample snapshots from 01 Jan 2004 of QuikSCAT orbital and CMORPH products.

The regions where QuikSCAT orbital geometry did not allow for wind sampling are shaded grey in the rainfall panel for easier comparison. In a qualitative sense, a relationship between CPKE and rainfall is evident over oceanic regions.

Saturation fraction, CAPE and CIN are calculated using RAOB data. The saturation fraction, defined as

$$\text{SatFraction} = \frac{\frac{-1}{g}\int_{psfc}^{ptop} q_v dp}{\frac{-1}{g}\int_{psfc}^{ptop} q_{v,sat} dp}, \tag{3.2}$$

is equal to the column integrated mixing ratio (TPW) divided by the column-integrated saturation mixing ratio, calculated by determining the saturation water vapor mixing ratios given the RAOB temperature profiles. It is therefore a measure of the column-integrated relative humidity. Bretherton et al. (2004) has shown that this parameter is highly correlated with rainfall, although the direction of causality is still not completely established. CAPE and CIN are calculated using the method developed by Emanuel (1994). The traditional definition for CAPE as a measure of the energy available for convection is used here, such that it is computed by vertically integrating the local buoyancy of a parcel from its level of free convection to its equilibrium level. CIN represents a potential barrier to convection, and is defined as the vertical integral of the virtual temperature difference between the environment and the parcel below the level of free convection.

Local maxima in geo-located rainfall are defined through consideration of a 6-hr smoothed rainfall time series at each station. The original time series of rainfall, CPKE, saturation fraction, CAPE and CIN are composited about all local rainfall maxima from 0 - 4 mm hr^{-1}, which encompasses virtually all rainfall variation at the 200 km spatial scale, so that temporal histories of all parameters relative to varying-magnitude rainfall cycles can be

constructed, yielding convenient two dimensional portrayals of rainfall time tendencies and environmental parameter history versus the maximum amplitude of the rainfall cycle. Because the satellite and RAOB data, even if available at the same GMT time daily, are lagged with respect to local times of rainfall maxima, one can derive the sub-daily time composites given that the CMORPH rainfall product consists of fixed 3-hr sampling.

Two caveats must be mentioned pertaining to the use of the chosen radiosonde sites depicted in Fig. 3.1. While rainfall and CPKE is representative of the 200 km scale, soundings are most likely representative of local environmental conditions, and therefore, noise in saturation fraction, CAPE and CIN will inevitably be introduced. However, given a sufficient number of samples through use of all stations over a 4-yr period, one can largely circumvent this issue. Additionally, despite the fact that launch sites are located mostly over smaller, remote islands such that a 2° rainfall average consists of predominantly oceanic pixels, there will be some influence by land. The extent to which land would have an influence depends on proximity to larger land areas, as well as the size of the individual islands. However, the majority of islands chosen contain land mass coverage less than 200-300 km^2. Recent studies (Robinson et al. 2011; Sobel et al. 2011) have found that islands of this size have a limited influence on average rainfall from the perspective of land versus ocean; therefore, near-vicinity rainfall structures are expected to mostly resemble those characteristic of maritime convection.

3.4 Temporal Evolution

3.4.1 Rainfall

The life cycle of rainfall relative to grid-averaged hour 0 rainfall maxima is depicted in the top panel of Fig. 3.3. In order to facilitate interpretation of this image, consider a rainfall cycle that has an hour 0 maximum of 1.6 mm hr $^{-1}$. The composite of the time-lagged (± 3 days) rainfall can then be found by viewing the horizontal transect anchored to the 1.6 mm hr $^{-1}$ rainfall rate shown on the ordinate. In this case, rainfall quickly intensifies 6 hours prior to the maximum and exhibits a rapid decrease over the following 6-hour period. For all hour 0 maxima up to 4 mm hr $^{-1}$, the composite time series over multi-day periods are displayed. Regarding timescales for rainfall, the diurnal cycle in rainfall is clearly visible, particularly for rainfall histories that correspond to lower-amplitude hour 0 rainfall rates (see the 0.8 to 1.6 mm hr $^{-1}$ transect, for instance), where clear minima in rainfall rate exist 12 hours prior to and after local maxima. The composite rainfall histories corresponding to these lower amplitude hour 0 rainfall rates are the ones most frequently observed, and thus contribute most heavily toward an average history that would be representative of the tropical mean diurnal cycle found in a number of satellite studies.

From the perspective of volumetric accumulation, a significant amount of rainfall is associated with rainfall cycles that correspond to hour 0 rainfall rates greater than 1.6 mm hr $^{-1}$. One can see that the diurnal cycle, while evident, is less visible in these higher-amplitude rainfall states. An envelope of elevated rainfall extending over an approximate 2-day period (± 24 hrs) is clearly visible, with the most substantial increase in rainfall beginning 12 hrs prior to the maximum amplitude. These envelopes of higher-amplitude

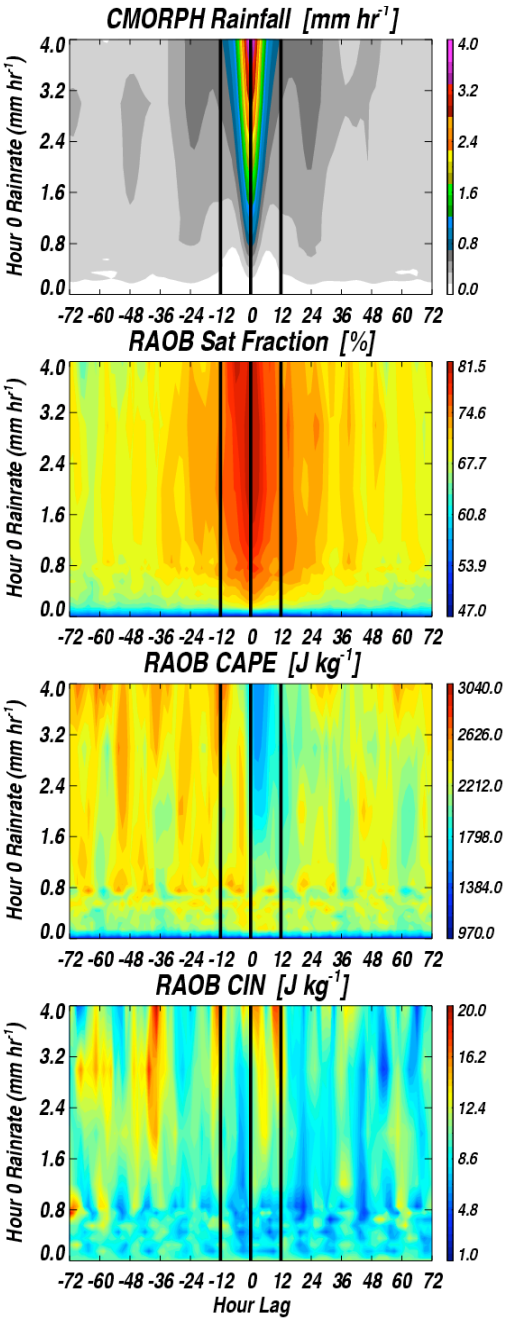

Figure 3.3. Composite temporal evolution of rainfall and radiosonde parameters as a function of local rainfall maximum. Vertical lines at ± 12 hrs are shown for visual reference only.

rainfall cycles are possibly associated with 2-day waves and attendant mesoscale convective systems (MCSs), and likely contribute toward a series of enhanced diurnal cycles. As discussed in section 3.3, despite the interpretation that the rainfall depicted here is largely maritime in nature, it is possible that land exerts some influence on the timing and development of convection, which therefore complicates attempts made to establish local solar times to the times of maximum rainfall.

3.4.2 RAOB Saturation Fraction, CAPE and CIN

The evolution of saturation fraction, CAPE and CIN are also illustrated in Fig. 3.3. The non-raining regime (bottom-most transect along the abscissa in all panels) is characterized by a dry atmosphere and less than 1000 J kg^{-1} of CAPE, with little variability over the 6-day period. Saturation fraction exhibits a general increase over time prior to the rainfall maximum for all cycles, with a tendency for maxima in saturation fraction and rainfall to be co-located in time, consistent with results found for integrated water vapor and rainfall tendencies in Zelinka and Hartmann (2009).

Interesting sequences for CAPE and CIN emerge with respect to varying-intensity rainfall cycles. Regardless of the amplitude of the rainfall maximum, CAPE magnitudes preceding the deepest convection in all cycles appear to be quite similar, thwarting attempts to relate CAPE at any prior time to the rainfall maximum and suggestive of an often-present reservoir of potential energy. More generally though, rainfall maximum aside, a visual comparison of the dissimilar rainfall and CAPE patterns highlight the difficulty one encounters in relating CAPE to rainfall over these sub-daily timescales. While CAPE is considered necessary for convection, its presence doesn't guarantee upcoming rainfall nor

dictate its intensity. This result is not completely unexpected, since CAPE sufficient for convection has been found to exist 90% of the time in another observational study (Sherwood 1999) of the tropics, despite deep rainfall occurring at a frequency far less than this. Depletion of CAPE begins once the appropriate triggering mechanisms are in place for deep precipitation development. In the composite, CAPE reaches a minimum 3 – 6 hours after local rainfall maxima, but is never completely consumed and instead, approaches a magnitude that is comparable to that of non-raining scenes, nicely visualized when one compares the non-raining horizontal transect near the bottom of the panel to a transect oriented vertically and displaced a 3 – 6 hours after the maximum-rainfall axis. The significant decreases in CAPE (40% reduction) likely suggest that, on average, convection is not in equilibrium with the environment.

CIN increases over the entire period of enhanced rainfall, and reaches a maximum 5 – 10 hours after peak rainfall. The increase in CIN is likely due to the combined effects of subsidence warming surrounding deep rainfall and cooling of the lower troposphere by cold pools associated with convective and mesoscale downdrafts. Large values of CIN are found both in non-raining regions and immediately after the time of heaviest rainfall for all rainfall cycles, as can be seen in the bottom panel of Fig. 3.3, confounding attempts to relate near-instantaneous rainfall rate and CIN. Nonetheless, from an evolution perspective, over these timescales, similar trends in CAPE and CIN with respect to rainfall can be gleaned from images presented in the modeling studies of Charboureau et al. (2004) and Khairoutdinov et al. (2009) as well.

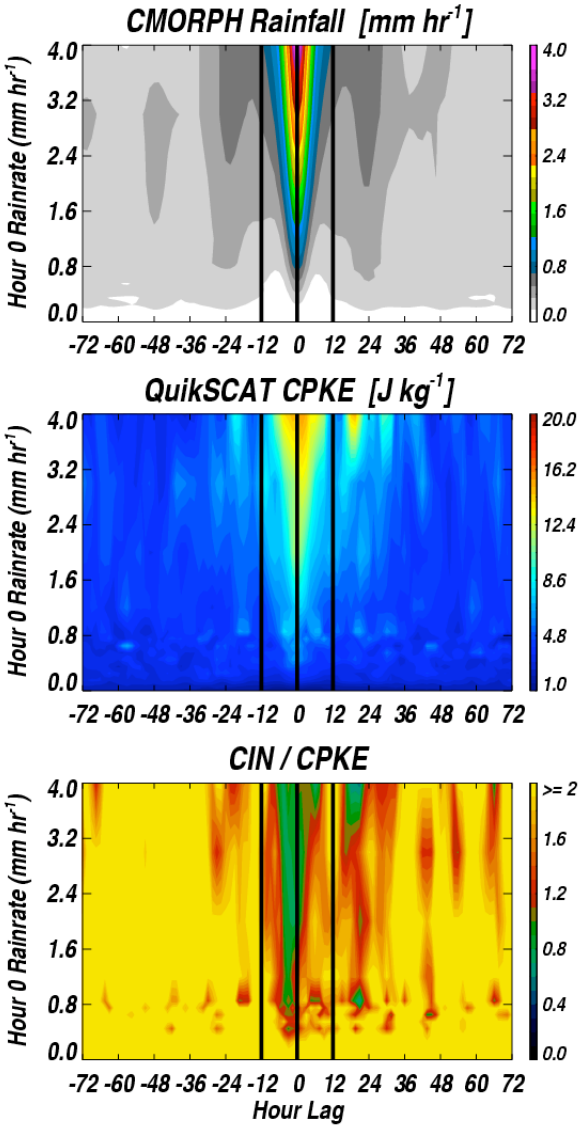

Figure 3.4. As in Fig. 3.3, but with rainfall, QuikSCAT CPKE and the ratio of CIN / CPKE.

For the highest amplitude rainfall cycles, the transition from light to heavier rainfall appears to occur several hours before CIN reaches a minimum. In fact, at a time lag of -24 and -12 hours, similar saturation fractions and CAPE exist, but less CIN exists at -24 hours. Despite this, the increase in rainfall commences at -12 hours, leaving the question open regarding what processes should be considered when developing a conceptual picture of

the hourly-timescale development of deep rainfall, given that a reservoir of CAPE and moisture are present coincident with periods of low CIN well before the increase in rainfall.

3.4.3 QuikSCAT CPKE and Discussion of the Transition from Light to Heavy Rainfall

The rainfall composites are reproduced in the top panel of Fig. 3.4 for qualitative comparison purposes to CPKE, which is shown in the middle panel of Fig. 3.4. It is highly correlated with rainfall, and peak values are coincident with the hour 0 rainfall axis. In the absence of rainfall, there is a tendency to approach negligible magnitudes. Due to similar CAPE, moisture and decreased CIN, the investigation of the transition proceeds along another avenue involving cold pools. Guided by modeling studies, and strictly based on observations here, a working hypothesis for the influence of cold pools on transition from shallow to deep rainfall is twofold: 1) cold pools act to increase the kinetic energy in the boundary layer such that near-surface parcels can acquire enough vertical kinetic energy to overcome the barrier (i.e. CIN) and therefore, this process can result in a positive rainfall time tendency; 2) cold pool activity increases CIN by cooling and drying the boundary layer in the vicinity of convection, thereby acting as a limiting factor on further increases in rainfall. In light of these contrasting effects, efforts to understand the observed transition to deeper rainfall are pursued through consideration of both CPKE and CIN and their ratio.

Despite the lack of consensus, a number of recent modeling results suggest that the transition from shallow, non-raining cumulus convection to precipitating cumulus clouds can be described from the perspective of boundary layer mean vertical turbulent kinetic energy overwhelming grid-mean CIN. A vertical velocity scale can be empirically derived from boundary layer total TKE and compared to a minimum vertical velocity that is

necessary for a parcel to overcome any layer of inhibition that may be capping the boundary layer. When the vertical kinetic energy is sufficient so that this minimum threshold is met, the development of raining clouds commences. This idea, then, is encapsulated by consideration of the ratio of CIN / TKE, and as it approaches unity (or below), the time tendency for cloud growth becomes positive. The idea extends back to Mapes (2000), where the ratio of CIN to "triggering energy" was deemed important for deep convection occurrence. In that study, triggering energy was thought to encompass sub-grid scale fluctuations in equivalent potential temperature, vertical kinetic energy, and gravity wave effects on local variations in CIN. Incorporating the same concept, the modeling studies of Bretherton et al. (2004) and Kuang and Bretherton (2006) investigated the transition from non-raining shallow convection to deeper, lightly raining clouds and Rio et al. (2009), Fletcher and Bretherton (2010), and Hohenegger and Bretherton (2011) have now extended the idea to study transitions over larger rainfall ranges.

From an observational perspective, all smaller scale fluctuations that would contribute to "triggering energy" cannot be determined. In this analysis, with transition defined as progression from shallow rain to deep rain, it is hypothesized that precipitation processes and cold pool effects are even more important than during the transition from non-raining to rainfall onset, and therefore, CPKE can be thought of as a significant triggering mechanism for parcels to overcome CIN. The two parameters are evaluated as a ratio with the intention of casting this observational study within the context of prior modeling results that also considered a ratio.

In Fig. 3.4, as grid-box mean CPKE approaches CIN, the ratio of CIN / CPKE tends toward unity and shallower precipitation begins to rapidly transition to deeper

rainfall. This occurs at time lags closer to -9 to -12 hrs for the deepest rainfall cycles, and -6 hrs for weaker hour 0 rainfall maximum cycles. Observed CPKE magnitudes of ~5 J kg^{-1} are derived and associated with grid-mean rainfall rates less than 1 mm hr^{-1}. This implies that either cold pools have to be in close proximity due to nearby deeper convection, or that shallower precipitating convection itself can produce enough CPKE to start the progression. The initial increase in CPKE by shallow convection is plausible, particularly when one considers that mesoscale organization of shallow raining cumulus convection (<5 km cloud top heights) in association with cold-pool outflows has been recently observed during the Rain in Cumulus over the Ocean (RICO) field campaign (Snodgrass et al. 2009). In the transition, then, shallow raining cumulus may not serve the sole role of preconditioning the atmosphere for deep convection from a moistening perspective, but may also serve the important role of increasing CPKE.

Summarizing results depicted in Figs. 3.3 and 3.4, it is hypothesized that given a sufficient reservoir of CAPE and moisture, as CIN / CPKE decreases such that the two are of comparable magnitude, rainfall increases. In this view, CAPE is seen as a necessary but not determining factor, with high values of CAPE observed for a number of days before the heavier rainfall. Given sufficient CPKE relative to CIN, the depletion of CAPE commences as parcels can acquire sufficient energy to overcome the capping inversion present.

Another view of the timescale for depletion of CAPE and the ratio of CIN / CPKE for three different rainfall cycles is shown in Fig. 3.5. The rapid drop in CAPE takes place roughly during the time interval that CIN $\leq$ CPKE. It can be seen that for the two more intense rainfall cycles, the increase in rainfall begins before the minimum in CIN is realized

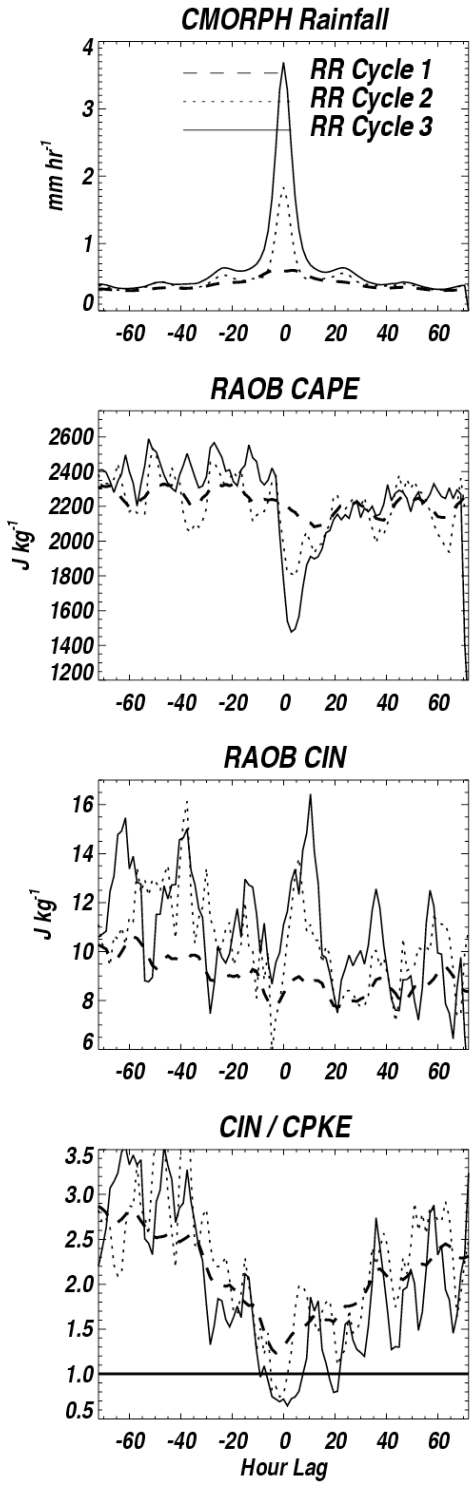

Figure 3.5. Evolution of the background for 3 horizontal slices extracted from Figs. 3.3 and 3.4 representing differing-magnitude composite rainfall cycles.

and continues through the time of rapid increase in CIN. However, the ratio of CIN / CPKE approaches unity before the minimum in CIN and is low throughout, and therefore, rainfall increases several hours before a minimum in CIN is observed and continues increasing after the minimum. For the lightest rainfall cycle (RR Cycle 1), CIN overwhelms CPKE and the time tendency of rainfall is not observed to increase to the extent that it does in the other cases.

The maximum in rainfall occurs near the minimum in CIN / CPKE, shortly after which a minimum in CAPE is observed as well. In the midst of widespread rainfall, CIN experiences a rapid increase for reasons discussed above, and thus CIN / CPKE increases and the convection begins to weaken and CAPE is no longer consumed. When the ratio is sufficiently larger than unity, rainfall tends toward the background average over the cycle. The view presented is one in which the interplay of CIN and CPKE drive the evolution of light to heavier rainfall, with CAPE serving more of a passive role and rarely being completely depleted, since CAPE depletion largely occurs during the period of time that CPKE $\geq$ CIN. Importantly, CIN and CPKE are out of phase with CPKE peaking during maximum rainfall and CIN peaking hours later. This essentially shuts down deep convection, before CAPE is entirely consumed.

The temporal composites are summarized in Fig. 3.6 with the interpretation that non-raining or lightly raining scenes are characterized by CIN exceeding CPKE (right panel of Fig. 3.5), while heavier rainfall is associated with CPKE $\geq$ CIN with the hypothesis being that CPKE approaching and surpassing CIN is a dominant factor in transitioning from light to deeper rainfall.

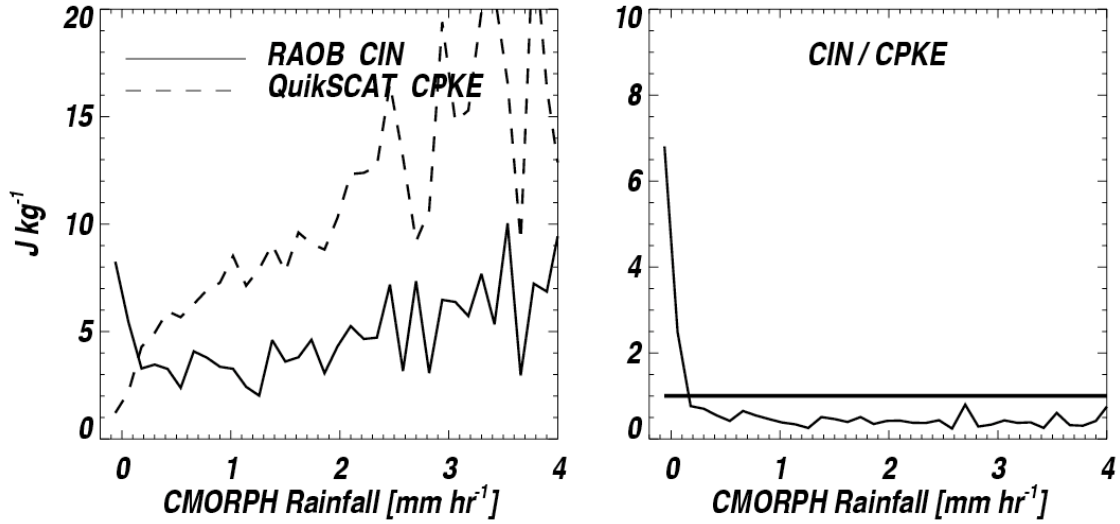

Figure 3.6. Instantaneous CIN and CPKE as a function of rainfall rate.

3.5 Conclusions

Through the exclusive use of observations, an analysis of the lifecycle of rainfall as a function of varying maximum-amplitude rainfall rate was performed. The two-dimensional perspective allows for easy comparison of rainfall and environmental evolution with respect to rainfall cycles that are identified according to progressively more intense hour 0 rainfall rates. Key parameters such as saturation fraction, CAPE and CIN have been discussed and interpreted with respect to prior studies. Generally, CAPE and periods of decreased CIN are observed without the development of heavier rainfall. It is

observed that for more intense rainfall cycles, significant reductions (~ 40%) in CAPE occur, suggesting that on average, periods of heavy rainfall and associated CAPE consumption are not in equilibrium with large-scale CAPE forcing. Heavy rainfall, on average, may occur in the absence of strong forcing as inferred by the significant reductions in CAPE that occur in the presence of elevated rainfall.

Recent modeling studies have begun to focus on sub-GCM scale processes as they relate to strengthening convection. Of these, one line of pursuit has involved investigating TKE and CIN. Provided with enough TKE, it is thought that boundary-layer parcels may acquire a minimum vertical momentum to overcome CIN present in the environment. These same studies have largely focused on the transition from non-raining shallow clouds to deeper ones, whereas the analysis here extends the idea to rainfall regimes at the 2° scale and focuses on the transition from light to heavily raining regimes through consideration of cold pool activity. Cold pool activity is summarized in a parameter with energy units (CPKE) and averaged over the same 2° scale. In this analysis, CPKE takes the place of TKE in the side-by-side comparison with CIN as it is now considered the significant lifting mechanism for situations such as these. The motivation to detect cold pool activity from space arises from previous modeling results that suggest signals may exist at the 25 km scale. It is argued that the envelope of increased rainfall is marked by the period over which CPKE approaches the magnitude of CIN. This period also outlines the time during which rapid depletion of CAPE occurs. CIN itself is a function of cold pool activity. Therefore, as rainfall progresses, cold pool activity may have the effect of increasing CIN to such an extent that it eventually overwhelms CPKE thus leading to a quick decrease in rainfall.

Because the transition is discussed here in terms of cold pool activity, cold pools either need to be generated by nearby deeper convection or by shallow raining clouds. The association with shallower raining clouds is supported by recent data collected during the RICO campaign, as discussed. This suggests that shallow raining clouds may serve as agents for increasing CPKE in addition to their role of moistening the lower atmosphere. CPKE, or "triggering energy" in general, should really be representative of the entire boundary layer, and ideally should be converted to a vertical kinetic energy since vertical motions impinging on a stable lower atmosphere and contributing to cloud base mass flux is the true process that should be investigated as it pertains to the transition process. However, this is where the observational approach is limited, given that retrievals are surface-based and attempts to convert to vertical kinetic energy values representative of the boundary layer would require additional assumptions and empiricism beyond observations. This also implies that CPKE approaching the magnitude of CIN should be thought of as an outline for determining the envelope of heavier rainfall. Specific magnitudes for CPKE and the ratio of CIN / CPKE should be reserved to the time when the vertical component of kinetic energy is derived since that is what is most desired, although it is expected to be strongly related to CPKE.

This work represents the first attempt to use satellites in the investigation of one aspect of variability unresolved by a GCM and considered to be important in rainfall transition as revealed by high-resolution modeling studies. In conjunction with model-based investigations, it is hoped that existing observational platforms and techniques can be utilized further to gain additional insight regarding the role horizontal variability on sub-GCM scales play in the transition from shallow rainfall to deeper convection.

CHAPTER 4

A COMBINED MULTI-SENSOR OBSERVATIONAL AND MULTI-SCALE MODELING FRAMEWORK VIEW OF RAINFALL AND ENVIRONMENT EVOLUTION

4.1 Introduction

Since the advent of the Tropical Rainfall Measuring Mission (TRMM, Kummerow et al. 1998), a more complete observational depiction of the vertical structure of rainfall and implied diabatic heating has been derived for geographic locations equator-ward of 40 degrees latitude. The high-resolution vertical and horizontal information provided by the TRMM Precipitation Radar (PR) has been instrumental in this pursuit. Recently, TRMM-based analyses of precipitation systems from a regional perspective have been performed. Among these, Berg et al. (2002) found rainfall distributions to differ regionally while the results of Chapter 2 suggest that these regional differences can be described in terms of different mixtures of reasonably similar (i.e. cloud distributions, ensemble heating) "building blocks". In Liu and Zipser (2009), similarity in precipitation systems was also shown for the case of warm-rainfall in various tropical locations. Latter results pointing toward similarity add a level of simplicity to the problem given that one may reconstruct the average state through consideration of a limited number of precipitating cloud ensembles recurring at basin-dependent relative frequencies of occurrences.

One limitation of a TRMM-based analysis is that the temporal evolution of regional precipitation systems cannot be studied on short (i.e. sub-daily) timescales. This limitation was addressed in Chapter 3 by incorporation of the three-hourly resolution CMORPH rainfall product. In Chapter 3, a mechanism for determining the temporal evolution of rainfall at a 2° spatial scale was proposed. The physical process outlined involved the consideration of satellite-derived cold pool kinetic energy (CPKE) and radiosonde-observed (RAOB) convective inhibition (CIN). When CPKE approached the magnitude of CIN, rainfall was shown to increase.

In this chapter, the analysis frameworks of Chapters 2 and 3 are applied to output from a novel multi-scale modeling framework (MMF). An MMF is configured in a manner that entails embedding a two-dimensional cloud-resolving model (CRM) into each large-scale grid box of a host general circulation model (GCM). The idea extends back to the work of Grabowski and Smolarkiewicz (1999) and Grabowski (2001). In the MMF configuration, "curtains" of CRMs simulate sub-GCM grid scale processes formerly accounted for through use of boundary layer, cloud and convection parameterizations. The MMF (occasionally referred to as superparameterization) approach is one suggested way forward (Randall et al. 2003; Arakawa 2004; Arakawa et al. 2011) in terms of modeling cloud processes during the period of time between the sole use of traditional convective parameterization and the sole use of global CRMs for climate simulations, and so far, simulations have yielded much improved representations for many phenomena (e.g. Benedict and Randall 2009; Pritchard and Somerville, 2009a,b; Benedict and Randall 2011 Demott et al. 2011; Pritchard et al. 2011).

The specific tasks undertaken in this study first involve quantifying recurring precipitating cloud ensembles depicted by the CRM "curtains" spanning the tropics and comparing results to the TRMM-derived rainfall clusters of Chapter 2. The second task of a two-fold analysis involves documenting the evolution of the environment on hourly time scales relative to varying-magnitude rainfall cycles and comparing results to the multi-sensor observational depiction developed and discussed in Chapter 3. The evaluation of model-simulated precipitation systems and short timescale rainfall evolution with respect to multi-sensor observations is, of course, an overarching goal of this work. However, in addition to this compare-and-contrast perspective, a particular aim of this study pertains to determining the extent to which a consistent conceptual framework for the evolution of different precipitation states on sub-daily timescales can be developed, utilizing a collaborative approach involving both observations and the model.

4.2 Observational Sources and Model Description

4.2.1 Observational Datasets

Several sources serve as observational benchmarks against which MMF rainfall and background characteristics are evaluated. All are discussed at length in Chapters 2 and 3 of this dissertation. The TRMM 2A25 and CMORPH three-hourly rainfall products serve as the basis for observed rainfall. RAOB-based parameters (saturation fraction, CAPE, CIN), and QuikSCAT CPKE are used for the large-scale environment state depiction with respect to rainfall evolution. Aspects of the analysis entail describing the evolution of parameters on sub-daily timescales. For instance, in order to document the temporal evolution of the environment relative to TRMM rainfall clusters, the differences in local observing times for

each observational platform and TRMM satellite overpass times must be tallied. This concept is extended as needed, since for any geographic location, storing the time differences between one observational platform and another collecting data at slightly lagged times allows for the investigation of short-term (i.e. sub-daily) convection evolution, as proposed in the Introduction.

4.2.2 Superparameterized Community Atmosphere Model (SP-CAM).

Model output from a five-year (September 1999 – August 2004) MMF tropical atmosphere simulation are used in this analysis. This particular MMF is a version of the superparameterized National Center for Atmospheric Research (NCAR) Community Atmosphere Model (CAM Version 3.0, or CAM3; Collins et al. 2006) coupled with a simple mixed-layer ocean model (hereafter referred to as SP-CAM). CAM3 has a horizontal resolution of ~ 2.8°, 30 vertical levels, and a time step of 30 minutes. A two-dimensional version of the System for Atmospheric Modeling (SAM; Khairoutdinov and Randall 2003) CRM is embedded in each grid box of CAM3. The CRM has a 128 km domain (32 columns at 4 km resolution) with periodic boundary conditions, a north-south orientation, and shares the same lowest 28 levels of CAM3. Further details on this particular SP-CAM configuration are provided in Khairoutdinov et al. (2008), while a schematic of the coupling between the host GCM grid and embedded CRM is illustrated in Benedict and Randall (2009).

The coupling of the atmospheric model to the slab-ocean model is described in Benedict and Randall (2011), and is formulated in such a way that SSTs can respond to anomalous surface fluxes, thereby affecting lower-troposphere buoyancy, evaporation and

ultimately, the evolution of convection on a wide range of time and spatial scales. Care is also taken to ensure that the model constrains SST deviations in such a manner that the observed SST climatology over the 5-yr period is still maintained. In effect, the incorporation of a simplistic slab ocean model represents an attempt towards realistically simulating the interaction between sea surface temperatures (SSTs) and the lower atmosphere. This has led to an even more realistic depiction of intraseasonal variability including the Madden-Julian Oscillation (Benedict and Randall 2011) relative to other MMF simulations that use prescribed SST fields.

CAPE, CIN and saturation fraction are all derived from CRM domain-average temperature and water vapor profiles, using the methods described in Chapter 3. The CRM domain-average profiles are equivalent to what would be provided on the GCM scale at the beginning and end of each GCM time step. In Chapter 3, CPKE was defined to be the average of the root mean square surface velocity fluctuations over an approximate 2x2° grid box. This satellite-based parameter is available over ocean only. Formulated similarly to the observed parameter (although at a different spatial scale), CPKE in the MMF, available for all GCM grid boxes, is equal to the CRM domain-average root mean square velocity fluctuation over the lowest model level of the CRM, although the model analysis is not limited to oceanic regions only.

4.3 Two-Part Analysis Methodology

4.3.1 Rainfall Regimes

In Chapter 2, observed rainfall clusters were largely classified and interpreted according to their raining cloud distributions and ensemble heating profiles. Therefore, the

development of a method for delineating MMF precipitation states should include an emphasis on these same characteristics. In this work, the chosen methodology centers on comparing MMF diabatic heating profiles to TRMM cluster heating profiles.

A particularly simple way to do this involves defining a Euclidean distance metric (d) to represent the average discrepancy between any given model heating profile and each of the TRMM cluster profiles. The metric is formulated as a two-dimensional array of (number of TRMM clusters) x (npoints), where npoints is computed as the total number of tropical grid-boxes in the MMF multiplied by the total length (in hours) of the simulation. For each grid-box and simulation hour (ipoint), the rows of d contain distance measures equal to the sum of the absolute value differences between each of the three TRMM cluster $Q_1 - Q_R$ profiles (illustrated in Chapter 2, interpolated to the MMF vertical levels, and often referred to as $Q_{1\text{-}R}$), and the CRM domain-average $Q_{1\text{-}R}$, calculated as

$$d\,(\text{ipoint},\text{icluster}) = \sqrt{\sum_{z=1}^{\text{nlev}} (Q_{1\text{-}R,\,\text{TRMM}}(\text{icluster},z) - Q_{1\text{-}R,\,\text{MMF}}(z))^2} \quad . \tag{4.1}$$

There are conditions that must be met for a CRM heating profile to be classified, all of which allow for greater consistency with the observational method described in Chapter 2. If $Q_{1\text{-}R}$ is 0 for all model levels, the profile is classified as non-raining and is not compared to the TRMM clusters. If all precipitating hydrometeor contents are negligible to the extent that TRMM PR would be incapable of observing the scene or if all rainfall is determined to be of non-convective origin (computation of a radar reflectivity and convective/stratiform partitioning are discussed in greater detail below), the profile is grouped into a "residual" category. The residual category, while occurring fairly often,

consists of such light rain that it contributes little to the total rainfall accumulation in the tropics. For all remaining scenes, the Euclidean distance formulation forces model heating profiles to belong to one of the TRMM observed clusters. MMF clusters now represent the composite average of all profiles belonging to each of the three TRMM cluster centroids. This allows for a straightforward comparison of the observed and MMF clusters. The extent to which model $Q_{1\text{-}R}$ profiles deviate significantly from each of the three observed clusters will clearly be reflected in the final MMF composite heating clusters.

Precipitation top height (PTH) distributions can now be derived for each MMF cluster and compared to the observed ones discussed in Chapter 2. As for determining the distributions, the MMF configuration is ideal given that hydrometeor profiles are available for every grid cell of each embedded CRM. The comparison proceeds by adopting a "model-to-satellite" approach. First, PR attenuation-corrected radar reflectivity profiles are computed given model hydrometeor, water vapor and temperature profiles. Provided with hydrometeor contents and CRM assumed drop size distributions (values originally set in Kharoutdinov and Randall (2003), although later modified (M. Branson and M. Khairoutdinov, personal communication)), PR reflectivities are simulated with relative ease through use of a radar simulator. Each precipitating column of the CRM is then diagnosed to be convective or stratiform based on an algorithm (Steiner et al. 1995) heavily relied upon in current PR product rain-type classifications, whereby convective and stratiform regions are separated according to peaks in radar reflectivity relative to a background average. The convective/stratiform classification is used in the derivation of the MMF PTH distributions. These distributions are derived by storing the maximum altitudes of detectable radar echoes (surpassing a threshold of 17 dBZ, the minimum detectable signal

for TRMM PR) above the surface for all convective-only cells of each CRM domain. Additionally, in order for a cell to be considered in the distribution, it must have a non-zero surface rainfall rate, consistent with the methodology of Chapter 2.

MMF precipitation clusters, objectively determined according to $Q_{1\text{-}R}$ profiles, are compared to TRMM cluster heating and associated raining cloud distributions for the same tropical ocean basins outlined in Chapter 2. RAOB saturation fraction, CAPE, CIN and QuikSCAT CPKE are temporally and spatially co-located with the TRMM clusters, and compared to the equivalent background parameters derived from the model fields and associated with the MMF precipitation clusters.

4.3.2 Sub-Daily Temporal Compositing

The first component of this analysis uses the TRMM satellite as the reference for precipitation system description. Precipitation systems are characterized by TRMM-inferred heating profiles and cloud populations. Simulating TRMM observables using MMF output, developing a method for identifying predominant precipitation states, and comparing model clusters to the observed clusters of Chapter 2 concisely summarizes the first focus. TRMM, however, provides only an instantaneous snapshot of precipitation systems with a relative disparate revisit time for any given location. Thus, a documentation of the rainfall lifecycle of any observed precipitation cluster from this sole-satellite perspective is immediately precluded. This is, however, just one complication. When one considers the combined effects of dissimilar orbital characteristics for TRMM and QuikSCAT along with relatively few radiosonde sites (with sparse temporal sampling), it becomes nearly impossible to gather a meaningful sample of various rainfall regimes. To

partly mitigate the sampling issues that arise with the use of the multi-sensor platform described above, a high temporal and spatial resolution multi-satellite product for rainfall (CMORPH) is used in substitution for TRMM. The loss of TRMM implies that the investigation of rainfall and environment evolution must proceed in a manner independent of precipitation clusters.

This component of the analysis, then, mimics the procedure detailed in Chapter 3. Briefly, this involves compositing saturation fraction, CAPE, CIN and CPKE about local rainfall maxima, defined through consideration of a 6-hr smoothed rainfall rate time series. For both observations and the MMF, then, temporal histories of these parameters relative to varying-magnitude rainfall cycles are constructed. Satellite and RAOB depictions of rainfall and environment evolution on sub-daily timescales are then compared to the MMF equivalent portrayals.

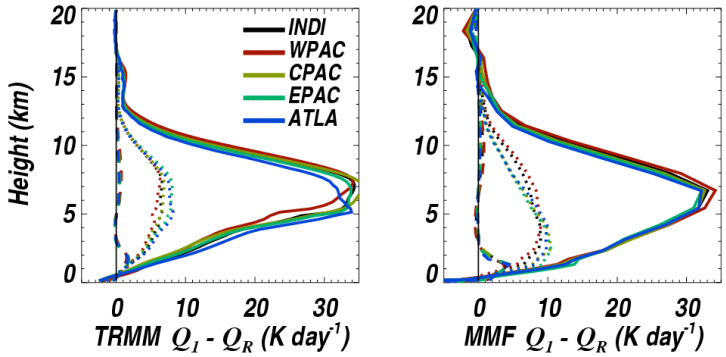

Figure 4.1. TRMM and MMF derived diabatic heating profiles for each rainfall cluster and ocean basin (boundaries shown in Fig. 2.4). The dashed, dotted and solid lines denote the SHAL, UNORG and ORG clusters, respectively.

4.4 Results

4.4.1 Rainfall Clusters and comparison to TRMM

4.4.1.1 Diabatic Heating, Precipitation Top Heights and Rainfall Distributions

The observed and MMF $Q_{1\text{-}R}$ profiles are illustrated in Fig. 4.1. The SHAL, UNORG and ORG terminology is retained in accordance with discussion in Chapter 2. Briefly, these clusters are interpreted as comprising fields of predominantly low-topped (i.e. echo tops below the freezing level), precipitating convective clouds (SHAL); generally unorganized fields of precipitating congestus and deep convective clouds (UNORG); and, organized systems of cumulonimbus clouds and well-developed stratiform components with numerous embedded shallow clouds (ORG). Substantial similarity in the heating profiles exists at most altitudes above the freezing level (~ 5 km). In the MMF, in all clusters and in all ocean basins, significant differences in the

composite heating (up to 5 K day^{-1}) exist below 5 km. This implies an increased production of shallow raining clouds relative to TRMM observations. Additional evidence for this interpretation can be found in Fig. 4.2. In the far-left column, the PR PTH distributions are shown. Bimodal distributions of raining convective clouds are evident, consistent with the images presented in Chapter 2. In the far-right column, despite the fact that distributions of raining clouds are largely unimodal, the RFOs in both the observations and the MMF are in general agreement with each other above the freezing level. The largest divergences in RFO magnitudes occur for the component of the distributions below the freezing level, in which case the MMF indicates significant numbers of raining clouds having PTHs below 5 km. Thus, the characteristics of the heating profiles and the PTH distributions are consistent in the interpretation of a larger population of shallow raining clouds in the MMF.

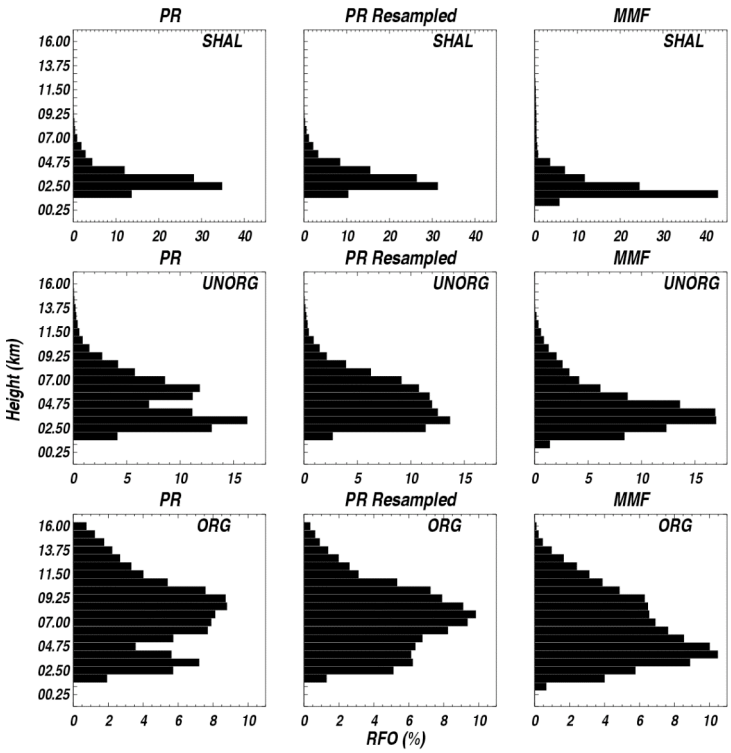

Figure 4.2. TRMM PR and MMF convective precipitation top height (PTH) distributions. For a given height bin, the relative frequencies of occurrence are computed by normalizing each cloud count by the total number of raining convective clouds. PR resampled distributions are described in detail in the text.

Physics of cloud production aside, there are two "mechanical" reasons to expect discrepancies in the PTH distributions. The first requires the consideration of the vertical resolution differences between TRMM PR and the MMF embedded CRM. PR radar reflectivity measurements are available at 0.25 km resolution up to 20 km. The CRM vertical resolution ranges from less than 0.20 km below 1 km to over 2 km at an altitude of 20 km. The rapid change in distribution RFO that exists in the UNORG and ORG clusters is observed near 5 km and occurs over a vertical distance of less than 1.5 km. However, the vertical resolution of the CRM near this altitude is roughly 1.25 km. Therefore, such a sharp structure would not be resolved given the current vertical resolution of the CRM near the freezing level.

To visualize the impact that this coarse resolution has on the PTH distributions, the PR PTH observations are interpolated to the MMF vertical levels and new distributions are computed. These re-sampled distributions are depicted in the middle column of Fig. 4.2. The observed UNORG cluster now exhibits no bimodality, consistent with the MMF, and both yield a peak in PTH occurrence just above 3 km. Bimodality is still somewhat evident in the observed ORG cluster. In fact, some evidence of this is illustrated in the MMF ORG cluster as well. The observed ORG cluster has a peak near 8 km, while the MMF cluster exhibits some "flattening" near this same altitude. The other, lower-altitude peak can be seen just above 3 km, albeit much more pronounced in the MMF.

In addition to considering vertical resolution issues, one needs to consider rainfall detection issues that exist in PR rainfall products. In an analysis of light rainfall from both TRMM PR and CloudSat, Berg et al. (2010) noted that shallow clouds with surface rainfall rates less than 1 – 2 mm hr $^{-1}$ are often missed in PR studies, likely due to instrument sensitivity, algorithm assumptions, and smaller cloud-size-to-PR-footprint ratios. Recall that PTH distributions consist of convective clouds that have both a non-zero surface rainfall rate and a simulated echo top radar reflectivity of at least 17 dBZ. If all raining clouds with surface rainfall rates less than 1 mm hr $^{-1}$ are manually removed from the MMF distribution composites, the peak in PTHs near 3 km decreases in all clusters, and therefore, approaches the magnitudes portrayed in the PR re-sampled distributions. Furthermore, in the MMF ORG cluster, the decrease in the 3 km peak immediately leads to an increase in the prominence of the peak at 8 km (since

distributions are normalized by the total number of clouds), a tendency that is in agreement with observations also.

While this manual removal of shallow raining clouds from the CRM and the effect on the PTH distributions is not published here, given the subjective nature of determining which lightly raining ones should be extracted, the act of doing so leads to better agreement with PR re-sampled PTH distributions. Thus, the two-component process of reconciling PTH distributions (independent of model moist convection representation) requires considering limitations in both the observations (i.e. rainfall detection issues) and the model (i.e. vertical resolution insufficient for resolving distribution structure near the freezing level). Based on this discussion, it cannot be claimed that the MMF produces the correct (additional) accumulation of light rain. It is

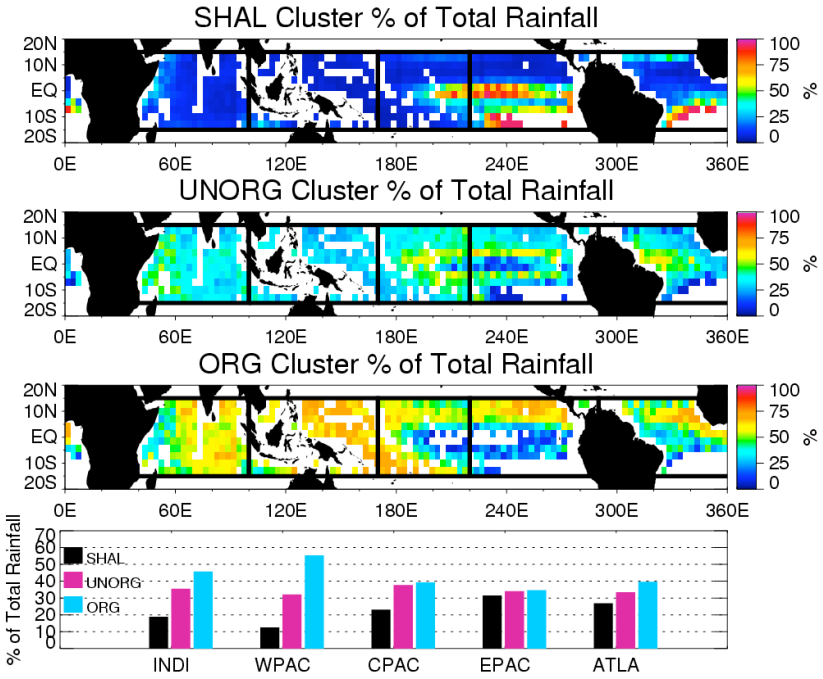

Figure 4.3. As in Fig. 2.4, but for the MMF precipitation clusters.

reasonable to state that PR underestimates the amount of light rain, and taking this into account may explain a notable percentage of the discrepancy in PTH distributions for shallow raining clouds.

The contribution to the average rainfall by each MMF rainfall cluster is shown in Fig. 4.3. Relative to observations (Chapter 2, Fig. 2.4), the deepest clusters (ORG, and to a lesser extent, UNORG) seem to serve as the largest contributors to the mean rainfall state, whereas in the observations, the SHAL cluster serves a greater role in volumetric rainfall accumulation. Prior studies have shown that the MMF produces more rainfall relative to observations in a climate-average sense (Tao et al. 2009). Specifically, it may not solely be the result of increased light rainfall which the MMF shows relative to TRMM, as discussed above, but may be reflective of an increase in deep precipitation regimes. Particularly noticeable is the enhanced contribution by the organized deep convection clusters in the west Pacific warm pool. Away from the warm pool, a number of regions exhibit agreement between TRMM and the MMF. For instance, the detailed, finger-structured extension (5-10°S latitude, 220-280°E longitude) of increased rainfall contribution by the UNORG and ORG clusters is depicted by the observations and the MMF in a remarkably consistent manner.

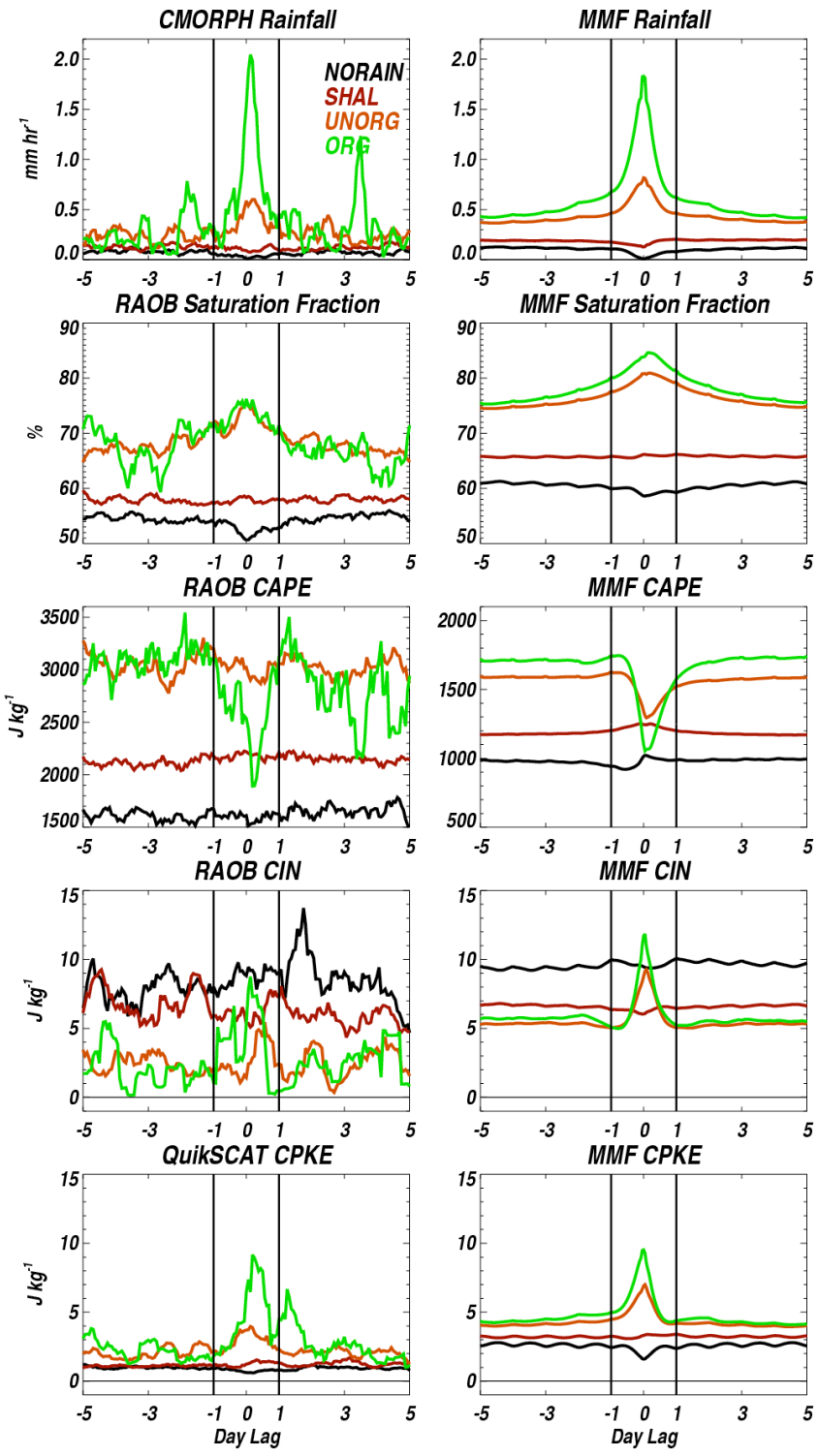

Figure 4.4. Temporal evolution of background parameters as a function of precipitation cluster observed at Day-0. In each panel, vertical lines are drawn for visual reference only.

4.4.1.2 Evolution of the Environment as a Function of Rainfall Cluster

The evolutions of rainfall and background parameters for a ±5 day period with respect to rainfall clusters are shown in Fig. 4.4. Before discussing detailed evolution, note that the absolute magnitude of some parameters relative to the same cluster varies when comparing the observations to the MMF (e.g. saturation fraction, CAPE). The MMF results are for all oceanic locations, while the observed results are for RAOB locations only (Fig. 3.1). Therefore, differing mean cluster background states are expected, given that equal sampling of all spatial locations is not achieved. From this point on, the focus is on the variation of parameters with respect to their background mean or a baseline representative of spatial locations sampled. From this perspective, much commonality is shared in cluster evolutions for both the observations and model.

Beginning with rainfall, significant differences exist over a 2-day period for each rainfall cluster in both the model and observations. For the ORG clusters, the rainfall tendency exhibits a strong resemblance to that of organized convection associated with 2-day waves (Haertel and Kiladis 2004), consistent with the interpretation that this cluster represents organized convective systems. Despite the large differences in rainfall between the UNORG and ORG clusters, similar evolutions of saturation fraction exist. The peak in saturation fraction occurs near the rainfall maximum in the observations, and 3-6 hours after the maximum in the MMF. Higher saturation fractions are both a cause (i.e. a more moist atmosphere prevents the deleterious effects of dry air entrainment on cloud growth) and effect (i.e. deeper clouds penetrating the atmosphere detrain moisture at various levels) of increased rainfall. For the ORG cluster, a significant decrease in CAPE on the order of 1000 J kg $^{-1}$ occurs over the day prior to maximum rainfall, with a

quick recovery taking place over the next 1 – 2 days. This evolution is consistent in the MMF, and is likely the result of cooling in the lower troposphere due to evaporation of rainfall and cold pool activity, along with subsidence warming in the environment

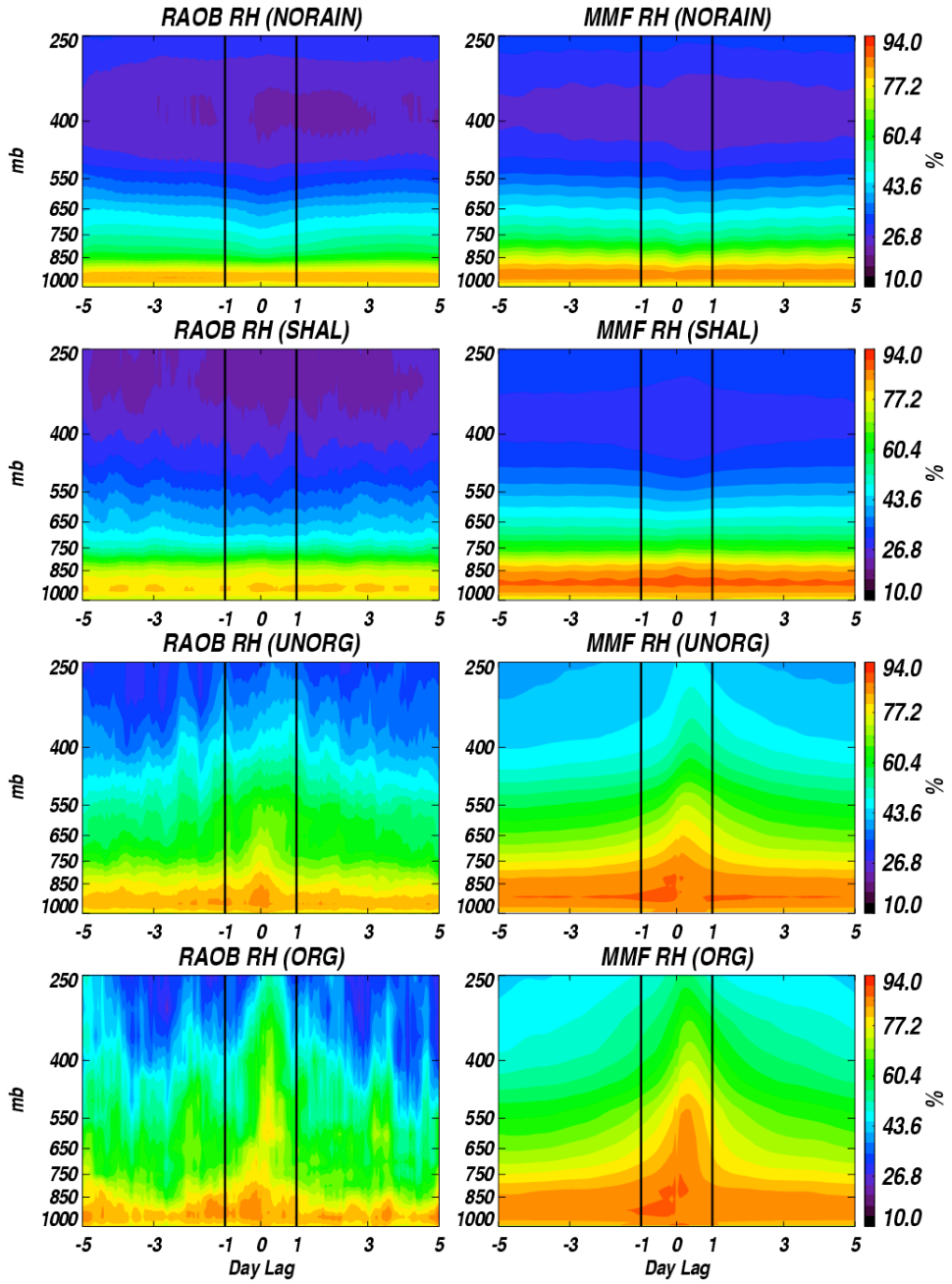

Figure 4.5. Temporal evolution of relative humidity for non-raining scenes and each TRMM and MMF precipitation cluster.

surrounding deep convection. Cold pools associated with widespread convection increase both CIN (again, due to cooling of the lower troposphere) and CPKE (due to kinetic energy generation by convective and mesoscale downdrafts, possibly strengthened by rainfall evaporation). These parameters are expected to increase with rainfall, which is indeed observed to occur in association with the UNORG and ORG clusters. In the MMF, the variations are in phase; in the observations, the peak in CIN appears to be slightly lagged roughly 6 hours after the rainfall maximum.

The relative humidity variations, depicted from a column-integrated point of view (saturation fraction) in Fig. 4.4, can also be investigated from a height-dependent perspective. The variations in relative humidity are illustrated in Fig. 4.5 for the non-precipitating scenes (NORAIN) and three rainfall clusters. The differences in saturation fraction from the SHAL to UNORG and ORG clusters is largely the result of significant relative humidity differences at altitudes above 850 mb (60% versus 25% near 550 mb when comparing the ORG to SHAL clusters, for instance), with less significant differences in lower-troposphere relative humidity (differences on the order of 5-10% for the same clusters). This is consistent with the conclusions of Brown and Zhang (1997) and many others, for instance, noting that variations in mid-tropospheric humidity play a large role in the distribution of cloud tops.

4.4.1.3 RAINFALL CLUSTER PROBABILITIES

The atmospheric environments at a 0-day lag in the composites of Fig. 4.4 represent conditions taking place at the time a particular cluster is observed. Rainfall at any given time is the result of its ambient environment in addition to the characteristics of

the environment evolving over a period of hours prior to the rainfall observation. Therefore, one cannot expect the occurrence of one cluster versus another is statically related to the current state of the atmosphere. Nonetheless, what can be gleaned from Fig. 4.4, however, are strong relations between the cluster, saturation fraction and CPKE. Equally clear from Fig. 4.4 is that non-raining scenes and ORG clusters have similar CAPE and CIN at day-0. As discussed, in the presence of heavy rainfall, CAPE substantially decreases and CIN increases. The changes in these parameters are significant to the extent that the magnitudes approach those characteristic of suppressed, non-raining conditions, thereby limiting their utility in distinguishing one cluster from another from the perspective of background conditions.

Saturation fraction and CPKE are then considered important parameters delineating one cluster from another. The probabilities of the non-raining scenes and rainfall clusters are quantified in Fig. 4.6. Minimal CPKE and saturation fractions are associated with non-raining scenes, while the ORG clusters lie in the state space associated with higher saturation fractions and CPKE. Interestingly, there is a noticeable slope in the probabilities of cluster occurrences, such that the deeper clusters are found in locations with higher saturation fractions and CPKE, but in the event that saturation fractions are lower, CPKE can compensate in such a way as to increase the occurrence probability of a particular cluster. The relations are quite tight in the MMF, with more variability depicted in the observations column. This is anticipated given the presence of retrieval noise and error associated with QuikSCAT surface wind retrievals. Fortunately, this is not a limitation in the model analysis.

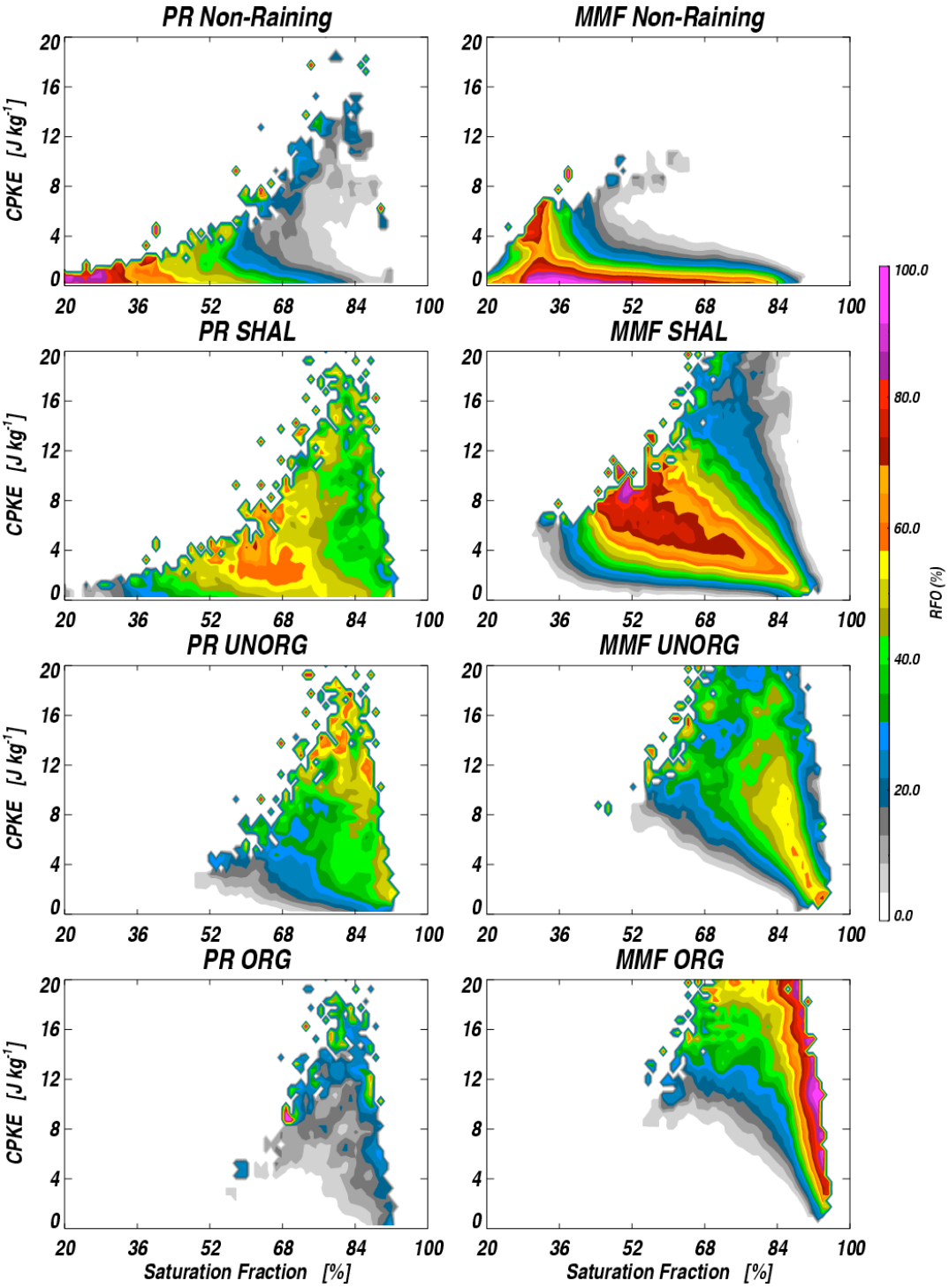

Figure 4.6. Occurrence frequency of non-raining scenes and precipitation clusters as a function of saturation fraction and CPKE.

There is a physical explanation offered for these slopes in cluster probabilities. Consider for the moment that there are larger, more coherent cloud structures or larger areas of upward mass flux associated with the leading edges of stronger cold pools. Therefore, as grid-average CPKE increases, indicative of additional or stronger cold pool activity, the spatial-extent of upward mass flux (related to the horizontal extent of the cloud bases) would increase in size. The effects of dry air entrainment are less severe as cloud parcels increase in size. Therefore, in a drier atmosphere, if parcels, on average, could be made larger, as could occur in the case of increased CPKE, then they could be less resistant to the negative effects of dry-air entrainment associated with lower saturation fraction environments, and thus, the growth of deep clouds commences. A high-resolution (100 m grid-size) modeling study by Khairoutdinov and Randall (2006) provided evidence of such a physical relation, and in this study, a much coarser observational and modeling framework may even be reflecting this behavior.

4.4.1.4 Synthesis of TRMM and MMF Rainfall Cluster Results

As discussed in section 4.3.2, there are limitations in deriving lagged temporal evolutions using a co-located multi-satellite and RAOB database that incorporates TRMM. The compilation of composites relying on platforms with varying temporal and spatial sampling characteristics leads to noisy results, clearly depicted in the temporal evolution panels of the observations column of Fig. 4.4. Therefore, it becomes difficult to establish with certainty when particular variables maximize with respect to rainfall in observations versus the MMF, thus complicating an attempt to establish differences in time lags that may be on the order of a couple hours. Nonetheless, specific comments

about the clusters can be made through use of both the model and observations, thus warranting a useful summary of general results for the first part of this tropical rainfall analysis. For the SHAL cluster and non-raining scenes, little variation in saturation fraction, CAPE, CIN and CPKE occur over the multi-day period. As the clusters becomes progressively deeper, both the observations and MMF depict an evolution of rainfall that is accompanied by significant decreases in CAPE, and increases in saturation fraction, CIN and CPKE that are roughly in phase with rainfall. The ORG clusters contribute roughly 30-40% to the accumulated rainfall in the tropics, as shown in Figs. 2.4 (TRMM) and 4.3 (MMF). Associated with these clusters is a 40-50% decrease in CAPE, occurring over an approximate 12-hour period. One interpretation consistent with these results is that a substantial proportion of rainfall occurs in association with non-equilibrium convection, consistent with the results of Chapter 3. Rainfall such as this would likely not be represented well in many conventional convective parameterizations where assumed decreases in CAPE in the presence of deep convection are small compared to the increase in CAPE that would be realized if convection were artificially suppressed and large scale advection and surface fluxes were acting alone. Despite the fact that there is an overproduction of the heaviest rainfall, particularly in the west Pacific warm pool, the MMF does quite well in simulating this non-equilibrium convection regime relative to TRMM and RAOB depictions, both in terms of significant contributions to tropical rainfall accumulation and CAPE tendencies.

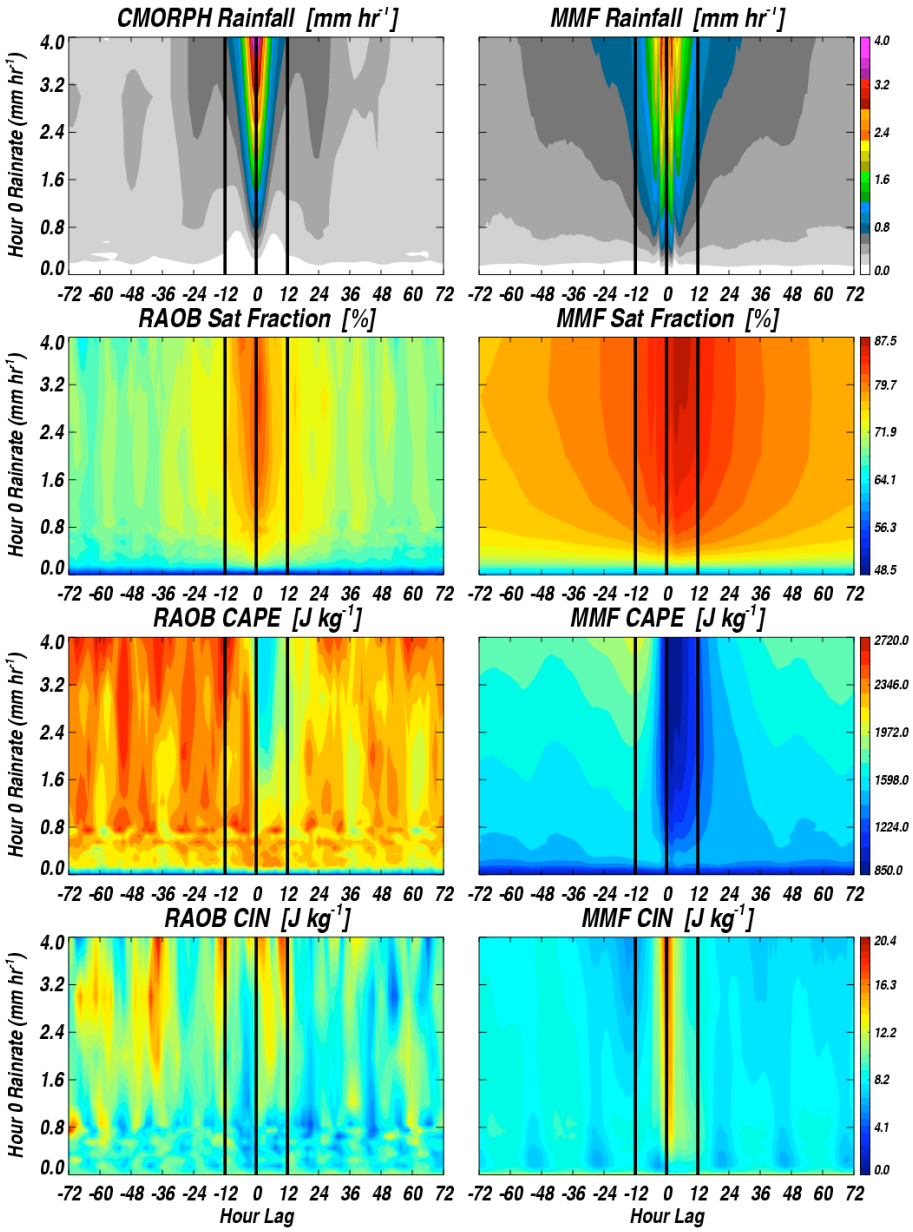

Figure 4.7. Composite temporal evolution of rainfall and background parameters as a function of local rainfall maximum. Vertical lines at ± 12 hrs are shown for visual reference only.

4.4.2 Investigation of Rainfall and Environment Evolution on Sub-Daily Timescales

The two-dimensional temporal composites of rainfall, saturation fraction, CAPE, CIN and CPKE with respect to varying amplitude rainfall cycles are illustrated in Figs. 4.7 and 4.8. The results are partly anticipated given the analysis of section 4.4.1. These

include peaks in saturation fraction at the time of maximum rainfall in the observations (although 3-6 hours later in the MMF), a maximum of CPKE in phase with the peak in rainfall rate, and a rapid consumption of CAPE associated with more intense rainfall cycles. A glaring difference hinted at, but not portrayed as clearly in the prior analysis, pertains to the rainfall and CIN variations depicted in Fig. 4.8. For all precipitation cycles in the MMF composite, rainfall remains elevated over a period of time much longer than that depicted by CMORPH. Furthermore, in the MMF, CIN is in phase with the maximum rainfall axis for the higher amplitude rainfall cycles, while in the RAOB composites, it peaks 6 or more hours after rainfall maxima, particularly evident for cycles with peak amplitude less than 3 mm hr^{-1}. The in-phase relationship between CPKE, CIN and rainfall and possible implications are discussed in greater detail below.

An attempt was made in Chapter 3 to understand the increase in rainfall through consideration of CIN and CPKE. Increases in CIN provide a negative feedback on rainfall, whereas increases in CPKE provide a positive feedback. Both parameters are related to cold pool activity, as discussed, but represent opposite, competing influences on the short timescale rainfall tendency. In this view, CAPE and saturation fraction were viewed as necessary for increased rainfall, but not as parameters strictly dictating the period of time over which rainfall remains elevated. It was argued that rainfall remains increased relative to the background during the time that CIN and CPKE are of comparable magnitude, such that when the ratio of CIN / CPKE approaches unity (i.e. ratio decreases with time), rainfall can increase, provided a reservoir of CAPE and moisture exists. Associating a specific ratio magnitude to the rainfall tendency was not a

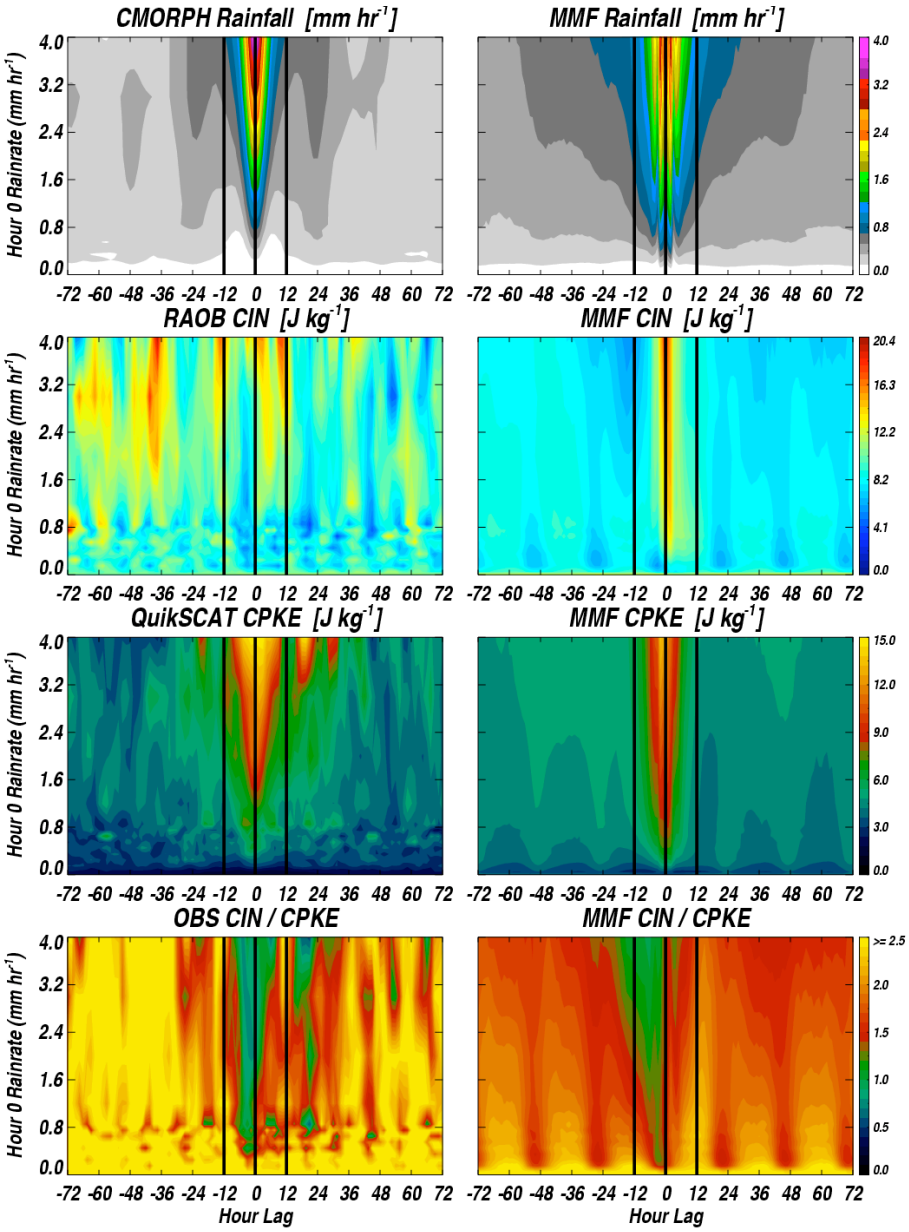

Figure 4.8. As in Fig. 4.7, but for CIN, CPKE and the ratio of CIN to CPKE.

goal of Chapter 3, for reasons discussed in section 3.5. Nonetheless, it was shown that increased rainfall was associated with decreased CIN / CPKE magnitudes.

This concept is applied now in the investigation of MMF rainfall time-tendencies. The ratio of CIN / CPKE is reproduced for the observations in the bottom left panel of Fig. 4.8, and for the MMF in the bottom right panel. Immediately evident are decreased

ratios coincident with increasing rainfall in the MMF, along with a minimum in CIN / CPKE before the rainfall maximum, as seen in the observations. A notable difference is the "reddening" of the image, indicating that CIN and CPKE are perhaps more closely coupled than suggested in observations. This divergence from observations, however, is anticipated given that MMF CIN and CPKE are both in phase with rainfall, as discussed.

Regarding the phasing between these parameters, consider first the CIN relationship with rainfall. There are two possible reasons why it would be maximized during the time of peak rainfall in the current MMF design. Recall that for the deeper convection clusters (UNORG and ORG), similar raining cloud distributions exist for the deepest convective clouds in conjunction with comparable or greater diabatic heating relative to observations. Associated with these intense convective cells are significant columns of upward vertical mass flux. In accordance with mass continuity, compensating mass flux occurs in the columns surrounding the convection. However, in the CRM, given that there are only 32 columns comprising the 128 km periodic domain, compensating motion can only take place in a limited number of columns. In the case of 3D convection (i.e. observations), the area over which subsidence takes place relative to convection is much larger. It is possible, then, that compensating subsidence is much stronger in the current MMF configuration for a given domain average rainfall rate, and the warming associated with the subsidence may contribute toward increasing CIN much more quickly than would otherwise be the case, thus leading to a tighter coupling between rainfall and CIN. The other possibility relates to an exaggerated cooling effect in the lowest levels of the model due to cold pool activity. This also amounts to a spatial scaling argument, in that the limited, periodic domain of the CRM doesn't permit

propagation of cold pools beyond the extent of the grid box, and thus the cooling effects of cold pools are proportioned among the limited number of cells existing in the domain. This also could result in CIN being in phase with rainfall. The same argument pertaining to the inability for cold pools to exit the restricted 2D domain of the CRM may lead to an exaggeration of CPKE for all rainfall rates as well. This hypothesis would be consistent with the strong spike in CPKE at less intense rainfall rates in Fig. 4.8, relative to that which is depicted in the observations panel.

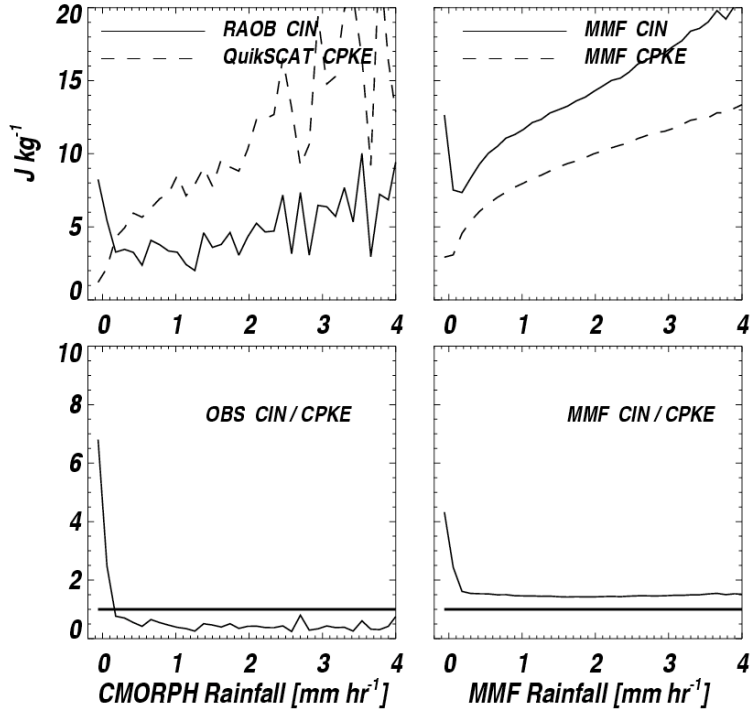

Figure 4.9. Observed and MMF average instantaneous relations between CIN, CPKE and rainfall.

CIN and CPKE are shown as a function of rainfall rate in Fig. 4.9. The rapid increase of CIN with respect to rainfall rate and elevated CPKE (particularly for low rainfall rates) in the MMF is illustrated in the top right panel, reflective of the tight coupling between rainfall, CPKE and CIN. Visually averaging out the noise (evident at

higher rainfall rates) in the QuikSCAT CPKE curve leads to a functional relationship between rainfall and CPKE that is similar to that which is portrayed in the MMF panel. The weaker coupling between CIN and rainfall is gathered from the observational (top left panel) perspective. The conceptual summary between the observations and MMF is the same, however – that is, non-raining scenes are characterized by CIN overwhelming CPKE, while significant rainfall occurs in conditions where CPKE approaches the magnitude of CIN.

Regardless of the mechanism that may contribute most significantly to a tightly coupled relationship between rainfall, CIN and CPKE, the smaller MMF CIN / CPKE ratio, evident throughout the entire bottom right panel of Fig. 4.8, implies that rainfall should be more widespread than in the observations. In other words, rainfall may both develop more easily in the MMF, and decay at a slower rate. This is indeed the case in the MMF rainfall panel of Fig. 4.8, and consistent with prior results discussed above noting that the MMF generally produces more rainfall than satellite observations show.

4.5 Conclusions

TRMM observations of tropical precipitation and raining cloud distributions are compared to collections of clouds derived from two-dimensional, periodic CRMs embedded in the large-scale grid boxes of the CAM. The MMF simulation used in this study is unique in that the atmospheric model is coupled to a simple mixed-layer ocean model permitting interaction between SSTs and lower-atmosphere energy fluxes. A more realistic treatment of the coupling between the ocean surface and lower atmosphere, and the use of a CRM in substitution of traditional convective and cloud parameterizations,

provides for a simulation of tropical convection superior to that of most parameterized GCMs, thus motivating the development of a new test-bed for comparing state-of-the-art GCM precipitating convection to multi-sensor observations of rainfall.

It is found that observed precipitation clusters, defined and interpreted according to TRMM PR distributions of echo-top heights and diabatic heating over a spatial scale similar to that of the GCM, are largely reproduced in the current SP-CAM after accounting for vertical resolution effects on cloud distribution derivations, and limitations in the PR product pertaining to capturing the correct distribution of shallow, lightly raining clouds. The three precipitation clusters that emerge are representative of shallow precipitation regimes (ensemble of clouds whose tops peak below the freezing level), unorganized deep convection regimes (deep clouds exist in the distributions, but less extensive upper level heating may indicate a lack of organization associated with the regime) and organized regimes (numerous deep and shallow clouds, and extensive heating above the freezing level). The overall contribution to the mean state of rainfall in the MMF by each cluster includes increased (decreased) volumetric accumulation by organized convective (shallow) regimes, relative to the PR depiction. These regimes may be responsible for the high-biased mean rainfall state that exists in the MMF. Surprisingly, despite the 4 km horizontal resolution of the CRM, within the shallow regime itself, raining cloud distributions and rainfall rates are comparable to PR results.

Bimodality in raining cloud distributions is a characteristic result of the two deepest TRMM clusters. While the MMF representation of the deepest regime hints at the existence of a bimodal distribution of raining clouds, despite the decreased amplitude of the peaks relative to TRMM, the cloud distributions are largely unimodal. It is argued that this

representation may be the result of the coarse CRM vertical resolution. The ability to simulate these distributions would require increased resolution, particularly near the freezing level.

Precipitation clusters are reasonably well separated in a state space defined by saturation fraction and CPKE. A deeper rainfall cluster can occur at a lower saturation fraction given sufficient cold pool activity. Physically, it is suggested that this occurs because larger areas of rising motion constituting ensembles of clouds occur in association with increased cold pool activity. This may be equated to an increase in size of convective plumes; thus, clouds may be more resistant to the detrimental effects of dry air entrainment. Even in the coarse-resolution CRM used here, similar behavior seems to be occurring.

A significant percentage of observed rainfall accumulation (roughly 30-40%) takes place during time intervals characterized by substantial decreases in CAPE. The MMF simulates this characteristic of non-equilibrium convection behavior quite well, likely in contrast to GCMs utilizing traditional convective parameterizations that assume quasi-equilibrium behavior between consumption of CAPE by convection and increases due to all non-convective processes.

In Chapter 3, rapid increases in rainfall were posited to occur when the kinetic energy associated with cold pools (CPKE) approached the magnitude of inhibition energy (CIN). In that component of this dissertation, rainfall, CPKE and CIN were all derived through use of satellites and radiosondes. The same conceptual framework was used to understand the pick-up of tropical rainfall that occurs in the MMF. In observations, CIN peaked after the period of maximum rainfall and was out of phase with CPKE (which peaks during rainfall). The lag allows for CIN to overwhelm CPKE in a more dramatic

manner, serving to cap the time period during which rainfall remains elevated. In the MMF, rainfall, CPKE and CIN are all tightly coupled and in phase, hypothesized to be the result of the two-dimensionality and limited domain of the currently embedded CRM. The enhanced coupling of CPKE and CIN, even in light rainfall, means that heavier rainfall may be more quick to develop and slower to end than would otherwise be the case in a larger-domain CRM or three-dimensional CRM configuration. It was proposed that this contributes to a lengthening of the time scale during which rainfall remains elevated, and may assist in explaining why heavier rainfall seems to last longer in the MMF relative to the satellite depiction, and may play some role in why the mean rainfall state in the MMF is biased high relative to observations.

CHAPTER 5

RAINING CLOUD POPULATIONS AND THEIR EVOLUTION DURING MADDEN-JULIAN OSCILLATION CONVECTIVE INITIATION IN THE WEST INDIAN OCEAN

5.1 Introduction

The initial discovery and findings of Madden and Julian (1971; 1972) have paved the way for almost four decades of research into the characteristics of the slow, eastward-propagating tropical disturbance commonly referred to as the Madden-Julian Oscillation (MJO). The MJO, while recognized as the foremost low-frequency mode of tropical intraseasonal variability influencing a wide range of global climate phenomena (e.g. Lau et al. 1989; Webster et al. 1998; Maloney and Hartmann 2000; Lawrence and Webster 2001; Maloney and Hartmann 2001; Zhang 2005), continues to be poorly simulated in contemporary global climate models (Lin et al. 2006; Kim et al. 2009). Thus, in tailoring a coherent picture of the MJO from deep convective initiation in the western Indian Ocean to termination near the dateline, continued extensive studies pertaining to the governing physics of the MJO (e.g. Majda and Stechmann 2009; Majda and Stechmann 2011), depiction in observations (e.g. Masunaga et al. 2006; Benedict and Randall 2007; Masunaga 2007; Tromeur and Rossow 2010) and representation in advanced climate

models (Benedict and Randall 2009; Thayer-Calder and Randall 2009; Benedict and Randall 2011) are warranted.

General deficiencies in MJO simulation aside, specific studies have shown that many models demonstrate the least amount of skill in forecasting the MJO during its initiation in the western Indian Ocean (Kim et al. 2009). This implies certain physical processes may be more relevant during the development of deep convection in the initial stages of the MJO than during convective development over more eastern longitudes in association with an already developed, propagating MJO event. While fundamentally related, two general components of the MJO problem thus arise: one aspect pertaining to propagation of large-scale, well defined convective envelopes, and another related to the first appearance of deep convection on MJO spatial scales.

The latter component of this problem is now attracting significant interest, corroborated by a recent international proposal (CINDY2011/DYNAMO[1]) to observe detailed cloud populations and environmental evolution during the initiation stages of an MJO event in the Indian Ocean. This expansive field campaign will consist of numerous in situ observations and high-resolution modeling studies to gain an increased understanding of the nature of convection at this stage in the MJO lifecycle. The Indian Ocean has long suffered from a lack of observations, hindering the development of a conceptual picture of convection and relation to the MJO in this remote ocean basin; hence, the motivation for a comprehensive campaign such as CINDY2011/DYNAMO.

[1] Cooperative Indian Ocean Experiment on Intraseasonal Variability in the Year 2011 (CINDY2011); Dynamics of the Madden-Julian Oscillation (DYNAMO) is the U.S. counterpart.

The characteristics of convection up to and through the initiation of the MJO will be intimately tied to the environment in which cloud development is taking place. The time tendency of environmental parameters favoring the development of deeper convection (increased moisture, for instance) can be influenced by processes deemed either local to the environment (e.g. evaporation) or external to the basin (e.g. wind shear or moisture transport in association with traveling waves originating outside of the ocean basin). Examples of various internal and external processes can be found in Jones and Weare (1996), Blade and Hartmann (1993), Stephens et al. (2004), Matthews (2008), Ray et al. (2009), and Ray et al. (2011). There is no a priori reason to expect that local processes have a monopoly on MJO convection initiation relative to external ones (or vice versa). Given the numerous initiation mechanisms explored in the literature, both internal and external factors are expected to play a role. Irrespective of the convective initiation process, the desire to document cloud populations and their evolution at this stage of the MJO remains.

The current lack of quantified cloud populations at this stage motivates the crux of this work, which aims to determine specific raining cloud populations and their evolution during Indian Ocean MJO initiation. The depiction that emerges is a product of a combined analysis of TRMM PR observations and output from a state-of-the-art climate model (SP-CAM coupled with a slab-ocean model, described in Benedict and Randall (2011); hereafter, often referred to as the MMF) that has been shown to simulate MJO variability with a realism typically unachieved from a climate model perspective. This cooperative effort will consist of detailing the evolution (during MJO initiation) of recently derived, often-occurring TRMM PR and MMF precipitation clusters (Chapters 2

and 4 of this dissertation), largely interpreted according to their constituent raining cloud populations. In this way, cloud population evolutions are implicitly described. The evolution of environmental parameters will be discussed as well, in order to 1) understand the background conditions fostering particular cluster occurrences, and 2) to document the prominent moistening processes responsible for the long-term increase in column water vapor prior to final convective initiation in the Indian Ocean.

Each precipitation cluster is robustly described by a unique heating profile that is observed to be similar in the tropics regardless of where the cluster is observed (Chapters 2 and 4 of this dissertation); therefore, the relative frequency of occurrence (RFO) of each cluster during MJO initiation strongly relates to the diabatic heating as a function of height, providing more useful information beyond that which would be available from a rainfall-only analysis. The analysis, while geared toward the MJO initiation problem, will also consist of quantifying raining cloud populations for locations experiencing growth of convection due to an already eastward-propagating MJO-event convective envelope. This additional analysis is performed so that the evolution of convection within the context of MJO initiation can be easily contrasted with the evolution that occurs in association with an already present large-scale convection anomaly (i.e. the propagation problem).

5.2 Data and Methodology

The CMORPH product and measurements from TRMM PR serve as the basis for rainfall and precipitation cluster characterization. Model precipitation clusters and all background parameters are derived from fields produced by an MMF simulation discussed

in Chapter 4. CMORPH, TRMM PR and the particular MMF configuration employed are all discussed at length in Chapters 2 and 4.

The environment in which TRMM precipitation clusters are evolving is entirely characterized by output from the Modern-Era Retrospective Analysis for Research and Applications (MERRA; Rienecker et al. 2011), available online through the NASA Goddard Earth Sciences Data and Information Services Center (GES DISC). The grid resolution for MERRA consists of a 0.50° latitude x 0.67° longitude horizontal mesh with 72 vertical levels of varying pressure thicknesses extending from the surface to 0.01 mb. Like other reanalysis products, the MERRA project involves assimilating multi-satellite retrievals of water and energy parameters, thus retaining a strong connection to Earth-atmosphere satellite observations that now comprise time series extending beyond 30 years. However, a unique aspect of this reanalysis project involves quantifying (and making available as an output parameter) the effect observations have on the temporal evolution of the atmosphere. This time tendency term is referred to as an "analysis increment" and because it is always quantified and provided, all budget equations for water and energy are exactly satisfied. The magnitude of the analysis increment does, to a large extent, relate to deficiencies in the physics of the model. Since the model state is forced to follow (at least reasonably so) the observed state in time, the analysis increment magnitude indicates the extent to which the physical terms of the prognostic equations are not providing the forcing necessary to evolve the state in a manner consistent with the observations. To this end, the analysis increment term can be used to quantify particular model shortcomings. Further details on MERRA alongside general mean-state depictions can be found in Rienecker et al. (2008), Bosilovich et al. (2011) and Rienecker et al. (2011).

In both the observations (CMORPH) and MMF, MJO events are isolated by spectrally analyzing rainfall fields (averaged to ~2.5° spatial and 1-day temporal resolution). First, for each location, the first three harmonics of the annual cycle (periods of a quarter, one-half and one year) are removed from the rainfall time series (Jan 2003 – Jan 2008 for observations; Sept 1999 – Sept 2004 for the MMF). The mean and linear components in time are then subtracted from each sequence, and the beginning and ends of each series are tapered to zero. Two-dimensional Fast Fourier Transform (FFT) is then applied to each latitudinal band (an array of time versus longitude) from 15°S – 15°N to obtain a frequency-wavenumber representation of the domain. MJO filtering proceeds by retaining frequencies and wavenumbers bounded by a rectangular domain comprising periods of 30 – 96 days and 1 – 5 in zonal wavenumber, as in Wheeler and Kiladis (1999). The filtered field is finally transformed back to a space defined by time and longitude.

Following a methodology similar to that of Masunaga (2007), all latitudinal bands are re-assembled to construct a three-dimensional (time, latitude and longitude) portrayal of MJO filtered rainfall anomalies. Propagating rainfall anomalies now have both a meridional and latitudinal structure. In this manner, convective anomalies are traced in time and all future composites of any variable are derived with respect to the latitude and longitude location of the MJO anomaly as opposed to indiscriminately computing an average over all latitudes from 15°S – 15°N (and essentially, neglecting the latitudinal location of the maximum in MJO filtered rainfall). The decision to track MJO events in this manner seems particularly useful for the initiation problem. Whereas anomalies in convection may extend over 10-20° in latitudinal extent as a well developed MJO event propagates eastward, convective development at MJO initiation in the West Indian Ocean

may only occur over limited latitudinal spatial extents. Therefore, it seems most reasonable to composite parameters with respect to those same limited locations, as opposed to computing a 15°S – 15°N meridionally-averaged parameter and investigating that temporal composite during MJO initiation.

Regarding MJO event diagnosis, a rectangular domain for MJO initiation is now defined for the West Indian Ocean. Meridionally, it extends from 15°S – 15°N latitude and zonally, from 40° – 90° E longitude. Considering this domain only, the latitude and longitude of MJO initiation is defined according to the innermost location of the first appearance of a spatial envelope consisting of filtered rainfall anomalies exceeding a threshold of 1.5σ. The area of anomalies surpassing this threshold is often small during initiation. As time proceeds and an event propagates eastward, the spatial extent of anomalies exceeding this magnitude often increases. Event termination occurs when any rainfall anomaly fails to exceed the 1.5σ threshold; the time, latitude and longitude are then stored to mark the termination location. The same technique is applied to the MMF for MJO event identification.

A schematic of this identification procedure is shown in Fig. 5.1. As discussed, the actual methodology isolates events in a latitude/longitude domain. Here, to facilitate visualization, identification is shown in a meridional/time domain. In the bottom left Hovmöller diagram, MJO events are enclosed by black oval-shaped contours; event initiations (terminations) are denoted by the western-most (eastern-most) locations of the contours. As expected, most events appear to initiate near 60° E longitude. An event is then projected onto a two-dimensional panel as illustrated in the figure (where, again, it is understood that the initiation, midpoint and termination represent latitude locations in

addition to longitude/time). All MJO events having a longitudinal separation between

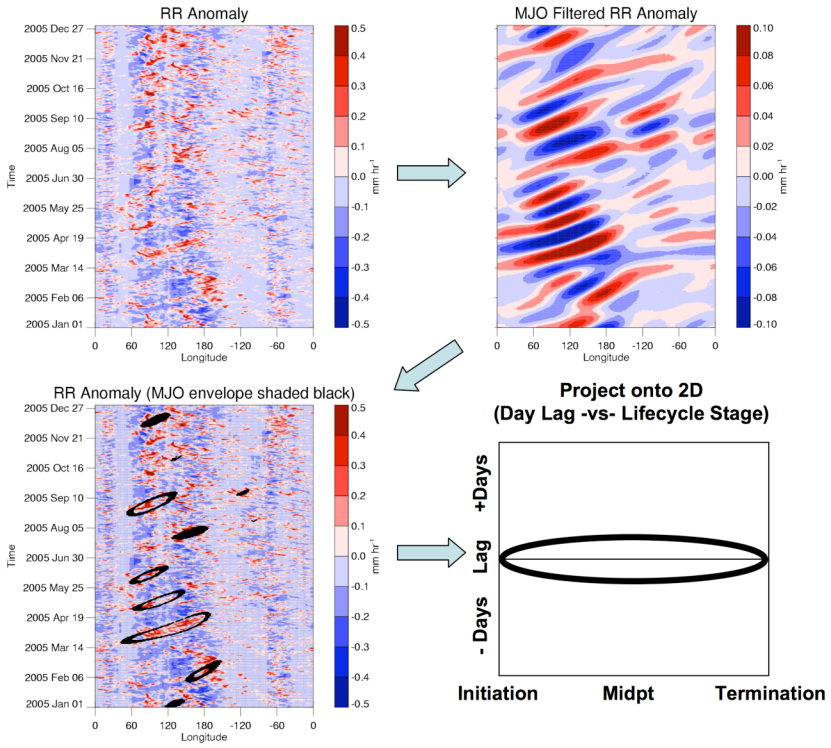

Figure 5.1. A schematic of MJO event identification and compositing methodology. In this example, a composite event, denoted by the oval in the bottom right panel, would represent an average of all events outlined (and meeting certain criteria, as detailed in the text) in the bottom left panel.

initiation and termination exceeding 20° are averaged to form a composite depiction of the MJO cycle (amounting to a total of 23 and 17 events in the observations and MMF, respectively). Elaborating on the bottom right panel in Fig. 5.1, the x-axis represents the life-cycle stage of the composite event as a whole. For each stage, pentad-smoothed composites of unfiltered rainfall, precipitation clusters (SHAL, UNORG and ORG), integrated water vapor (TPW), integrated moisture convergence (TPWTRANS), evaporation minus precipitation (E-P) and lower-troposphere temperature lapse rates are

constructed for a ± 20-day period temporally-lagged with respect to the centered (in time) location of a propagating, MJO-filtered rainfall anomaly exceeding 1.5σ.

5.3 Composite Results

5.3.1 Rainfall and Raining Cloud Populations

Composites of rainfall are shown in Fig. 5.2. The top three panels portray three different observations-based rainfall composites. CMORPH rainfall is considered the primary benchmark from the observational perspective. This characterization stems from the sole reliance on multi-satellite observations. Moreover, because of how constituent satellite measurements are synthesized in CMORPH, a three-hourly temporal resolution is achieved. Therefore, observed composites of CMORPH rainfall are expected to be most representative of the mean rainfall state in this portrayal, given that each MJO event is consistently and equally sampled.

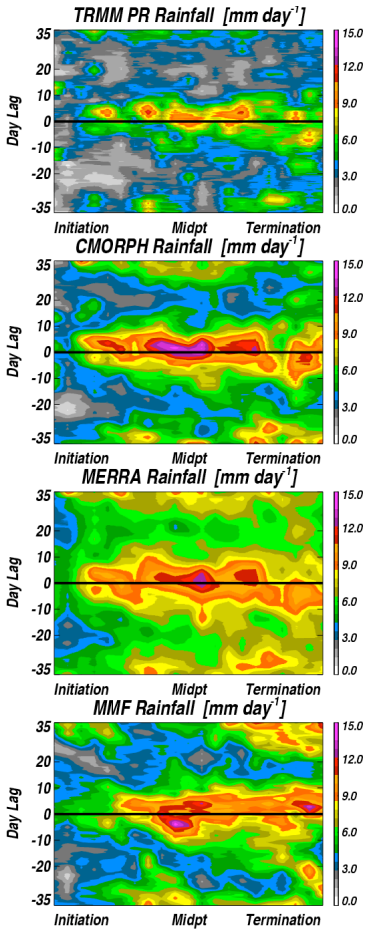

Figure 5.2. Temporal evolution of rainfall as a function of the MJO lifecycle stage.

TRMM PR rainfall is shown in the top panel of Fig. 5.2. Owing to the non-sun-synchronous orbit of TRMM, any given location experiences a sparse revisit time. To this

end, the mean state of TRMM PR rainfall for each day lag and lifecycle stage of the MJO could appear drastically different from the view provided by CMORPH. However, a visual inspection of the TRMM PR and CMORPH rainfall panels highlights at least reasonable pattern agreement between the two depictions (e.g. less rainfall for all time lags during the initiation stage, increasing rainfall for all stages at -15 days, etc.). Hence, while sampling issues play some role, it is expected that the precipitation clusters extracted from the mean PR rainfall state are reasonably representative of those that occur for any given lifecycle stage and day lag. MERRA depicts elevated rainfall with respect to both TRMM and CMORPH (discussed in a bit more detail later), particularly for all day lags during initiation and at ± 20 days for all other stages. Qualitatively, quite a bit of agreement can be seen when comparing the MMF panel to CMORPH.

In general, the maximum rainfall occurs near the midpoint (denoted as Midpt) of the MJO event, consistent for all observational and model depictions. While a particular longitude cannot be associated with the midpoint, it often occurs eastward of the central Indian Ocean. In order to cast these results within the context of a few prior studies, consider now a vertical transect extending from -35 to +35 days anchored to the midpoint in each panel. The composites of rainfall (or any parameter) along this vertical slice are expected to be most comparable to temporal evolutions shown in studies that calculate composites with respect to minimum OLR or MJO maximum rainfall (e.g. Benedict and Randall 2007).

By definition, precipitation clusters are characterized by raining cloud populations and vertical heating profiles; as such, quantifying the evolution of precipitation clusters amounts to tracing the evolution of raining cloud populations as a function of time. The evolving relative frequencies of occurrence (RFO) for each precipitation cluster (and a non-raining scene) are shown in Fig. 5.3. For all MJO lifecycle stages, the RFO of non-raining scenes decreases to a minimum near day 0. As discussed in Chapters 2 and 4, the SHAL cluster consists of numerous raining clouds with tops below the freezing level.

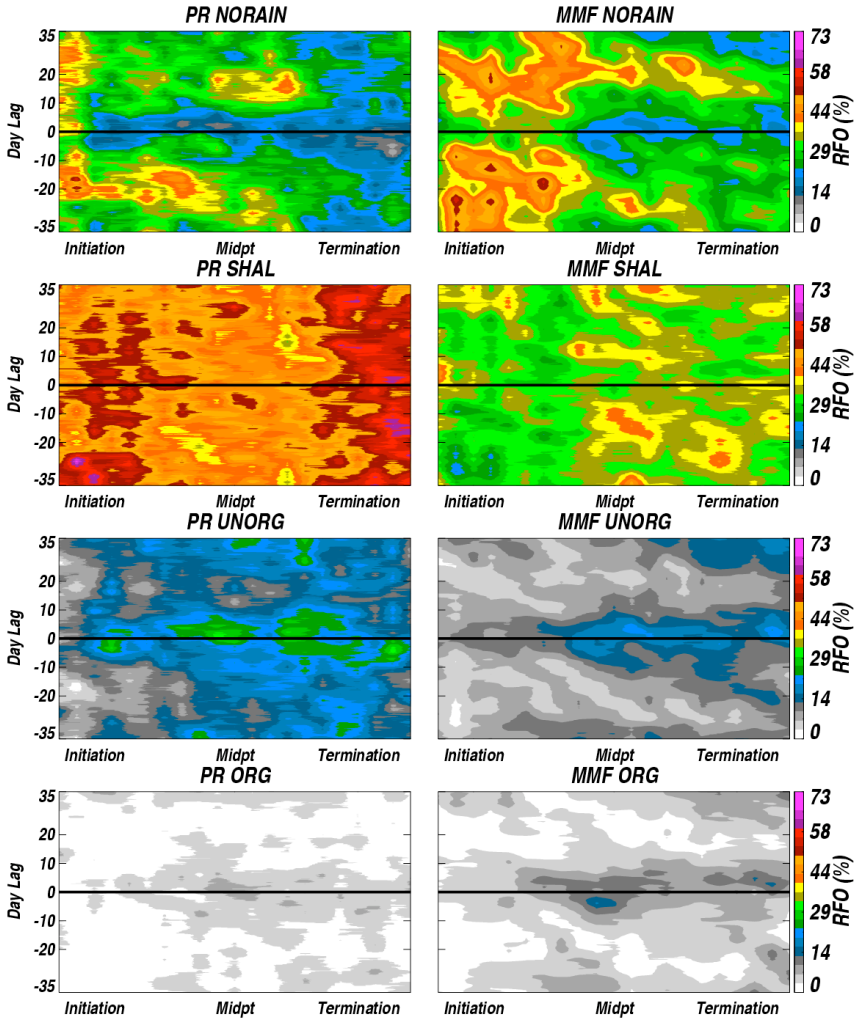

Figure 5.3. Temporal evolution of TRMM PR and MMF nonraining scenes and precipitation clusters as a function of the MJO lifecycle stage.

Interestingly, there is a near constant background of shallow raining clouds, irrespective of the temporal lag. There are variations with respect to lifecycle stage – likely reflective of mean state differences one would experience in traveling from the West Indian to Pacific Ocean basins – but, the pattern of the SHAL cluster RFOs does not reflect that of rainfall in Fig. 5.2. The UNORG clusters, mostly consisting of congestus and numerous deep clouds (likely not organized into mesoscale convective systems (MCSs), however), peaks at day 0. The ORG cluster (likely reflective of MCSs) is rare during the initiation stage until about ±5 days of day 0.

The interpretation of these results is as follows. There are always similar populations of shallow raining clouds around, independent of the day lag. This is particularly evident in the observations. Considering an alternate point of view, it would appear that there are greater numbers of shallow raining clouds present at ± 20 days only if one would compute the RFO without consideration of non-raining scenes. In considering them, however, as time progresses toward day 0, the "empty" non-raining space becomes filled with deeper clouds and eventually, organized rainfall systems. Thus, it could be said that there is not necessarily a transition from shallow raining clouds to deeper systems since SHAL clusters are prevalent at all day lags. Instead there is an addition of deeper clouds and organized systems (i.e. UNORG and ORG clusters), taking up the space formerly occupied by non-raining scenes. In effect, there is a modulation of non-raining and deeper precipitation clusters, and less variation in the SHAL cluster. This is the case for initiation and most other stages of the composite MJO event.

In comparing initiation to other stages of the MJO lifecycle, note that if one were to compute RFO anomalies for each cluster, similar evolutions would be portrayed. The

differences are really in the mean state depictions of the cluster occurrences. For instance, during the initiation stage in both the observations and MMF, it is not uncommon for several weeks to pass before the ORG cluster is observed. In other stages, it is observed more frequently as one approaches day 0, but nonetheless, it is observed at all time lags. In summary, during initiation, the SHAL cluster and non-raining scene characterize most of the variation. Over time, populations of congestus and unorganized deeper raining clouds increase, with a few organized deep convective systems occurring within ~5 days of day 0 (slightly more frequently in the MMF). Possible reasons for the lack of deeper clusters during initiation are highlighted below as variations in the background parameters are incorporated into the discussion.

5.3.2 Column-Integrated Water Vapor and Time Tendency

The evolution of TPW is shown in Fig. 5.4. MERRA and the MMF are in good

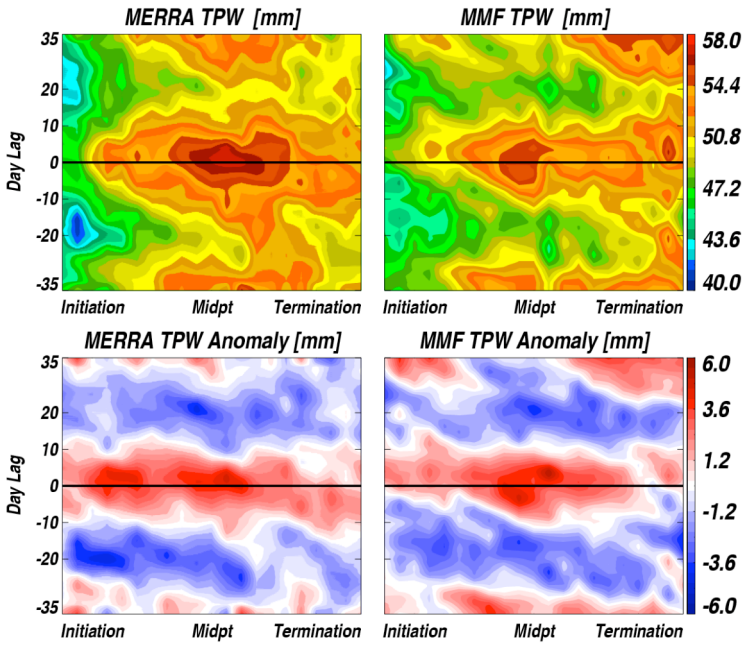

Figure 5.4. MERRA and MMF TPW temporal evolution as a function of MJO lifecycle stage.

agreement. The TPW anomaly is shown in the bottom two panels of the figure. While the mean states are different between initiation and other stages (significantly less TPW at all time lags during initiation), the anomalies in TPW are similar. This result is not unique to TPW only; anomalies in parameters are often similar during initiation and other stages of the composite MJO lifecycle. The slow increase in TPW commences at -20 days and continues until day 0. The budget equation for TPW can be written as

$$\frac{\partial}{\partial t}\mathrm{TPW} = \underbrace{-\frac{1}{g}\int_{Psfc}^{0}\overbrace{\left(\nabla_{H}\cdot qV_{H}\right)}^{\mathrm{MCONV}}dp}_{\mathrm{TPWTRANS}} + E - P + \underbrace{\left(\frac{\partial Q_{v}}{\partial t}\right)_{ANA}}_{\textit{MERRA ONLY}}. \qquad (5.1)$$

Temporal changes in TPW are driven by integrated moisture convergence (hereafter, referred to as TPWTRANS), evaporation (E) and rainfall (P). As discussed earlier, the analysis increment term in MERRA – a tendency term representing the influence of observations on the state evolution – is added to the prognostic equations and in this case, ensures that TPW follows a series of states closer to observations than may otherwise occur. The addition of this term, unique to MERRA, ensures that Eq. 5.1 is exactly satisfied for the reanalysis product.

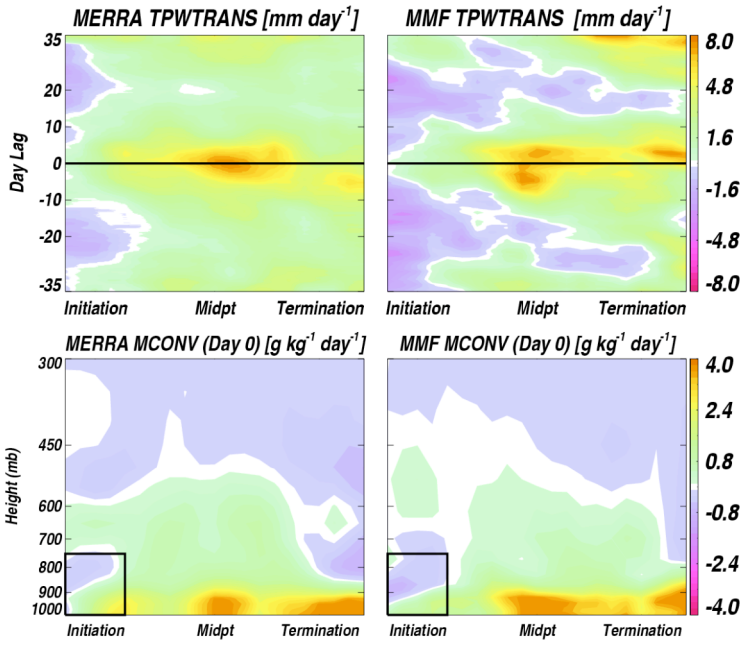

Figure 5.5. Temporal evolution of column-integrated moisture convergence in the top two panels as a function of MJO lifecycle stage. Moisture convergence as a function of altitude for each stage is illustrated in the bottom two panels.

TPWTRANS is shown in the top panels of Fig. 5.5. Of significance is the stage-dependent role that moisture convergence serves in the time tendency of TPW. During initiation, TPWTRANS is mostly negative (particularly in the MMF) or weakly positive. During later stages of the composite MJO event, TPWTRANS serves as a major contributor for increasing TPW (consistent with studies such as Maloney and Hartmann 1998). Assessing the height dependent components of TPWTRANS, horizontal moisture convergence vertical profiles (MCONV) are shown in the bottom panels. This portrayal represents the lifecycle stage and height variation along the horizontal slice (black line anchored to day 0) overlain in the top two panels of Fig. 5.5. When TPWTRANS is positive during initiation, the area of positive MCONV is quite shallow, as highlighted by the black boxes centered on initiation in the bottom panels. Recall the increased population

of congestus (and a few deep) clouds shown in Fig. 5.3 at day 0 during the initiation stage. Given this shallow MCONV, it is reasonable to think that congestus and shallower clouds are responsible for the moisture convergence, a process unique to initiation. Deep MCONV (extending up to 600 mb) is shown for all other stages at day 0. Interestingly though, it is particularly strong in the lowest levels of the atmosphere (below 850-900 mb), perhaps indicative of the continued role often-present shallow raining clouds play in moistening the environment from a convergence perspective.

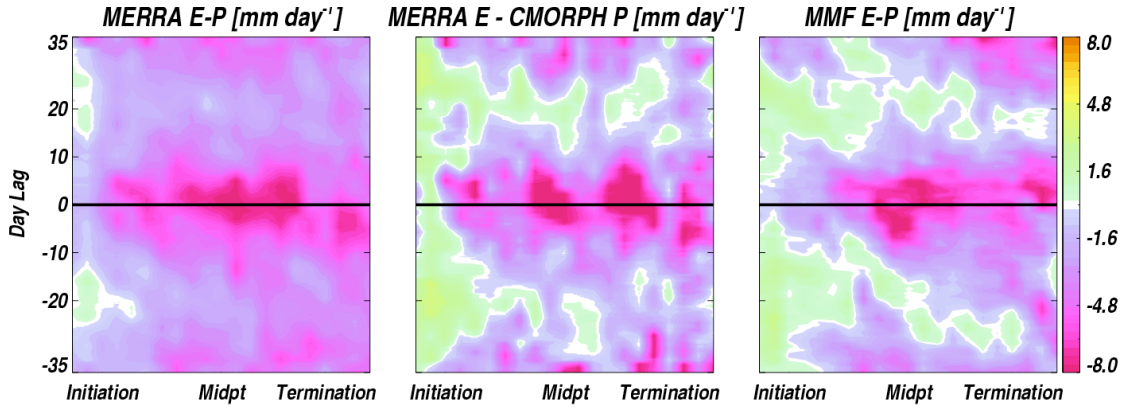

Figure 5.6. Temporal evolution of evaporation minus rainfall (E – P) for each MJO lifecycle stage. MERRA-only terms are depicted in the far left panel, while CMORPH rainfall is used in substitution of MERRA rainfall in the center panel.

E – P is illustrated in Fig. 5.6. The results for MERRA are markedly different from that which is portrayed in the MMF. Prior to the development of the most intense rainfall observed during the initiation period (day 0), the MMF shows positive E – P for virtually all day lags (-35 to -5 days, for example) while in MERRA, net evaporation is only depicted from approximately -25 to -15 days. In a global sense, both MERRA rainfall and ocean evaporation have been shown to more closely resemble available observational data sets than a number of other reanalysis products, although positive biases in tropical rainfall

continue to be documented (Bosilovich et al. 2011). That MERRA yields enhanced rainfall relative to CMORPH (Fig. 5.2) and thus, decreased E – P, is not particularly surprising considering the prior study cited.

Retaining MERRA evaporation but using CMORPH in substitution of MERRA rainfall instead, the new E – P calculations are shown in the middle panel of Fig. 5.6. While not implying that MMF E – P is the final benchmark to strive for, the portrayals are now much more consistent. During initiation, evaporation is most important for virtually all day lags, and contributes largely to the positive time tendency in TPW. The difference in rainfall (MERRA – CMORPH) is, for most stages and lags, positive as shown in Fig. 5.7. The MERRA analysis increment term for TPW (Eq. 5.1) is shown in the middle panel of Fig. 5.7. Moreover, in addition to the extensive positive differences in rainfall, the tendency in water vapor due to the analysis increment is positive. In other words, an additional moistening (independent of physics) is almost always necessary in the MMF, in part

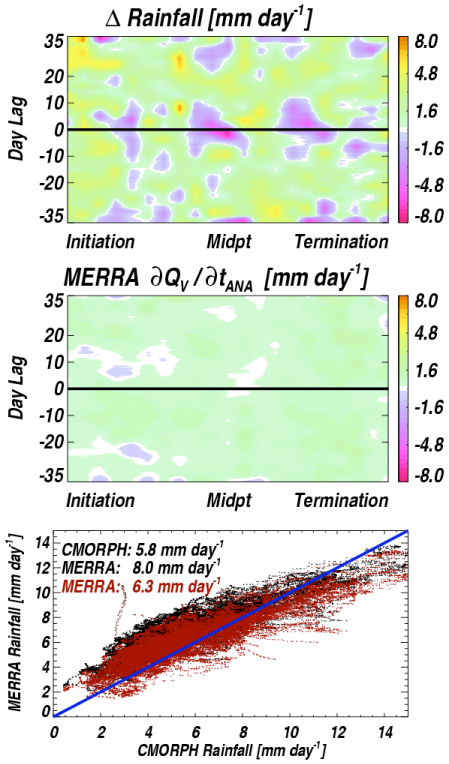

Figure 5.7. MERRA minus CMORPH rainfall is illustrated in the top panel. The MERRA column-integrated analysis increment term for water vapor is shown in the middle panel. A scatterplot of MERRA rainfall versus CMORPH rainfall is shown in the bottom panel (black), while the red dots denote the comparison for MERRA rainfall "corrected" with the analysis increment term.

because there is too much depletion due to rainfall (as evidenced in the top panel of Fig. 5.7). In an approximate sense then,

$$P_{CMORPH} \approx P - \left(\frac{\partial Q_v}{\partial t} \right)_{ANA}, \quad (5.2)$$

where P is MERRA rainfall as in Eq. 5.1. In effect, modifying MERRA rainfall by subtracting the analysis increment term brings the new estimate of MERRA rainfall closer to that of CMORPH, as shown in the bottom-most scatter plot panel of Fig. 5.7. There is reason to suspect then that the E – P composite (using MERRA for E, and CMORPH for P in the center panel of Fig. 5.6) may be more realistic than the E – P composite obtained through use of MERRA terms only.

Synthesizing all components of the integrated water budget, there is a fairly consistent picture between observations-based reanalysis and MMF output regarding the processes that increase TPW from days -20 to 0 during initiation and other lifecycle stages of the MJO. During initiation, the process of evaporation moistens the environment (Fig. 5.6) in the presence of raining congestus (and shallower) clouds. There is a contribution by moisture convergence near a day lag of 0, but it appears to be shallow (Fig. 5.5) and therefore, it is reasonable to assume that these same shallower (SHAL, UNORG) clusters are largely responsible for this increase. Once the MJO event has developed, there is a role-reversal in moistening processes. Comparable increases in TPW now occur largely due to deep moisture convergence (Fig. 5.5), while depletion of TPW by precipitation now overwhelms the increase by evaporation (i.e. more expansive areas of negative E – P in Fig. 5.6).

The view presented highlights the MJO lifecycle-dependent role in moistening processes. The extended period (over 20 days) of SHAL clusters unaccompanied by

organized deep convection allows for a slow, consistent buildup of TPW during initiation. If additional organized systems were present, then further increases in TPW might be limited due to the increase in area-average rainfall.

5.3.3 Lower-Troposphere Temperature Lapse Rates

The lack of deep convection during most day lags of the initiation stage is an interesting problem. In Chapters 3 and 4, it was posited that deep rainfall (associated with the UNORG and ORG clusters) was very dependent on moisture as well as convective inhibition (CIN) in relation to cold pool activity. Conceptually, cold pools may assist in the development of deeper rainfall by a dynamic mechanism that involves lifting of surface air beyond a slightly more stable lower-troposphere (characterized by increased temperature lapse rates). Increased lapse rates would be proportional to the magnitude of CIN in those chapters.

The lower-troposphere lapse rates (750 – 900 mb) are shown for MERRA and the MMF in Fig. 5.8. Relative to all stages in the lifecycle of the MJO, the permanent presence of increased lapse rates is a noteworthy signature of the initiation period. Decreased magnitudes of TPW (Fig. 5.4) in association with increased lapse rates (i.e. increased CIN) may both be responsible for the continued presence of the SHAL clusters as shown in Fig. 5.3, and may prevent the widespread development of UNORG and ORG clusters in the observations and MMF during the initiation period. In return, this allows for a continued increase in TPW over a long time scale. If the stable layer was weaker during the initiation stage, then perhaps UNORG and ORG clusters would develop more quickly and rainfall would be enhanced sooner than otherwise would occur, thus shortening the time-scale of

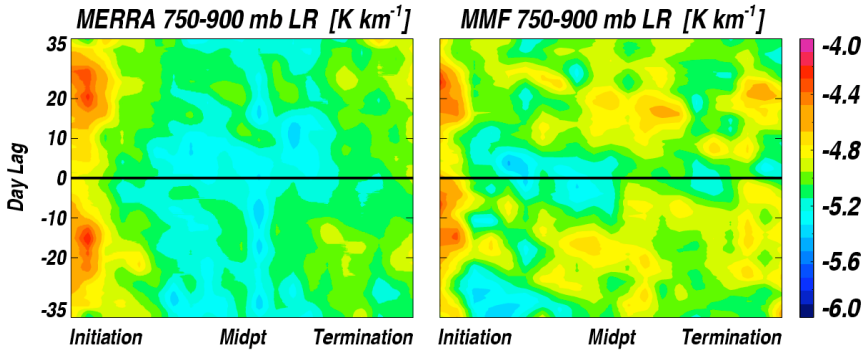

Figure 5.8. Temporal evolution of lower-troposphere temperature lapse rates as a function of MJO lifecycle stage.

moistening as E – P would go negative. The vertical extent of the moisture convergence couplet (positive moisture convergence below 900 mb; negative up to 750 mb) highlighted by the black boxes in Fig. 5.5 is consistent with the location of the stronger stable layer, such that much of the moisture transport occurs beneath the layer in association with shallow and congestus raining clouds.

5.4 Conclusions

Temporal evolutions of rainfall, raining cloud populations, TPW, moisture convergence, E – P and lower-troposphere temperature lapse rates are derived for each stage of a composite MJO event. The composite event typically initiates in the West Indian Ocean and terminates near the dateline. For each stage of the MJO (defined according to the centered position of the convective envelope traveling from the Indian to Pacific Ocean basin), the derived temporal composites are illustrated and compared with the purpose of determining to what extent the atmosphere evolves in a similar manner independent of the MJO event stage.

To a large extent, the composite event is indicative of a situation in which non-raining scenes, congestus (> 5 km) clouds and collections of both unorganized deep and organized deep convective cloud ensembles are modulated in frequency for all stages of the composite event. In contrast, populations of shallow raining clouds (2 – 4 km in depth) are often prevalent, independent of the lifecycle stage and time lag considered. Therefore, instead of considering a conceptual view that entails a transition from shallow rain to deeper systems as the convectively active phase of the MJO approaches, the results suggest that the numbers of deep clouds and organized systems increase at the expense of non-raining scenes. Instead of a transition from shallow to deep, results suggest an addition of deep clouds. This finding is consistent for all stages of the MJO. Because there is not necessarily a transition from shallow raining systems to deeper ones, the low-level cooling and drying that is often associated with deeper systems – thus stabilizing the environment – could be offset by a constant presence of shallow raining clouds serving to moisten and heat the lowest levels of the atmosphere. In this way, deep convection may not shut off as quickly. In a conceptual view that involves a transition from shallow to deep, this would not be feasible.

With respect to the initiation stage of the MJO event relative to others, the shallow raining cloud populations remain constant and as time proceeds, progressively-deeper congestus are observed along with an addition of a few organized deep systems. However, most of the initiation stage passes without the occurrence of the deepest precipitation cluster. A similar view is presented in the MMF, although there is some indication that the deepest organized precipitation cluster occurs a bit more frequently. With respect to the other stages of the composite event, similar transitions in raining cloud populations occur;

however, organized systems are much more prevalent at all times, even during the "suppressed" phase of the MJO.

For all stages of lifecycle, while the absolute mean-state magnitudes of TPW are different, similar increases in TPW occur as time tends toward the period of stage-dependent maximum rainfall (Day Lag 0). However, during initiation, the multi-week increase in TPW is mostly the result of evaporation exceeding precipitation. Eventually, as Day 0 is approached, positive moisture convergence is observed; however, it takes place over a shallow layer depth (observed mostly below 850 – 900 mb). Evaporation and moisture convergence switch roles during the more developed stages of the MJO event. As the MJO event propagates eastward, evaporation exceeds precipitation only at lags of -15 to -25 days. During this same period, moisture convergence deepens and grows increasingly positive and serves to continue increasing TPW up to Day 0.

The lack of deep systems during initiation, from the TRMM perspective particularly, is striking. In addition to decreased TPW, a particularly strong stable layer is observed from 750 – 900 mb, perhaps limiting the extent to which heavy rainfall can develop. Both factors could plausibly limit the development of deep precipitation clusters. The delay in the development of deep clusters and associated heavy rainfall during initiation is important as it allows for the unfettered growth in TPW, largely through the slow process of evaporation and later, shallow moisture convergence. In addition to this satellite and MMF perspective, in situ data collected during the CINDY2011/DYNAMO campaign is expected to significantly contribute to the quantification of the raining cloud populations most prevalent during the initiation period, and will further assist in the

development of a conceptual description of the intraseasonal timescale moistening processing operating during this period in the West Indian Ocean.

CHAPTER 6

CONCLUSIONS

The research topics of Chapters 2 – 5 can be broadly grouped into three themes, all of which involve incorporating data from multi-sensor observations and output from an MMF simulation. These themes concern: 1) an investigation of the regionally-varying mean-state of rainfall in the tropics by extracting and characterizing "building blocks" (i.e. collections of raining clouds) of the mean state independently for adjacent ocean basins in the tropics; 2) an investigation of the transition from light to heavier rainfall on hourly timescales considering all ocean basins as a whole; and 3) an investigation of the evolution of rainfall regimes and associated raining cloud populations during the initiation stage of the MJO in the West Indian Ocean. All three themes relate to the goal of understanding what types of precipitation systems contribute to regional rainfall characteristics, and what parameters (able to be both derived utilizing currently-existing observational platforms and simulated through use of an MMF configuration) serve to influence the transition from light rainfall systems to deeper ones over varying timescales.

Specifically, in Chapter 2, radar data from TRMM PR are used in a clustering algorithm that classifies precipitation regimes based on the ensemble of precipitating clouds present at a given time over a specified grid-size similar to that of a GCM grid cell.

Three similar precipitation clusters emerge consistently within each ocean basin, the characteristics of which are largely independent of the basin under investigation. The three precipitation clusters consist of shallower raining clouds (ensemble of clouds whose tops peak below the freezing level), unorganized deep convection (deep clouds exist in the distributions, but less extensive upper level heating may indicate a lack of organization associated with the regime) and organized convection (numerous deep and shallow clouds, and extensive heating above the freezing level). The distributions of raining cloud top heights at a 1 – 2° spatial scale are bimodal in the deepest clusters, signifying a population of shallow and congestus clouds in close proximity to deeper convective clouds. This is consistent for all basins; therefore, it can be used as a benchmark for convective parameterizations that strive to first represent appropriate ensembles of convective clouds and then to accurately represent their interaction with the environment.

Future work should include an investigation into the mechanisms responsible for bi-modality in the raining cloud populations at the 1 – 2° spatial scale, as well as quantification of transport and source terms affecting global water and energy budgets that are likely influenced by the presence of a particular precipitation cluster.

Each cluster discussed in Chapter 2 is associated with substantially different surface rainfall rates. This motivates an investigation of what (observable) mechanisms delineate weaker rainfall states from heavier ones, and over what timescales lightly raining cloud populations transition to heavier ones. This is the subject of Chapter 3. The incorporation of the CMORPH rainfall product allows for rainfall evolution to be studied on hourly timescales. Key radiosonde-based parameters such as saturation fraction, CAPE and CIN are discussed. Generally, CAPE and periods of decreased CIN are observed without the

development of heavier rainfall. For more intense rainfall cycles, significant reductions (~40%) in CAPE occur, suggesting that on average, periods of heavy rainfall (constituting 30 – 40% of the total precipitation in the tropics) and associated CAPE consumption are not in equilibrium with large-scale CAPE forcing. These composite results imply that heavy rainfall (from a 2° spatial scale perspective) occurs frequently in the absence of strong forcing.

Recent modeling studies have begun to focus on sub-GCM scale processes as they relate to strengthening convection. With this in mind, the role that unresolved cold pool activity plays in the transition from light to heavy rainfall (averaged to 2°) is investigated. Cold pool activity, for the first time derived from a satellite perspective, is summarized in a parameter with energy units (CPKE) and averaged over the same 2° scale. It is argued that the envelope of increased rainfall is marked by the period over which CPKE approaches the magnitude of CIN. Physically, once rainfall has commenced, CPKE increases and is considered to be a significant lifting mechanism allowing for boundary layer parcels to break through lower troposphere stable layers, thereby promoting the development of additional, deeper clouds. It is hypothesized that even lightly raining clouds can generate CPKE; thus, in addition to the moisture preconditioning role shallow raining clouds serve, they may also serve as agents for generating CPKE. The time period over which CPKE is of comparable magnitude to CIN also outlines the time during which rapid depletion of CAPE occurs. CIN itself is a function of cold pool activity. Therefore, as rainfall progresses, cold pool activity may have the effect of increasing CIN to such an extent that it eventually overwhelms CPKE, thereby leading to a substantial decrease in area-averaged rainfall.

The extent to which CPKE is influenced by phenomena other than cold pools (e.g. strong, organized updrafts influencing surface winds), the relationship between CPKE and cloud-base mass flux (for the purposes of convective parameterization) and the degree to which shallow raining clouds can influence CPKE are subjects of future modeling and observational work.

In Chapter 4, TRMM precipitation clusters are compared to collections of raining clouds derived from an MMF simulation. The simulation used in this study is unique in that the atmospheric model is coupled to a simple mixed-layer ocean model, thus allowing for a more realistic interaction between SSTs and lower-atmosphere energy fluxes. It is found that observed precipitation clusters are largely reproduced in the MMF after accounting for vertical resolution effects on cloud distribution derivations, and limitations in the PR product pertaining to capturing the correct distribution of shallow, lightly raining clouds. In both the observations and especially the MMF, precipitation clusters are reasonably well separated in a state space defined by saturation fraction and CPKE. A deeper rainfall cluster can occur at a lower saturation fraction given sufficient cold pool activity. Physically, it is suggested that this occurs because larger areas of rising motion constituting ensembles of clouds occur in association with increased cold pool activity. This may be equated to an increase in size of convective plumes; thus, clouds may be more resistant to the detrimental effects of dry air entrainment. Even in the coarse-resolution CRM used here, similar behavior seems to be occurring.

The same conceptual framework for understanding the increase in area-averaged tropical rainfall, developed in Chapter 3, is applied to the MMF. Significant increases in rainfall are accompanied by substantial decreases in CAPE, consistent with the

observations. The MMF simulates this characteristic of non-equilibrium convection behavior quite well, likely in contrast to GCMs utilizing traditional convective parameterizations that assume quasi-equilibrium behavior between consumption of CAPE by convection and increases due to all non-convective processes. In observations, CIN peaked after the period of maximum rainfall and was out of phase with CPKE (which peaks during rainfall). The lag allows for CIN to overwhelm CPKE in a more dramatic manner, serving to cap the time period during which rainfall remains elevated. In the MMF, rainfall, CPKE and CIN are all tightly coupled and in phase, hypothesized to be the result of the two-dimensionality and limited domain of the currently embedded CRM. The enhanced coupling of CPKE and CIN, even in light rainfall, means that heavier rainfall may be quicker to develop and slower to end than would be the case in a larger-domain CRM or three-dimensional CRM configuration. It was proposed that this contributes to a lengthening of the time scale during which rainfall remains elevated in the MMF relative to that which is depicted in the observational study.

Comparing the evolution of rainfall on hourly timescales from observations and the MMF to a coarser-resolution, parameterized model is a subject of future research. Additionally, the CPKE and CIN relation to 1 – 2° rainfall time tendency will be explored in higher-resolution model studies to further assess the mechanism's ability to explain rainfall in a model that sufficiently reproduces the full spectrum of shallow and deep raining clouds.

In Chapter 5, temporal evolutions of rainfall, raining cloud populations, TPW, moisture convergence, E – P and lower-troposphere temperature lapse rates are derived for each stage of a composite MJO event. Non-raining scenes, populations of congestus (> 5

km) clouds and collections of both unorganized deep and organized deep convective cloud ensembles are modulated in frequency for all stages of the composite event; in contrast, populations of shallow raining clouds (2 – 4 km in depth) are often prevalent, independent of the lifecycle stage and time lag considered. Therefore, instead of considering a conceptual view that entails a transition from shallow rain to deeper systems as the convectively active phase of the MJO approaches, the results indicate that the numbers of deep clouds and organized systems increase at the expense of non-raining scenes. Instead of a transition from shallow to deep, there is an addition of deep clouds. This finding is consistent for all stages of the MJO. Because there is not necessarily a transition from shallow raining systems to deeper ones, the low-level cooling and drying that often is associated with deeper systems – thus stabilizing the environment – could be offset by a constant presence of shallow raining clouds serving to moisten and heat the lowest levels of the atmosphere. In this way, deep convection may not shut off as quickly. In a conceptual view that involves a transition from shallow to deep, this would not be feasible.

Moistening processes are discussed for the MJO initiation stage. The ~20 day increase in TPW is mostly the result of evaporation exceeding precipitation. Eventually, as Day 0 is approached, positive moisture convergence is observed; however, it takes place over a shallow layer depth (observed mostly below 850 – 900 mb). Evaporation and moisture convergence switch roles during the more developed stages of the MJO event. As the MJO event propagates eastward, evaporation exceeds precipitation only at lags of -15 to -25 days. During this same period, moisture convergence deepens and grows increasingly positive. During these later stages, moisture convergence serves as the dominant mechanism for increasing TPW up to Day 0.

The initiation period is characterized by a lack of deep systems. Along with decreased TPW, a particularly strong stable layer (i.e. CIN) is observed from 750 – 900 mb. In Chapters 3 and 4, the development of deeper rainfall was related to CIN and CPKE. For all time lags during the initiation stage, the joint effects of decreased TPW and increased CIN likely place a strong restraint on the development of deep precipitation clusters. The delay in the development of deep clusters and associated heavy rainfall during initiation could allow for the continued growth in TPW, largely through the slow process of evaporation and later, shallow moisture convergence. In contrast, if heavy rainfall were to develop more quickly, E – P would likely decrease, and the timescale for moistening may be shortened.

A continued investigation of shallow raining clouds, their properties and their hypothesized nearly-constant occurrence frequency, independent of MJO lifecycle stage, will be performed using multi-year compilations of CloudSat data in conjunction with TRMM PR depictions. The role that CPKE may play in the initial development of the deeper precipitation clusters in the drier and more stable atmosphere characteristic of the West Indian MJO initiation period, along with a more in-depth investigation of the transport and evaporation terms of the moisture budget equation (using other datasets) are expected aspects of future work as well.

REFERENCES

Allen, M. R., and W. J. Ingram, 2002: Constraints on the future changes in climate and the hydrological cycle. *Nature*, **419**, 224 - 232.

Anderberg, M. R., 1973: *Cluster analysis for applications*. Academic Press, New York, 359 pp.

Arakawa, A., 2004: The Cumulus Parameterization Problem: Past, Present, and Future. *J. Climate*, **17**, 2493 - 2525.

_____, J.-H. Jung, and C.-M. Wu, 2011: Toward unification of the multiscale modeling of the atmosphere. *Atmos. Chem. Phys. Discuss.*, **11**, 3181 - 3217.

Benedict, J. J., and D. A. Randall, 2007: Observed Characteristics of the MJO Relative to Maximum Rainfall. *J. Atmos. Sci.,* **64**, 2332-2354.

_____, and _____, 2009: Structure of the Madden-Julian Oscillation in the Superparameterized CAM. *J. Atmos. Sci.*, **66**, 3277 - 3296.

_____, and _____, 2011: Impacts of Idealized Air-Sea Coupling on Madden-Julian Oscillation Structure in the Superparameterized CAM. *J. Atmos. Sci.*, doi:10.1175/JAS-D-11-04.1. **in press.**

Berg, W., C. D. Kummerow, and C. Morales, 2002: Differences between East and West Pacific Rainfall Systems. *J. Climate*, **15**, 3659 - 3672.

_____, T. L'Ecuyer, J. M. Haynes, 2010: The Distribution of Rainfall over Oceans from Spaceborne Radars. *J. Appl. Meteor. Climatol.*, **49**, 535 - 543.

Blade, I., and D. L. Hartmann, 1993: Tropical intraseasonal oscillation in a simple nonlinear model. *J. Atmos. Sci.,* **50**, 2922-2939.

Boccippio, D. J., W. A. Petersen, and D. J. Cecil, 2004: The tropical convective spectrum. Part I: Archetypal vertical structures. *J. Climate*, **18**, 2744 - 2769.

Bosilovich, M. G., F. R. Robertson, J. Chen, 2011: Global Energy and Water Budgets in MERRA. *J. Climate*, doi:10.1175/2011JCLI4175.1. **in press.**

Bretherton, C. S., J. R. McCaa, and H. Grenier, 2004: A New Parameterization for Shallow Cumulus Convection and Its Application to Marine Subtropical Cloud-Topped Boundary Layers. Part I: Description and 1D Results. *Mon. Wea. Rev.*, **132**, 864 - 882.

_____, M. E. Peters, and L. E. Back, 2004: Relationships between Water Vapor Path and Precipitation. *J. Climate*, **17**, 1517 - 1528.

Brown, R. G., and C. Zhang, 1997: Variability of Midtropospheric Moisture and Its Effect on Cloud-Top Height Distribution during TOGA COARE. *J. Atmos. Sci.*, **54**, 2760 - 2774.

Caine, S., C. Jakob, S. Siems, and P. May, 2009: Objective classification of precipitating convective regimes using a weather radar in Darwin, Australia. *Mon. Wea. Rev.*, **137**, 1585 - 1600.

Chaboureau, J.-P., F. Guichard, J.-L. Redelsperger, and J.-P. Lafore, 2004: The role of stability and moisture in the diurnal cycle of convection over land. *Quart. Jour. Roy. Meteor. Soc.*, **130**, 3105 - 3117.

Chelton, D. B., and M. H. Freilich, 2005: Scatterometer-Based Assessment of 10-m Wind Analyses from the Operational ECMWF and NCEP Numerical Weather Prediction Models. *Mon. Wea. Rev*., **133**, 409 - 429.

Collins, W. D., and Coauthors, 2006: The Formulation and Atmospheric Simulation of the Community Atmosphere Model Version 3 (CAM3). *J. Climate*, **19**, 2144 - 2161.

DeMott, C. A., C. Stan, D. A. Randall, J. L. Kinter III, and M. Khairoutdinov, 2011: The Asian Monsoon in the Super-Parameterized CCSM and its Relationship to Tropical Wave Activity. *J. Climate*, doi:10.1175/2011JCLI4202.1, **submitted.** 3055 - 3079.

Derbyshire, S. H., I. Beau, P. Bechtold, J.-Y. Grandpeix, J.-M. Piriou, J.-L. Redelsperger, and P.M.M. Soares, 2004: Sensitivity of moist convection to environmental humidity. *Quart. Jour. Roy. Meteor. Soc.*, **130**, 3055 - 3079.

Durre, I., R. S. Vose, and D. B. Wuertz, 2006: Overview of the Integrated Global Radiosonde Archive. *J. Climate*, **19**, 53 - 67.

Elsaesser, G. S., C. D. Kummerow, T. S. L'Ecuyer, Y. N. Takayabu, and S. Shige, 2010: Observed Self-Similarity of Precipitation Regimes Over the Tropical Oceans. *J. Climate*, **23**, 2686 - 2698.

Emanuel, K. A., 1994: *Atmospheric Convection.* Oxford University Press, 580 pp.

Fletcher, J. K., and C. Bretherton, 2010: Evaluating Boundary Layer-Based Mass Flux Closures Using Cloud-Resolving Model Simulations of Deep Convection. *J. Atmos. Sci.*, **67**, 2212 - 2225.

Freilich, M. H., D. G. Long, and M. W. Spencer, 1994: SeaWinds: A scanning scatterometer for ADEOS II-Science overview. *Proc. Int. Geoscience and Remote Sensing Symp.*, Pasadena, CA, IEEE, 960 - 963.

Grabowski, W. W., 2001: Coupling Cloud Processes with the Large-Scale Dynamics Using the Cloud-Resolving Convection Parameterization (CRCP). *J. Atmos. Sci.,* **58**, 978 - 997.

_____, and P. K. Smolarkiewicz, 1999: A cloud resolving convective parameterization for modeling the tropical convective atmosphere. *Physica D.,* **133**, 171 - 178.

Haertel, P. T., and G. N. Kiladis, 2004: Dynamics of 2-Day Equatorial Waves. *J. Atmos. Sci.*, **61**, 2707 - 2721.

Hohenegger, C., and C. S. Bretherton, 2011: Simulating deep convection with a shallow convection scheme. *Atmos. Chem. Phys. Discuss.*, **11**, 8385 - 8430.

Hou, A., G. S. Jackson, C. Kummerow, and C. M. Shepherd, 2008: Global precipitation Measurement, in *Precipitation: Advances in Measurement, Estimation, and Prediction*, edited by S. Michaelides, pp. 1 - 39.

Houze, R. A., Jr., 1997: Stratiform precipitation in regions of convection: A meteorological paradox? *Bull. Amer. Meteor. Soc.*, **78**, 2179 - 2196.

_____, and A. K. Betts, 1981: Convection in GATE. *Rev. Geophys. Space Phys.*, **19**, 541 - 576.

Huddleston, J. N., and B. W. Stiles, 2000: Multidimensional histogram (MUDH) rain flag product description (version 3.0). Jet Propulsion Laboratory, Pasadena, CA, 8 pp. [*Available online at ftp://podaac.jpl.nasa.gov/pub/ocean_wind/quikscat/L2B/doc/MUDH_Description_V3.pdf]*

Iguchi, T., T. Kozu, R. Meneghini, J. Awaka, and K. Okamoto, 2000: Rain-profiling algorithm for the TRMM precipitation radar. *J. Appl. Meteor.*, **39**, 2038 - 2052.

Jakob, C., and G. Tselioudis, 2003: Objective identification of cloud regimes in the Tropical Western Pacific. *Geophys. Res. Lett.*, **30**, doi:10.1029/2003GL018367.

_____, _____, and T. Hume, 2005: The radiative, cloud, and thermodynamic properties of the major tropical western Pacific cloud regimes. *J. Climate*, **18**, 1203 - 1215.

Johnson, R. H., T. M. Rickenbach, S. A. Rutledge, P. E. Ciesielski, and W. H. Schubert, 1999: Trimodal characteristics of tropical convection. *J. Climate*, **12**, 2397 - 2418.

Jones, C., and B. C. Weare, 1996: The Role of Low-Level Moisture Convergence and Ocean Latent Heat Fluxes in the Madden and Julian Oscillation: An Observational Analysis Using ISCCP Data and ECMWF Analyses. *J. Climate*, **9**, 3086 - 3104.

Joyce, R.J., J. E. Janowiak, P. A. Arkin, and P. Xie, 2004: CMORPH: A method that produces global precipitation estimates from passive microwave and infrared data at high spatial and temporal resolution. *J. Hydromet.*, **5**, 487 - 503.

Khairoutdinov, M., C. DeMott, and D. Randall, 2008: Evaluation of the Simulated Interannual and Subseasonal Variability in an AMIP-Style Simulation Using the CSU Multiscale Modeling Framework. *J. Climate*, **21**, 413 - 431.

_____, S. K. Krueger, C.-H. Moeng, P. A. Bogenschutz, and D. A. Randall, 2009: Large-Eddy Simulation of Maritime Deep Tropical Convection. *J. Adv. Model. Earth Syst.*, **Vol. 1**, 13 pp.

_____, and D. A. Randall, 2003: Cloud Resolving Modeling of the ARM Summer 1997 IOP: Model Formulation, Results, Uncertainties, and Sensitivities. *J. Atmos. Sci.*, **60**, 607 - 625.

_____, and _____, 2006: High-Resolution Simulation of Shallow-to-Deep Convection Transition over Land. *J. Atmos. Sci.*, **63**, 3421 - 3436.

Kim, D., and Coauthors, 2009: Application of MJO Simulation Diagnostics to Climate Models. *J. Climate*, **22**, 6413 - 6436.

Kim, H.-M., C. D. Hoyos, P. J. Webster, and I.-S. Kang, 2009: Ocean-atmosphere coupling and the boreal winter MJO. *Clim. Dyn.*, doi:10.1007/s00382-009-0612-x.

Kingsmill, D. E., 1995: Convection Initiation Associated with a Sea-Breeze Front, a Gust Front, and Their Collision. *Mon. Wea. Rev.*, **123**, 2913 - 2933.

Kuang, Z., and C. S. Bretherton, 2006: CMORPH: A Mass-Flux Scheme View of a High-Resolution Simulation of a Transition from Shallow to Deep Cumulus Convection. *J. Atmos. Sci.*, **63**, 1895 - 1909.

Kummerow, C. D., W. Barnes, T. Kozu, J. Shiue, and J. Simpson, 1998: The Tropical Rainfall Measuring Mission (TRMM) Sensor Package. *J. Atmos. Oceanic Technol.*, **15**, 809 - 817.

Lau, K. M., L. Peng, C. H. Sui and T. Nakazawa, 1989: Dynamics of superclusters, westerly wind bursts, 30-60 day oscillations, and ENSO: A unified view. *J. Meteor. Soc. Japan,* **67**, 205-219.

Lawrence, D. M., and P. J. Webster, 2001: Interannual Variations of the Intraseasonal Oscillation in the South Asian Summer Monsoon Region. *J. Climate,* **14**, 2910-2922.

L'Ecuyer, T. S., and G. L. Stephens, 2003: The tropical oceanic energy budget from the TRMM perspective. Part I: Algorithm and uncertainties. *J. Climate*, **16**, 1967 - 1985.

_____, and _____, 2007: The tropical oceanic energy budget from the TRMM perspective. Part II: Evaluating GCM representations of the sensitivity of regional energy and water cycles to the 1998-99 ENSO cycle. *J. Climate*, **20**, 4548 - 4571.

_____, and G. McGarragh, 2009: A 10-year climatology of tropical radiative heating and its vertical structure from TRMM observations. *J. Climate*, **23**, 519 - 541.

Lima, M. A., and J. W. Wilson, 2008: Convective Storm Initiation in a Moist Tropical Environment. *Mon. Wea. Rev.*, **136**, 1847 - 1864.

Lin, B., B. A. Weilicki, P. Minnis, L. Chambers, K.-M. Xu, Y. Hu, and A. Fan: The Effect of Environmental Conditions on Tropical Deep Convective Systems Observed from the TRMM Satellite. *J. Climate*, **19**, 5745 - 5761.

Lin, J.-L., and Coauthors, 2006: Tropical Intraseasonal Variability in 14 IPCC AR4 Climate Models. Part I: Convective Signals. *J. Climate,* **19**, 2665-2690

Liu, C., and E. J. Zipser, 2009: "Warm Rain" in the Tropics: Seasonal and Regional Distributions Based on 9 yr of TRMM Data. *J. Climate*, **22**, 767 - 779.

_____, _____, D. J. Cecil, S. W. Nesbitt, and S. Sherwood, 2008: A Cloud and Precipitation Feature Database from Nine Years of TRMM Observations. *J. Appl. Meteor. Clim.*, **47**, 2712 - 2728.

Liu, W. T., 2002: Progress in Scatterometer Applications. *J. Oceanogr.*, **58**, 121 - 136.

Luo, Zhengzhao, G. Y. Liu, G. L. Stephens, and R. H. Johnson, 2009: Terminal versus transient cumulus congestus: A CloudSat perspective. *Geophys. Res. Lett.*, **36**, doi:10.1029/2008GL036927.

Madden, R. A., and P. R. Julian, 1971: Detection of a 40-50 day oscillation in the zonal wind in the tropical Pacific. *J. Atmos. Sci.,* **28**, 702-708.

_____, and _____, 1972: Description of global-scale circulation cells in the Tropics with a 40-50 day period. *J. Atmos. Sci.,* **29**, 1109-1123.

Majda, A. J., and S. N. Stechmann, 2009: The skeleton of tropical intraseasonal oscillations. *Proc. Natl. Acad. Sci.,* **106 (21)**, 8417.

_____, and _____, 2011: Nonlinear Dynamics and Regional Variations in the MJO Skeleton. *J. Atmos. Sci.,* **accepted**.

Maloney, E. D., and D. L. Hartmann, 1998: Frictional Moisture Convergence in a Composite Life Cycle of the Madden – Julian Oscillation. *J. Climate,* **11**, 2387-2403.

_____, and _____, 2000: Modulation of Eastern North Pacific Hurricanes by the Madden-Julian Oscillation. *J. Climate,* **13**, 1451-1460.

_____, and _____, 2001: The Madden-Julian oscillation, barotropic dynamics, and North Pacific tropical cyclone formation. Part I: Observations. *J. Atmos. Sci.,* **58**, 2545-2558.

Mapes. B. E., 2000: Convective Inhibition, Subgrid-Scale Triggering Energy, and Stratiform Instability in a Toy Tropical Wave Model. *J. Atmos. Sci.*, **57**, 1515 - 1535.

_____, S. Tulich, J. Lin, and P. Zuidema, 2006: The mesoscale convection life-cycle: Building block or prototype for large-scale tropical waves? *Dynam. Atmos. Oceans*, **42**, 3 - 29.

_____, and R. Neale, 2011: Parameterizing Convective Organization to Escape the Entrainment Dilemma. *J. Adv. Model. Earth Syst.*, **Vol. 3**, 20 pp.

Marchand, R., N. Beagley, T. P. Ackerman, 2009a: Evaluation of Hydrometeor Occurrence Profiles in the Multiscale Modeling Framework Climate Model Using Atmospheric Classification. *J. Climate*, **22**, 4557 - 4573.

_____, J. Haynes, G. G. Mace, T. Ackerman, and G. Stephens, 2009b: A comparison of simulated cloud radar output from the multiscale modeling framework global climate model with CloudSat cloud radar observations. *J. Geophys. Res.*, **114**, doi:10.1029/2008JD009790.

Masunaga, H., 2007: Seasonality and Regionality of the Madden-Julian Oscillation, Kelvin Wave and Equatorial Rossby Wave. *J. Atmos. Sci.*, **64**, 4400 - 4416.

_____, and C. D. Kummerow, 2006: Observations of tropical precipitating clouds ranging from shallow to deep convective systems. *Geophys. Res. Lett.*, **33**, doi:10.1029/2006GL026547.

_____, T. S. L'Ecuyer, and C. D. Kummerow, 2006: The Madden-Julian Oscillation Recorded in Early Observations from the Tropical Rainfall Measuring Mission (TRMM). *J. Atmos. Sci.*, **63**, 2777 - 2794.

Matthews, A. J., 2008: Primary and successive events in the Madden-Julian Oscillation. *Quart. Jour. Roy. Meteor. Soc.*, **134**, 439 - 453.

Moeng, C.-H., M. A. LeMone, M. F. Khairoutdinov, S. K. Krueger, P. A. Bogenschutz, and D. A. Randall, 2009: The Tropical Marine Boundary Layer Under a Deep Convection System: a Large-Eddy Simulation Study. *J. Adv. Model. Earth Syst.*, **Vol. 1**, 13 pp.

Mohr, K. I., J. S. Famiglietti, and E. J. Zipser, 1999: The Contribution to Tropical Rainfall with respect to Convective System Type, Size, and Intensity Estimated from the 85-GHz Ice-Scattering Signature. *J. Appl Meteor.*, **38**, 596 - 606

Moncrieff, M. W., and C. Liu, 2006: Representing Convective Organization in Prediction Models by a Hybrid Strategy. *J. Atmos. Sci.*, **63**, 3404 - 3420.

Pereira, L. G., and S. A. Rutledge, 2006: Diurnal Cycle of Shallow and Deep Convection for a Tropical Land and an Ocean Environment. *Mon. Wea. Rev.*, **134**, 2688 - 2701.

Pritchard, M. S., M. W. Moncrieff, R. C. J. Somerville, 2011: Orogenic propagating precipitating systems over the US in a global climate model with embedded explicit convection. *J. Atmos. Sci.*, doi:10.1175/2011JAS3699.1. **in press.**

_____, and R. C. J. Somerville, 2009a: Assessing the Diurnal Cycle of Precipitation in a Multi-Scale Climate Model. *J. Adv. Model. Earth Syst.*, **Vol. 1**, 16 pp.

_____, and _____, 2009b: Empirical orthogonal function analysis of the diurnal cycle of precipitation in a multi-scale climate model. *Geophys. Res. Lett.*, **36**, doi:10.1029/2008GL036964

Randall, D., M. Khairoutdinov, A. Arakawa, and W. Grabowski, 2003: Breaking the Cloud Parameterization Deadlock. *Bull. Amer. Meteor. Soc.*, **84**, 1547 - 1564.

Ray, P., C. Zhang, J. Dudhia, and S. S. Chen, 2009: A numerical case study on the initiation of the Madden-Julian oscillation. *J. Atmos. Sci.*, **66**, 310 - 331.

_____, _____, M. W. Moncrieff, J. Dudhia, J. Caron, L. R. Leung, and C. Bruyere, 2011: Role of the atmospheric mean state on the initiation of the Madden-Julian oscillation in a tropical channel model. *Clim. Dyn.*, doi: 10.1007/s00382-010-0859-2.

Rienecker, M. M., and Coauthors, 2008: The GEOS-5 Data Assimilation System – Documentation of versions 5.0.1 and 5.1.0, and 5.2.0. NASA Tech. Rep. Series on Global Modeling and Data Assimilation, NASA/TM-2008-104606, VOL. 27, 92 pp.

_____, and _____, 2011: MERRA: NASA's Modern-Era Retrospective Analysis for Research and Applications. *J. Climate*, **24**, 3624 - 3648.

Robinson, F. J., S. C. Sherwood, D. Gerstle, C. Liu, and D. J. Kirshbaum, 2011: Exploring the Land-Ocean Contrast in Convective Vigor Using Islands. *J. Atmos. Sci.*, **68**, 602 - 618.

Ross, A. N., A. M. Tompkins, and D. J. Parker, 2004: Simple Models of the Role of Surface Fluxes in Convective Cold Pool Evolution. *J. Atmos. Sci.*, **61**, 1582 - 1595.

Rossow, W. B., G. Tselioudis, A. Polak, and C. Jakob, 2005: Tropical climate described as a distribution of weather states indicated by distinct mesoscale cloud property mixtures. *Geophys. Res. Lett.*, **32**, doi:10.1029/2005GL024584.

Sherwood, S. C., 1999: Convective Precursors and Predictability in the Tropical Western Pacific. *Mon. Wea. Rev.*, **127**, 2977 - 2991.

Shige, S., Y. N. Takayabu, W.-K. Tao, and D. E. Johnson, 2004: Spectral retrieval of latent heating profiles from TRMM PR data. Part I: Development of a model-based algorithm. *J. Appl. Meteor.*, **43**, 1095 - 1113.

_____, _____, _____, and C.-L. Shie, 2007: Spectral retrieval of latent heating profiles from TRMM PR data. Part II: Algorithm improvement and heating estimates over tropical ocean regions. *J. Appl. Meteor. Clim.*, **46**, 1098 - 1124.

Short, D. A., and K. Nakamura, 2000: TRMM radar observations of shallow precipitation over the tropical oceans. *J. Climate*, **13**, 4107 - 4124.

Snodgrass, E. R., L. Di Girolamo, and R. M. Rauber, 2009: Precipitation Characteristics of Trade Wind Clouds during RICO Derived from Radar, Satellite, and Aircraft Measurements. *J. Appl. Meteor. Clim.*, **48**, 464 - 483.

Sobel, A. H., C. D. Burleyson, and S. E. Yuter, 2011: Rain on small tropical islands. *J. Geophys. Res.*, **116**, doi:10.1029/2010JD014695, 15 pp.

Steiner, M., R. A. Houze, and S. E. Yuter, 1995: Climatological Characterization of Three-Dimensional Storm Structure from Operational Radar and Rain Gauge Data. *J. Appl. Meteor.*, **34**, 1978 - 2007.

Stephens, G. L., P. J. Webster, R. H. Johnson, R. Engelen, and T. L'Ecuyer, 2004: Observational Evidence for the Mutual Regulation of the Tropical Hydrological Cycle and Tropical Sea Surface Temperatures. *J. Climate*, **17**, 2213 - 2224.

Sun, Y., S. Solomon, A. Dai, and R. W. Portmann, 2007: How Often Will It Rain? *J. Climate*, **20**, 4801 - 4818.

Takayabu, Yukari N, S. Shige, W.-K. Tao, and N. Hirota, 2010: Shallow and Deep Latent Heating Modes over Tropical Oceans Observed with TRMM PR Spectral Latent Heating Data. *J. Climate*, **23**, 2030 - 2046.

Tao, W.-K., J.-D. Chern, R. Atlas, D. Randall, M. Khairoutdinov, J.-L. Li, D. E. Waliser, A. Hou, X. Lin, C. Peters-Lidard, W. Lau, J. Jiang, and J. Simpson, 2009: A Multiscale Modeling System: Developments, Applications, and Critical Issues. *Bull. Amer. Meteor. Soc.*, **90**, 515 - 534.

Thayer-Calder, K., and D. A. Randall, 2009: The Role of Convective Moistening in the Madden-Julian Oscillation. *J. Atmos. Sci.*, **66**, 3297 - 3312.

Tompkins, A. M., 2001: Organization of Tropical Convection in Low Vertical Wind Shears: The Role of Cold Pools. *J. Atmos. Sci.*, **58**, 1650 - 1672.

Warren, S. G., C. J. Hahn, and J. London, 1985: Simultaneous occurrence of different cloud types. *J. Appl. Meteor. Clim.*, **24**, 658 - 667.

Webster, P. J., V. O. Magana, T. N. Palmer, J. Shukla, R. A. Tomas, M. Yanai, and T. Yasunari, 1998: Monsoons: Processes, predictability, and the prospects for prediction. *J. Geophys. Res.,* **103**, 14451-14510.

Wheeler, M., and G. N. Kiladis, 1999: Convectively Coupled Equatorial Waves: Analysis of Clouds and Temperature in the Wavenumber – Frequency Domain. *J. Atmos. Sci.,* **56**, 374-399.

Wu, C.-M., B. Stevens, and A. Arakawa, 2009: What Controls the Transition from Shallow to Deep Convection? *J. Atmos. Sci.*, **24**, 1793 - 667.

Yanai, M., S. Esbensen, and J.-H. Chu, 1973: Determination of bulk properties of tropical cloud clusters from large-scale heat and moisture budgets. *J. Atmos. Sci.*, **30**, 611 - 627.

Zelinka, M. D., and D. L. Hartmann: Response of Humidity and Clouds to Tropical Deep Convection. *J. Climate*, **22**, 2389 - 2404.

Zhang, C., 2005: Madden – Julian Oscillation. *Rev. Geophys.,* **43**, RG2003, doi:10.1029/2004RG000158.

Zhang, Y., S. Klein, G. G. Mace, and J. Boyle, 2007: Cluster analysis of tropical clouds using CloudSat data. *Geophys. Res. Lett.*, **34**, doi:10.1029/2007GL029336.

Zuidema, P. and B. Mapes, 2008: Cloud vertical structure observed from space and ship over the Bay of Bengal and the Eastern Tropical Pacific. *J. Meteor. Soc. Japan*, **86A**, 205 - 218.